

---

## CHAPTER 8

## *Planetary-scale waves and other eddies*

Copyright 2003 David A. Randall

---

### 8.1 Introduction

Earlier we introduced the concept of the zonally averaged circulation, and defined “eddies” as zonal inhomogeneities. In atmospheric science, the term “eddy” is often used synonymously with “wave,” but actually waves are special eddies. A “wave” can be defined as a process that transports energy without transporting mass.<sup>1</sup> Waves can also transport momentum. Familiar examples are sound waves, and water waves seen at the beach; the latter are examples of what meteorologists call “gravity waves.”

Waves can be produced by a variety of mechanisms (Fig. 8.1). Orographic forcing, heating that is localized at particular longitudes, and baroclinic and barotropic instability are among the mechanisms that can generate large-scale waves in the atmosphere. In the case of a wave forced by heating, the wave itself may or may not alter the heating.

Waves arise from a variety of physical mechanisms, and appear on many spatial and temporal scales. The atmosphere supports Rossby waves, Kelvin waves, inertia-gravity waves, mixed Rossby-gravity waves and sound waves. Wavelengths range from the circumference of the Earth, to the width of North America, to a few millimeters. Periods range from thousandths of a second to weeks. The distributions of energy and fluxes over these various scales are complicated and interesting.

From elementary physics, we know that a particle does not undergo any net displacement as a small-amplitude wave passes by; it moves in a more or less circular path, and returns to its starting point. This is consistent with the definition of “wave” given above. We also know, however, that it is possible for a surfer to ride on a large-amplitude water wave. We can think of the surfer as a particle of mass that is, in fact, transported by the wave. This illustrates that large-amplitude (often called “finite-amplitude”) waves can transport mass. A wave that can transport mass can also transport any intensive property that is “attached” to the mass, such as potential temperature or water vapor mixing ratio. If a wave is defined, as above, as a process that transports energy but not mass, then beyond some limit a large-amplitude wave is not a wave at all. We can use the word “eddy” to denote zonal inhomogeneities that may or may not be waves.

As discussed earlier, it is useful to distinguish between “stationary” eddies, which are anchored to features (such as mountain ranges) on the Earth’s surface and so appear in time-averaged (e.g. monthly mean) maps, and “transient” eddies that move and so are hidden in

---

<sup>1</sup>. This definition was given to me by Jule Charney. I have never seen it written down anywhere.

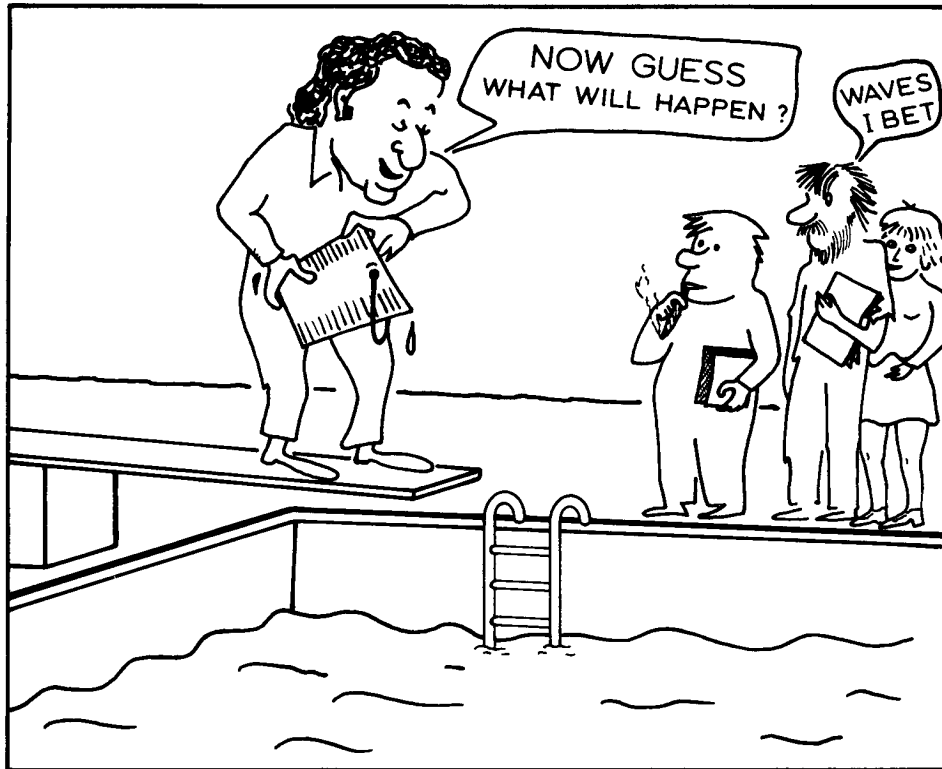


**Figure 8.1:** A cartoon that appeared in Morel (1973). The man on the diving board is Jule Charney. The other three people are presumably M.I.T. graduate students of the early 1970s.

time averages.

Eddies appear in the winds, temperatures, geopotential heights, surface pressure, water vapor mixing ratio, and all other fields that characterize the circulation. They are important aspects of the circulation in their own right, and in addition they are of interest because they can affect the zonally averaged flow by producing fluxes and flux convergences. Such feedbacks of the eddies on the zonally averaged flow are the subject of the next chapter.

As mentioned earlier, atmospheric waves come in a variety of physically distinct types. Rossby waves, which arise from conservation of potential vorticity on the sphere, are the type most properly referred to as “planetary waves,” because they depend for their existence on rotation in the presence of spherical geometry, and so are characteristic of planetary atmospheres, although of course they also occur in oceans, and in stars. Rossby waves propagate westward relative to the mean flow, so that it is possible for them to be stationary (with respect to the surface) in a westerly regime. They can be excited in many ways, including interactions of the mean flow with mountains, convective events, and instabilities of various kinds. The most energetic Rossby waves have very large horizontal scales. To the extent that they are excited at low levels, their energy propagation can be upward. Upward-propagating Rossby waves are believed to play an important role in stratospheric sudden warmings, as discussed in the next chapter.

Gravity waves arise through the action of the buoyancy force under stable stratification. They occur on many scales. When their scale is larger than the radius of deformation, they are strongly influenced by rotation, and are called “gravity-inertia waves.” They can be produced by many mechanisms, including topographic forcing and convection. Vertically propagating gravity waves are thought to produce important vertical momentum transports that strongly affect the large-scale circulation, especially in the stratosphere and above. Today, the role of gravity waves in the general circulation is a “hot” topic.

The tropical atmosphere is home to two special classes of equatorially trapped waves. These are the “mixed Rossby-gravity waves,” also called Yanai waves, which propagate westward; and Kelvin waves, which propagate eastward. As described later, these two types of waves have been implicated in the physical mechanism that drives the Quasi-Biennial Oscillation, although gravity waves are now believed to be quite important. Kelvin waves are also believed to play important roles in El Niño and in the Madden-Julian oscillation.

The purpose of the present chapter is to describe the observed climatological distribution of eddy activity, and to offer some theories of the mechanisms that produce both stationary and transient eddies.

## 8.2 Free and forced small-amplitude oscillations of a thin spherical atmosphere

### 8.2.1 Perturbation equations

Laplace (originally published in French in 1799; English translation in 1832) was the first to investigate the free and forced oscillations of a thin atmosphere on a spherical planet. His 200-year-old paper is still very relevant today. Here we briefly outline his work, omitting the mathematical details. A handout giving those details and discussing the applications of Laplace’s work to the problem of atmospheric tides is available on request.

Laplace considered a spherical planet without mountains, and with a highly idealized basic state:

$$\bar{\mathbf{V}}_h = 0, \bar{\omega} = 0, \frac{\partial \bar{\phi}}{\partial p} = -\bar{\alpha}, p\bar{\alpha} = R\bar{T}(p), p_S = p_0 = \text{constant} . \quad (8.1)$$

Here  $T(p)$  is an arbitrary function of  $p$ . Note that  $T$  does *not* depend on latitude. This basic state has no meridional temperature gradient and no mean flow. It is, of course, in balance.

The linearized governing equations are

$$\frac{\partial u'}{\partial t} = (2\Omega \sin \varphi) v' - \frac{1}{a \cos \varphi} \frac{\partial \phi'}{\partial \lambda} , \quad (8.2)$$

$$\frac{\partial v'}{\partial t} = -(2\Omega \sin \varphi) u' - \frac{1}{a} \frac{\partial \phi'}{\partial \varphi} , \quad (8.3)$$

$$\frac{1}{a \cos \varphi} \left[ \frac{\partial u'}{\partial \lambda} + \frac{\partial}{\partial \varphi} (v' \cos \varphi) \right] + \frac{\partial \omega'}{\partial p} = 0 , \quad (8.4)$$

$$\frac{\partial}{\partial p} \left( \frac{\partial \phi'}{\partial t} \right) + S_p \omega' = -\frac{R}{c_p p} \underline{Q}, \quad (8.5)$$

where

$$S_p \equiv -\frac{\bar{\alpha} \partial \bar{\theta}}{\bar{\theta} \partial p} \quad (8.6)$$

is the static stability, which depends only on  $p$ , and  $\underline{Q}$  is the heating. Friction has been neglected in the momentum equations. Also,

$$\phi' = gz' + \Phi(\lambda, \varphi, t), \quad (8.7)$$

where  $\Phi$  is the *external* gravitational tidal potential, due to the moon and/or sun. In (8.6), we recognize that the atmosphere experiences gravitational accelerations due to the pulls of the moon and sun, in addition to that of the Earth. The variation of  $\Phi$  with  $p$  is negligible, because the atmosphere is thin compared to the distances to the sun and moon. Note that these equations are valid only for atmospheres that are shallow compared to the planetary radius,  $a$ .

We look for *separable* solutions of the form

$$\begin{bmatrix} u' \\ v' \\ \omega' \\ \phi' \\ Q \\ \Phi \end{bmatrix} = \sum_n \left\{ \begin{bmatrix} U_n^{\sigma, s}(p) \\ V_n^{\sigma, s}(p) \\ W_n^{\sigma, s}(p) \\ Z_n^{\sigma, s}(p) \\ J_n^{\sigma, s}(p) \\ G_n^{\sigma, s}(p) \end{bmatrix} \Theta_n^{\sigma, s}(\varphi) \right\} \exp[i \underbrace{(s\lambda + \sigma t)}_{\text{phase}}], \quad (8.8)$$

where the  $\Theta_n^{\sigma, s}(\varphi)$  are as-yet-undetermined functions of latitude only, and

$s$  = zonal wave number = 0, 1, 2...

$\sigma$  = frequency,  $\sigma < 0 \rightarrow$  eastward moving

$\sigma > 0 \rightarrow$  westward moving .

The superscripts  $(\sigma, s)$  simply denote the particular frequency and zonal wave number associated with each mode. The subscript  $n$  is introduced to recognize the possibility of multiple solutions, and the summation over  $n$  represents a superposition of these solutions. It

can be shown that the set  $\{\Theta_n^{\sigma,s}(\varphi)\}$  for all  $n$  is *complete* for  $-\frac{\pi}{2} \leq \varphi \leq \frac{\pi}{2}$ . At this point, we do not know what meridional structures are represented by the  $\Theta_n^{\sigma,s}(\varphi)$ .

After several pages of manipulation, we can derive the following two equations:

$$F(\Theta_n^{\sigma,s}) = -\epsilon_n \Theta_n^{\sigma,s}, \quad (8.9)$$

$$\frac{d^2 W_n^{\sigma,s}}{dp^2} + \frac{S_p}{gh_n} W_n^{\sigma,s} = -\frac{R}{gh_n c_p} \left( \frac{J_n^{\sigma,s}}{p} \right). \quad (8.10)$$

Here  $F$  is a linear operator:

$$F \equiv \frac{d}{d\mu} \left( \frac{1-\mu^2}{v^2-\mu^2} \frac{d}{d\mu} \right) - \frac{1}{(v^2-\mu^2)} \left[ \frac{s}{v} \left( \frac{v^2+\mu^2}{v^2-\mu^2} \right) + \frac{s^2}{1-\mu^2} \right]; \quad (8.11)$$

$v \equiv \frac{\sigma}{2\Omega}$  is the *normalized* frequency; and  $\mu \equiv \sin \varphi$ , so that  $d\mu \equiv \cos \varphi d\varphi$ . We have introduced the nondimensional quantity

$$\epsilon_n \equiv \frac{4\Omega^2 a^2}{gh_n}. \quad (8.12)$$

The quantity  $h_n$ , which appears in (8.10) and (8.12), is a “separation constant,” because it arises during the separation of variables. It is called the “equivalent depth,” for reasons that will become clear later.

Not surprisingly, Eq. (8.9) is called the meridional structure equation, and Eq. (8.10) is called the vertical structure equation. Recall that we have derived these equations using the assumptions that the basic state is at rest, and that the temperature depends on pressure (i.e. height) only. Separation of variables is not possible if the basic state is made more realistic, e.g., if the observed zonally averaged temperature and winds are used.

Eq. (8.9) was derived by Laplace about 200 years ago. It is often called the Laplace Tidal Equation, or LTE. It is a second-order ordinary differential equation, and so two boundary conditions are needed. It suffices to assume that the  $\Theta_n^{\sigma,s}$  are bounded at the poles, i.e. at  $\mu = -1$  and  $1$ . Note that (8.9) and its boundary conditions are satisfied quite nicely by the trivial solution  $\Theta_n^{\sigma,s} \equiv 0$ . Non-trivial solutions do exist, but only for particular choices of the parameters  $v$  and/or  $h_n$  (or  $\epsilon_n$ ). If these parameters are chosen “at random,” the *only* solution of (8.9) that satisfies the boundary conditions is the trivial solution  $\Theta_n^{\sigma,s} \equiv 0$ . A

problem of this type is called an “eigenvalue” problem. The frequencies and/or equivalent depths that allow non-trivial solutions are the eigenvalues, and the  $\Theta_n^{\sigma,s}$  are the eigenfunctions or eigenvectors, which (for this particular problem) are called *Hough functions*.

All information about the planetary radius, rotation rate, and gravity is “buried” in the parameters  $\varepsilon_n$  and  $\nu$ . The parameter  $\varepsilon_n$  is sometimes called by the imposing name “the terrestrial constant.” Because it contains only two non-dimensional parameters characterizing the planet, the LTE does not “know” or “care” very much about the particular planet to which it is being applied. For given  $\nu$  and  $\varepsilon_n$ , the eigenvalues and eigenfunctions of (8.9) are the same for all planets, provided that the atmosphere in question is shallow compared to the planetary radius. This means that the solutions of (8.9) have a very broad applicability.

The vertical structure equation, (8.10), is a second-order ordinary differential equation for  $W_n^{\sigma,s}(p)$ . For now we regard  $J_n^{\sigma,s}$  as known, so that (8.10) contains the single unknown  $W_n^{\sigma,s}$ . The assumption that  $J_n^{\sigma,s}$  is known means that  $J_n^{\sigma,s}$  is at least approximately independent of the motion. This assumption would be reasonable for heating due to absorption of solar radiation by ozone, but it would be completely inappropriate for cumulus heating, for example. At the top of the atmosphere we apply the boundary condition

$$W_n^{\sigma,s} = 0 \text{ at } p = 0. \quad (8.13)$$

This is exact. The *exact* lower boundary condition (in the absence of mountains) is  $w \equiv \frac{Dz}{Dt} = 0$  at  $p = p_S(\lambda, \varphi, t)$ . We apply the *linearized* boundary condition

$$\frac{Dz}{Dt} \equiv \left( \frac{\partial z'}{\partial t} \right)_p + \bar{\omega}' \frac{\partial z}{\partial p} = 0 \text{ at } p = p_0. \quad (8.14)$$

Here  $p_0$  is the spatially and temporally constant value of  $p_S$  in the basic state. Because

$$gz' = \phi' - \Phi, \quad (8.15)$$

where  $\Phi(\lambda, \varphi, t)$  is known, and using the hydrostaticity of the basic state, as expressed by

$$g \left( \frac{\partial z}{\partial p} \right)_{p=p_0} = -\bar{\alpha}_0 = -\frac{R\bar{T}_0}{p_0} \equiv -g \frac{H_0}{p_0}, \quad (8.16)$$

we can rewrite the linearized lower boundary condition (8.14) as

$$\frac{\partial \phi'}{\partial t} - \omega' g \frac{H_0}{p_0} = \frac{\partial \Phi}{\partial t} \text{ at } p = p_0. \quad (8.17)$$

This involves both  $\phi'$  and  $\omega'$ . After some additional algebra to eliminate  $\phi'$  in (8.17), we can finally express the lower boundary condition entirely in terms of  $W_n^{\sigma,s}$ , as

$$\frac{dW_n^{\sigma,s}}{dp} - \frac{H_0}{h_n} \frac{W_n^{\sigma,s}}{p_0} = \frac{i\sigma}{gh_n} G_n^{\sigma,s} \text{ at } p = p_0. \quad (8.18)$$

Note that the gravitational forcing enters the problem through the lower boundary condition on the vertical structure equation. The thermal forcing enters through the vertical structure equation itself. The gravitational and thermal forcings do not appear in the LTE.

### 8.2.2 Free oscillations of the first and second kinds

A free oscillation is one for which there is no thermal or gravitational forcing. When there is *no thermal forcing* the vertical structure equation (8.10) reduces to

$$\frac{d^2 W}{dp^2} + \frac{S_p}{gh} W = 0. \quad (8.19)$$

Here the superscripts  $(\sigma, s)$  and the subscript  $n$  have been dropped for simplicity. When there is *no gravitation forcing* the surface boundary condition (8.18) can be simplified to

$$\frac{dW}{dp} - \frac{H_0}{h} \frac{W}{p_0} = 0 \text{ at } p = p_0. \quad (8.20)$$

We also have

$$W = 0 \text{ at } p = 0. \quad (8.21)$$

The system (8.19) - (8.21) has non-trivial solutions only for special values of  $h$ . These eigenvalues are denoted by  $\hat{h}$ . For  $h \neq \hat{h}$ , only the trivial solution [i.e.  $W(p) \equiv 0$ ] exists. In order to find the  $\hat{h}$  and the corresponding solutions for  $W(p)$ , we have to specify the static stability  $S_p$  as a function of height. Different choices for  $S_p$  will give different  $h$  and  $W(p)$ .

For the case of free oscillations, the solution procedure is summarized in Fig. 8.2. Note that in this case we have *two* eigenvalue problems: One from the vertical structure equation, and a second from the LTE. In the vertical structure problem, the eigenvalues are the equivalent depths. In the meridional structure problem, the eigenvalues are the frequencies.

As a very simple example, suppose that  $S_p = 0$ . Then we find from (8.19) that

$$\frac{d^2 W}{dp^2} = 0. \quad (8.22)$$

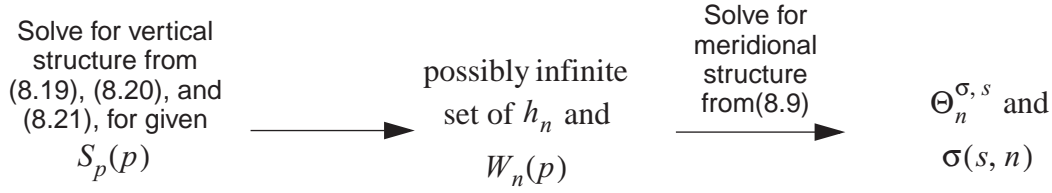


**Figure 8.2:** The solution procedure for free oscillations. The vertical structure equation is solved first, yielding the equivalent depths as eigenvalues. The frequencies are then obtained as eigenvalues of the LTE.

A solution of (8.22) that is consistent with the upper boundary condition (8.21) is

$$W = Ap, \quad (8.23)$$

where  $A$  is an arbitrary constant. Use of (8.23) in the lower boundary condition (8.20) gives

$$\hat{h} = H_0. \quad (8.24)$$

This is the only possible equivalent depth for free oscillations of an isentropic atmosphere. *With more general stratifications there can be many (infinitely many) equivalent depths.* As mentioned earlier, this is why we need the subscript  $n$ , i.e. we use  $n$  to denote a particular solution. The procedure used to find the equivalent depth in this simple example can also be used for other stratifications.

With  $\hat{h}$  given by (8.24), nontrivial solutions of (8.9) exist only when there is a special relation (called the dispersion relation) among  $v$ ,  $s$ , and  $n$ . We refer to  $n$  as the “wave type.” The Hough functions (i.e., the solutions of the LTE) have been tabulated by Longuet-Higgins (1968) and others. Here we consider only some limiting cases. First suppose that there is no rotation, so that  $v = \frac{\sigma}{2\Omega} \rightarrow \infty$ . We continue to assume that  $S_p = 0$  so that (8.24) applies. For this case, find that

$$v^2 F \rightarrow \frac{d}{d\mu} \left[ (1 - \mu^2) \frac{d}{d\mu} \right] - \frac{s^2}{1 - \mu^2}, \quad (8.25)$$

and

$$v^2 \varepsilon \rightarrow \frac{\sigma^2 a^2}{g \hat{h}} = \frac{\sigma^2 a^2}{g H_0}. \quad (8.26)$$

Then the LTE reduces to



$$\frac{d}{d\mu} \left[ (1 - \mu^2) \frac{d\Theta}{d\mu} \right] + \left( \frac{\sigma^2 a^2}{gH_0} - \frac{s^2}{1 - \mu^2} \right) \Theta = 0. \quad (8.27)$$

It can be shown that (8.27) has solutions that are bounded as  $\mu \rightarrow \pm 1$  only for

$$\frac{\sigma^2 a^2}{gH_0} = n(n+1), \quad n = 1, 2, 3 \dots \quad (8.28)$$

These frequencies that satisfy (8.28) are eigenvalues. The eigenfunctions, i.e., the nontrivial solutions of (8.27), are called associated Legendre functions of order  $n$  and rank  $s$ , denoted by

$$\Theta_n = P_n^s(\mu), \quad n \geq s. \quad (8.29)$$

Note that  $n$  and  $s$  are both integers such that  $n \geq s$ . The  $P_n^s$  are discussed in the Appendix. When (8.29) is combined with the longitudinal structure shown in (8.7), we find that the horizontal structure of the waves is given by

$$Y_n^s(\mu, \lambda) = P_n^s(\mu) \exp(is\lambda). \quad (8.30)$$

These are the spherical harmonics (see the Appendix on this topic). Here  $n$  is the total number of nodal circles,  $s$  is the zonal wave number, and  $n - s$  is the number of nodes in the meridional direction, also known as the “meridional nodal number.”

The solutions found here are external gravity waves. They are called “external” because they have no nodes in the vertical and they do not propagate vertically. A stratified (i.e., non-isentropic) atmosphere can support both external and internal gravity waves.

The frequencies can be written as

$$\sigma = \pm \frac{\sqrt{n(n+1)gH_0}}{a}; \quad (8.31)$$

they depend on the wave’s horizontal scale through the two-dimensional index,  $n$ , but they are *independent of  $s$* . For example, when  $n = 1$ ,  $s$  can be either 0 or 1 (because  $n \geq s$  and  $s \geq 0$ , but both modes have the same frequency. This is not true when rotation is present, because with rotation the zonal direction (in which scale is measured by  $s$ ) becomes physically “different” from the meridional direction. A non-isentropic atmosphere can support both external and internal gravity waves.

Now consider  $\Omega \neq 0$ , still for an isentropic atmosphere, and neglect all details. Define a stream function  $\psi$  and a velocity potential  $\chi$  so that

$$\begin{aligned}
u' &= -\frac{1}{a} \left( \frac{\partial \psi}{\partial \phi} \right)_p + \frac{1}{a \cos \phi} \left( \frac{\partial \chi}{\partial \lambda} \right)_p, \\
v' &= \frac{1}{a \cos \phi} \left( \frac{\partial \psi}{\partial \lambda} \right)_p + \frac{1}{a} \left( \frac{\partial \chi}{\partial \phi} \right)_p.
\end{aligned}
\tag{8.32}$$

The vorticity is then  $\xi_p = \mathbf{k} \cdot (\nabla_p \times \mathbf{V}_h) = \nabla_p^2 \psi$ , and the divergence is  $\delta_p = \nabla_p \cdot \mathbf{V}_h = \nabla_p^2 \chi$ . The equation of horizontal motion leads to

$$\frac{\partial}{\partial t} \nabla_p^2 \psi + \left( \frac{2\Omega \cos \phi}{a} \right) v' + 2\Omega \sin \phi (\nabla_p^2 \chi) = 0
\tag{8.33}$$

(the vorticity equation) and

$$\frac{\partial}{\partial t} \nabla_p^2 \chi + \left( \frac{2\Omega \cos \phi}{a} \right) u' - 2\Omega \sin \phi (\nabla_p^2 \psi) = -g \nabla_p^2 z'
\tag{8.34}$$

(the divergence equation). We can also show (see the problems at the end of this chapter) that for an isentropic atmosphere

$$\frac{\partial z'}{\partial t} + H_0 \nabla_p^2 \chi = 0.
\tag{8.35}$$

Equations (8.33) through (8.35) form a closed set that can be solved for  $\psi$ ,  $\chi$ , and  $z'$ .

From (8.33) and (8.35) we see that when  $\Omega \neq 0$  stationary motion cannot exist unless  $v' = 0$ . For nontrivial stationary motion with  $v' = 0$  it follows from (8.2) that  $s = 0$ , i.e. the motion must be both purely zonal and zonally uniform.

Margules (1893) and Hough (1898) showed that the LTE has two classes of solutions, which they named Free Oscillations of the First and Second Classes. For the case of

$\epsilon_n \equiv \frac{4\Omega^2 a^2}{g h_n}$  small (weak rotation), we can obtain approximate solutions of (8.33) and (8.34)

by expanding in spherical harmonics (see Longuet-Higgins, 1968). These Free Oscillations of the First Class (FOFC) are essentially gravity waves, satisfying

$$\left. \begin{aligned}
\chi &\equiv A_n^s P_n^s(\mu) e^{i(s\lambda + \sigma t)} \\
\psi &\equiv 0 \quad (\text{irrotational}) \\
\sigma^2 &\equiv \frac{g H_0}{a^2} n(n+1)
\end{aligned} \right\}.
\tag{8.36}$$

Compare with (8.31), obtained for  $\Omega = 0$ . Haurwitz (1937) obtained a more accurate expression for the frequency of the FOFC:

$$\sigma \equiv \frac{\Omega s}{n(n+1)} \pm \sqrt{\frac{\Omega^2 s^2}{n^2(n+1)^2} + n(n+1) \frac{gH_0}{a^2}}. \quad (8.37)$$

This should be compared with (8.31). For large  $n$ , (8.37) reduces to (8.31). The additional terms in (8.37) involve  $\Omega$ . For  $n \geq 4$  the error in (8.37) is less than 1%. From (8.37) we see that eastward propagating inertia gravity waves have frequencies slightly different from those of westward propagating inertia gravity waves. The difference is due to rotation.

The Free Oscillations of the Second Kind (FOSC) are the so-called Rossby-Haurwitz waves, which satisfy

$$\left. \begin{aligned} \psi &\equiv iB_n^s P_n^s(\mu) e^{i(s\lambda + \sigma t)} \\ \chi &\equiv 0 \quad (\text{nondivergent}) \\ \sigma &\equiv \frac{2\Omega s}{n(n+1)} > 0 \end{aligned} \right\}. \quad (8.38)$$

Note that, since  $\sigma > 0$ , the FOFC always move westward. They are nearly nondivergent. They can be found by assuming  $\chi = 0$  from the beginning, as follows: For  $x = 0$ , Eq. (8.33) reduces to

$$\frac{\partial}{\partial t} \nabla^2 \psi + \frac{2\Omega}{a^2} \frac{\partial \psi}{\partial \lambda} = 0. \quad (8.39)$$

Therefore

$$i\sigma \left\{ \frac{1}{a^2 \cos^2 \varphi} \left[ \cos \varphi \frac{d}{d\varphi} \left( \cos \varphi \frac{d\hat{\psi}}{d\varphi} \right) - s^2 \hat{\psi} \right] \right\} + \frac{2\Omega i s}{a^2} \hat{\psi} = 0, \quad (8.40)$$

or

$$\frac{d}{d\mu} \left[ (1 - \mu^2) \frac{d\hat{\psi}}{d\mu} \right] + \left( \frac{2\Omega s}{\sigma} - \frac{s^2}{1 - \mu^2} \right) \hat{\psi} = 0. \quad (8.41)$$

This is another eigenvalue problem. The solution of (8.41) is  $\hat{\psi} = B_n^s P_n^s(\mu)$ . Note that for Rossby-Haurwitz waves, in contrast to pure gravity waves,  $\sigma$  does depend explicitly on  $s$ .

The westward propagation of Rossby-Haurwitz waves is due to the Earth's sphericity. To see this, rewrite (8.39) as

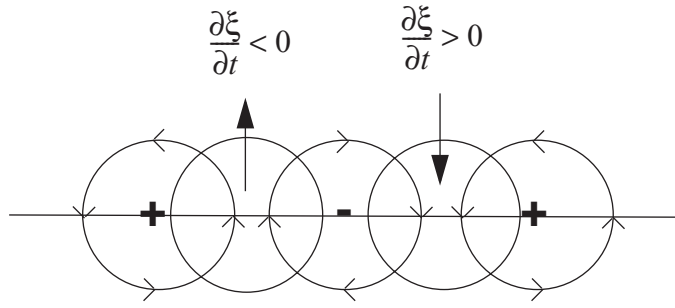


Figure 8.3: Chain of vortices along a latitude circle, illustrating the westward propagation of Rossby waves.

$$\frac{\partial \xi}{\partial t} + \beta v = 0, \quad (8.42)$$

where

$$\beta \equiv \frac{2\Omega \cos \varphi}{a} = \frac{1}{a} \frac{df}{d\varphi}. \quad (8.43)$$

Note that  $\beta \geq 0$ . Consider a chain of vortices along a latitude circle, as shown in Fig. 8.3. In places where  $v > 0$ ,  $\beta v > 0$ , so  $\frac{\partial \xi}{\partial t} < 0$ . This occurs to the west of the place where  $\xi < 0$ . Similarly, where  $v < 0$ ,  $\beta v < 0$ , so  $\frac{\partial \xi}{\partial t} > 0$ . This occurs to the west of the place where  $\xi > 0$ .

A direct test of the theory of non-divergent Rossby waves was made by Eliassen and Machenhauer (1965) and Deland (1965). They performed a spherical-harmonic analysis of the 500 mb stream function, isolating transient waves by taking the difference in 24 hours. Their results, illustrated in Fig. 8.4, show westward propagation. Table 8.1 compares the computed and observed phase speeds, in degrees of longitude per day. The model overpredicts the westward phase speeds. This error is due to our neglect of the effects of divergence. Table 8.2 gives examples of the periods of the FOFC and FOSC.

### 8.3 Observations of stationary and transient eddies in middle latitudes

Blackmon (1976) discussed the observed eddy activity in the Northern Hemisphere, as seen in the 500 mb geopotential height. He used a ten-year record, and considered both summer and winter conditions. The data were available twice per day, at 00 Z and 12 Z.

Blackmon filtered the data in both space and time, in order to isolate particular space-time scales. He expanded the height fields into spherical harmonics  $Y_n^m$  (see the Appendix on spherical harmonics), where subscript  $m$  denotes the zonal wave number, and subscript  $n$  denotes the “two dimensional index.” The number of nodes in the meridional direction, i.e. the “meridional nodal number” (try saying that five times, fast) is  $n - m \geq 0$ ; note that  $m \leq n$  is required. The largest value of  $n$  considered by Blackmon was  $n = 18$ . Note that  $m = 18$

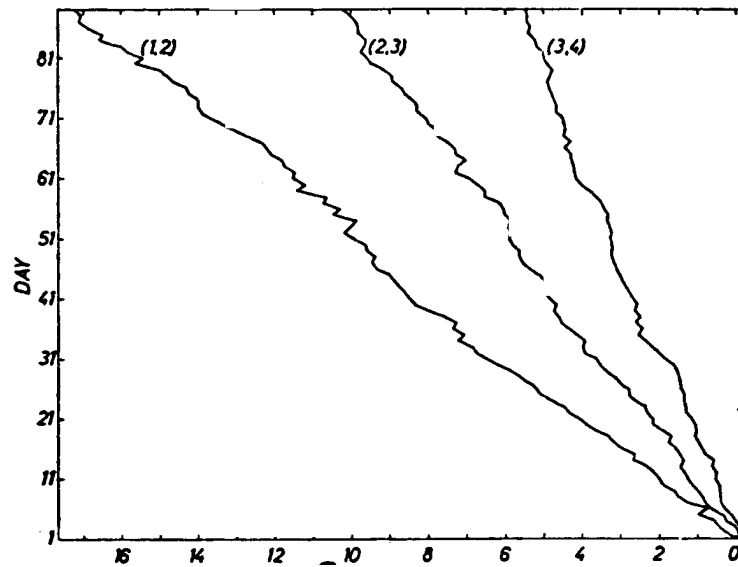


Figure 8.4: Successive daily values of the phase angle for the 24 hour tendency field,  $\psi_{s,n}(t+1) - \psi_{s,n}(t)$ , at the 500 mb level for the components  $(s, n) = (1, 2), (2, 3), (3, 4)$ , during the 90 day period beginning 1 December 1956. The ordinate is time, in days. The abscissa represents the number of westward circulations round the Earth after the first passage of the Greenwich meridian, and so it is a measure of longitudinal phase propagation. From Eliassen and Machenhauer (1965).

$(s, n)$	$c_{R-H}$	$c_{obs}$
(1,2)	-115	-70
(2,3)	-53	-40
(3,4), (1,4)	-28	-20
(2,5)	-16	-12
(3,6)	-9	-8

Table 8.1: Predicted and observed phase speeds of Rossby-Haurwitz modes, in degrees of longitude per day.

corresponds to a zonal wave length of  $20^\circ$  of longitude, which in middle latitudes corresponds to a wavelength of roughly 1000 km.

<i>n</i>	<i>s</i>	<i>First Class To West, hours</i>	<i>First Class To East, hours</i>	<i>Second Class Only to West, days</i>
1	1	13.76	39.34	1.21
2	1	10.92	14.50	5.37
	2	11.80	18.10	1.64
3	1	9.11	10.09	8.75
	2	9.23	10.96	3.87
	3	9.63	12.17	2.10
4	1	7.65	7.99	12.78
	2	7.65	8.28	6.11
	3	7.75	8.66	3.79
	4	7.94	9.18	2.56
5	1	6.52	6.67	17.75
	2	6.52	6.79	8.70
	3	6.52	6.95	5.62
	4	6.58	7.24	3.92
	5	6.69	7.49	3.05

**Table 8.2:** Periods of the free oscillations on the sphere, as computed from theory. Note that the periods of the gravity waves are given in hours, while those of the Rossby waves are given in days. From Phillips (1963).

The spherical harmonics form a complete orthonormal basis that can be used to represent an arbitrary function on the sphere (see the Appendix). Using the spherical harmonics, the data can be expanded as follows:

$$Z(\lambda, \varphi) = \sum_{n=-m}^m \sum_{m=0}^n C_n^m Y_n^m. \quad (8.44)$$

Here the  $C_n^m$  are the expansion coefficients. Blackmon defined three groups of spatial scales, based on the two-dimensional index:

**Regime I:**  $0 \leq n \leq 6$ , or “long waves;”

**Regime II:**  $7 \leq n \leq 12$ , or “medium-scale waves;” and

**Regime III:**  $13 \leq n \leq 18$ , or “short waves.”

Because Blackmon’s truncation scheme is based on the two-dimensional index, a particular wave can have nodes in the zonal direction or in the meridional direction, most have both. Note that for all three regimes  $0 \leq m \leq n$ . All three regimes therefore contain modes with small values of  $m$ , i.e. long zonal scales.

The expansion coefficients for each set of waves can be determined for each observation time. They were filtered in time, using three filters:

*Low pass:* Admits periods in the range longer than or equal to 10 days;

*Medium-pass:* Admits periods in the range 2.5 days to 6 days;

*High-pass:* Admits periods in the range 1 day to 2 days.

Note that a period of one day represents the most rapidly fluctuating wave that can be captured by the twice-a-day data that was used in Blackmon’s study.

The lower panel of Fig. 8.5 shows the time-averaged 500 mb height averaged over nine winters. The features seen here are stationary waves. Note the two prominent troughs, one near the east coast of North America, and the other near Japan. These same features can be seen in the figures of Chapter 2, of course.

The upper panel of Fig. 8.5 shows the total root-mean-square (rms) geopotential height, for winter, without time or space filtering. There are three prominent “centers of action,” in the North Pacific, the North Atlantic, and over Siberia.

Fig. 8.6 shows low-pass filtered (long period) rms winter heights, for all spatial scales (top left), for Regime I (top right), for Regime II (bottom left), and for Regime III (bottom right). It is clear that very little contribution comes from Regime III. Both Regime I and Regime II contribute significantly. The Regime II contribution shows maxima in regions where blocking commonly occurs. Blocking will be discussed later.

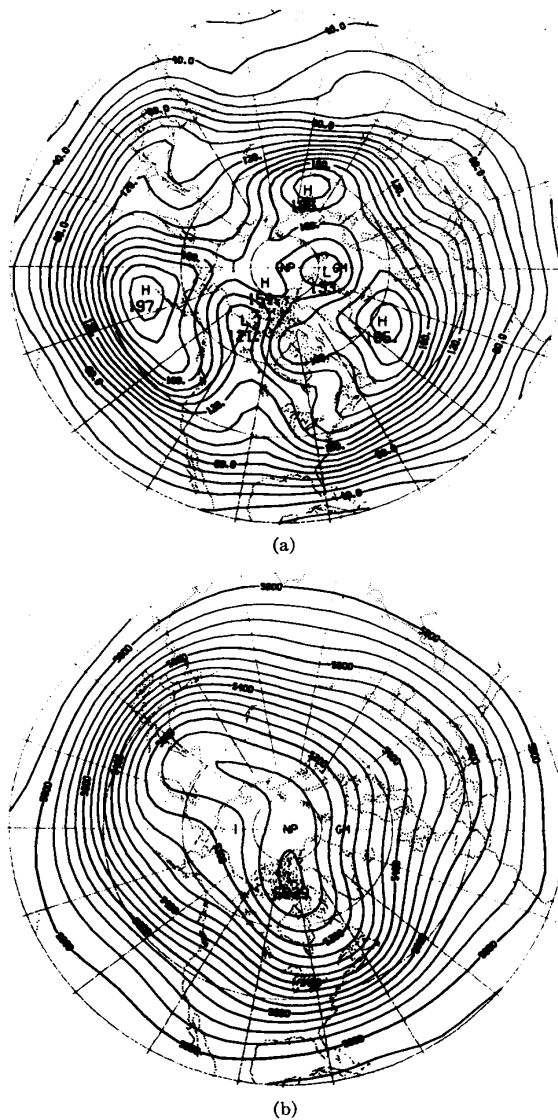


Figure 8.5: Maps of the geopotential height for 9 winters: (a) rms unfiltered, contour interval 10 m; (b) average, contour interval 50 m. From Blackmon (1976).

Fig. 8.7 is similar to Fig. 8.6, but for medium-pass waves, i.e. those of “synoptic” periods in the range of 2.5 to 6 days. For this range of periods, most of the action comes from Regime II and Regime III; the long waves do not contribute much. Note, however, that the contour interval is smaller than that used in Fig. 8.6, so that the total amount of activity indicated in Fig. 8.7 is less.

Even less power resides in high-pass waves (not shown).



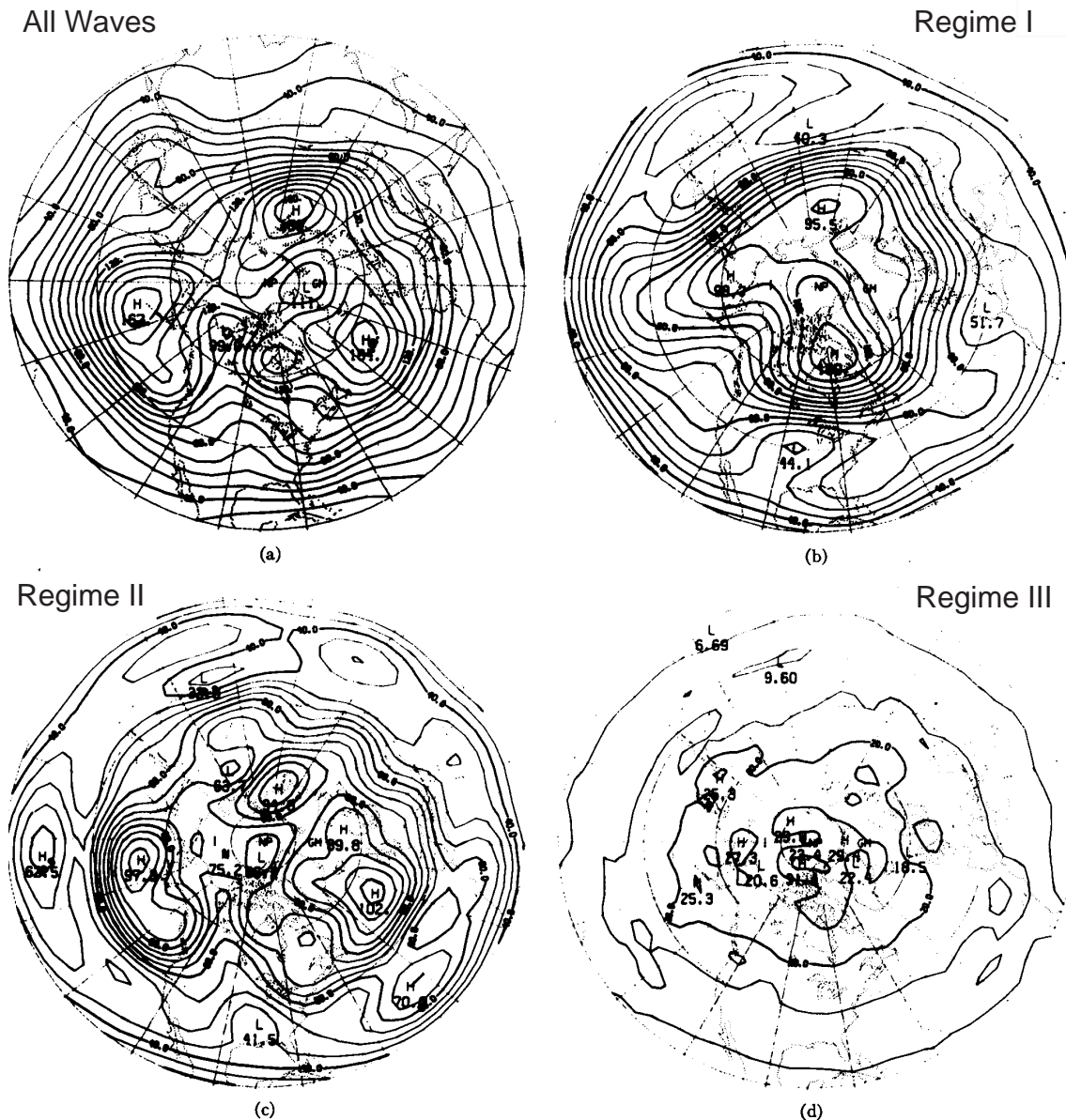
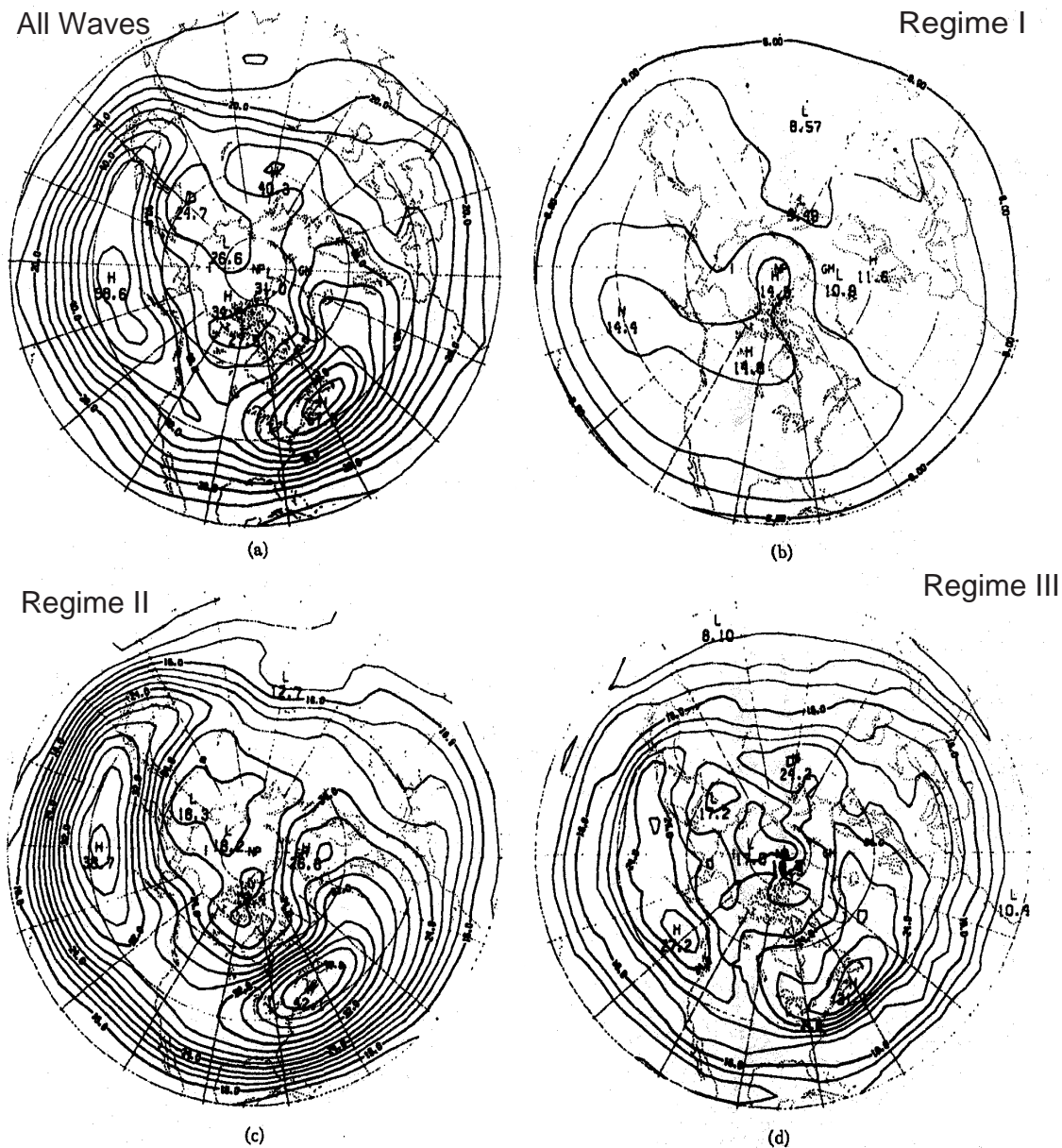


Figure 8.6: Maps of the low-pass filtered rms fields (winter): (a) all waves, contour interval 10 m; (b) waves in Regime I, contour interval 5 m; (c) waves in Regime II, contour interval 5 m; (d) waves in Regime III, contour interval 5 m. From Blackmon (1976).

Table 8.1 shows that in winter the greatest power is found along a “ridge” running from lower left (small  $n$ , low frequency) to upper right (large  $n$ , high frequency). By far the largest power occurs in the low frequencies and for two-dimensional index  $n$  on the order of 6. The diurnal tide is also apparent near the bottom right, with  $n = 2$ .

The corresponding results for the summer season are omitted here for brevity. In summer, the wave amplitudes are greatly reduced, as is the strength of the mean flow, and the centers of action are shifted towards the pole. As in winter, the long waves and low



**Figure 8.7:** Maps of the medium-pass filtered rms fields (winter): (a) all waves, contour interval 5 m; (b) waves in Regime I, contour interval 2 m; (c) waves in Regime II, contour interval 2 m; (d) waves in Regime III, contour interval 2 m. From Blackmon (1976).

frequencies dominate.

One conclusion from Blackmon's study is that most of the transient eddy energy resides at the low frequencies and long wavelengths. This has been known for a long time. For example, Wiin-Nielsen et al. (1963) analyzed the total heat and momentum transport across a latitude circle as a function of wave number for selected latitudes. As shown in Fig.

$n$	Frequency (days) <sup>-1</sup>															
	0	1/15	2/15	3/15	4/15	5/15	6/15	7/15	8/15	9/15	10/15	11/15	12/15	13/15	14/15	15/15
18	51.7	49.8	45.8	39.3	37.0	26.7	21.2	17.3	13.7	10.1	7.2	5.3	4.1	3.4	3.2	3.4
17	68.7	66.5	58.6	48.1	40.1	34.0	27.9	22.1	15.8	11.0	7.6	5.4	4.3	3.1	3.2	3.3
16	98.5	97.5	82.4	69.6	56.5	45.0	34.8	26.0	18.4	12.2	7.9	5.5	4.1	3.3	3.3	3.5
15	141.6	131.0	108.1	85.9	70.3	58.6	75.6	32.3	19.7	11.6	7.3	5.1	4.1	3.3	3.3	3.4
14	210.1	195.5	158.9	122.3	99.5	79.2	53.3	32.3	18.2	10.8	6.9	4.9	3.5	3.3	3.3	3.4
13	302.8	272.5	213.2	164.7	129.0	92.6	56.1	31.6	16.8	9.4	5.7	4.4	3.2	2.9	2.9	3.3
12	502.6	435.2	311.1	225.5	159.9	99.8	53.5	26.8	13.6	8.0	5.3	3.9	3.2	3.0	3.0	3.4
11	746.3	639.7	443.3	290.6	176.5	94.4	43.8	21.1	10.6	6.0	4.1	3.6	3.0	2.8	3.0	3.4
10	1190.1	943.3	545.9	322.8	181.0	80.5	33.6	15.6	8.3	5.4	3.9	3.3	3.0	2.9	3.1	3.6
9	1815.2	1417.6	739.3	323.8	135.8	55.0	23.2	11.4	6.1	4.1	3.1	2.8	2.4	2.7	2.9	3.6
8	3305.7	2175.9	732.7	245.2	104.5	42.0	17.3	9.1	4.3	3.6	2.3	2.6	2.2	2.7	2.5	3.4
7	3732.6	2370.4	698.2	191.2	71.2	29.3	12.9	7.7	3.8	3.6	2.3	2.9	1.9	2.6	2.5	4.3
6	3731.5	2374.2	657.5	149.3	51.0	20.6	9.0	5.8	2.4	2.8	1.3	2.3	1.5	2.4	2.3	4.2
5	3563.5	2192.6	522.5	114.0	39.1	16.2	7.1	4.9	3.4	2.7	2.2	2.2	2.2	2.2	2.6	4.8
4	2553.1	1600.8	420.2	95.1	34.5	13.8	5.7	4.2	2.1	2.6	1.5	2.1	1.3	2.0	2.1	3.8
3	1448.2	992.6	329.2	79.7	27.0	9.4	4.6	3.3	2.1	1.8	1.4	1.5	1.2	1.5	5.3	4.6
2	1115.3	642.0	146.3	41.8	18.5	8.3	3.3	2.3	1.6	1.6	1.1	1.3	1.2	1.4	2.2	3.7
1	294.5	221.7	105.9	45.1	15.8	4.1	2.0	1.7	1.2	1.0	0.9	1.0	1.0	1.1	6.0	12.4
0	168.6	92.6	17.1	4.7	2.5	1.4	1.0	0.8	0.6	0.6	0.6	0.6	0.6	0.6	1.8	3.5

Table 8.1: Power as a function of wave number and frequency for the winter season. Units: m<sup>2</sup> rad<sup>-1</sup> (15 days)<sup>-1</sup>

8.8, by far the strongest contributions come from zonal wave numbers less than 10. For middle latitudes, this corresponds to wave lengths longer than 2000 km. The results show that the waves of largest spatial scale do most of the work of transporting energy and momentum poleward; the “synoptic-scale” and mesoscale eddies that we think of as “weather” play only a relatively minor role. They are fleas on the back of the general circulation.

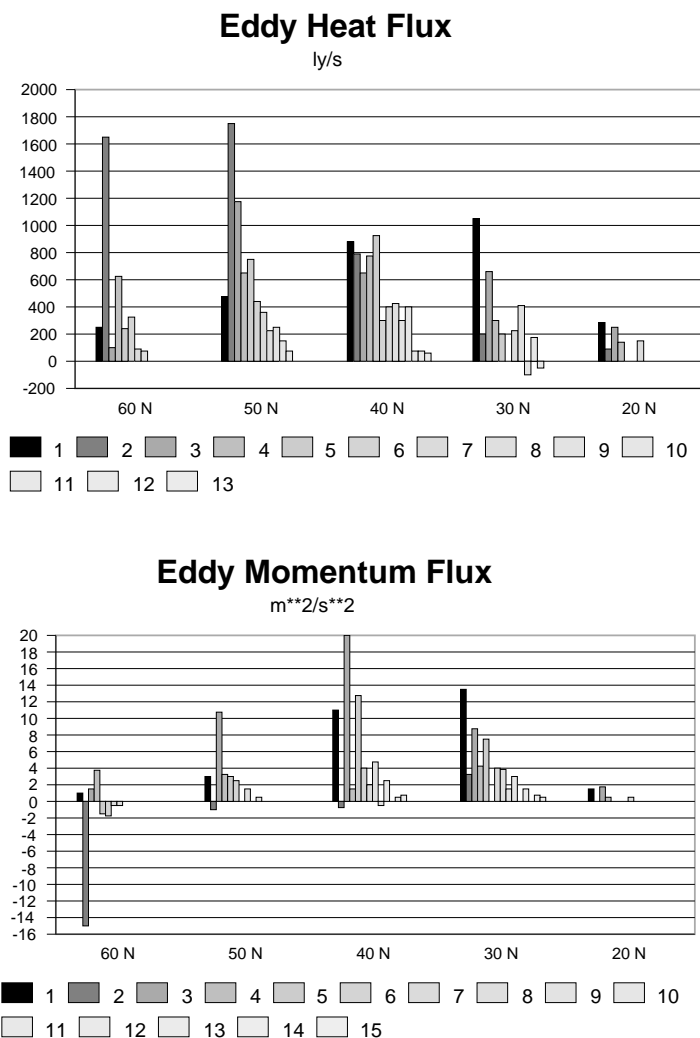


**Figure 8.8:** Upper panel: The total eddy heat transport across a latitude circle as a function of wave number for selected latitudes, for January 1962. Lower panel: The eddy momentum transport averaged with respect to pressure, as a function of zonal wave number, for selected latitudes, based on observations for January 1962. In both panels the gray scale at the bottom denotes the zonal wave number. From Wiin-Nielsen et al. (1963).

#### 8.4 Theory of orographically forced stationary waves

Stationary waves are forced by mechanical and/or thermal effects that are anchored to the Earth's surface. Mountain ranges can produce waves either by orographic forcing (i.e., by blocking the flow) or by acting as elevated heat sources. Thermal forcing is also associated with land-sea contrasts, sea surface temperature gradients, and the like.

Held (1983) summarized the work of Charney and Eliassen (1949), who tried to understand the effects of orographic barriers on stationary waves in middle latitudes. The starting point is consideration of the conservation of potential vorticity in shallow water (see

the Appendix on the shallow water equations), with the quasigeostrophic approximation, i.e.

$$\left(\frac{\partial}{\partial t} + \mathbf{V}_g \cdot \nabla\right)q = -\left(\frac{r\zeta}{h - h_T}\right), \quad (8.45)$$

where

$$q \equiv \frac{\zeta + f}{h - h_T}. \quad (8.46)$$

Here  $h$  is the height of the free surface,  $[h]$  is the zonally averaged value of  $h$ ,  $h_T(x)$  is the height of the topography, assumed to vary in the  $x$ -direction only,  $h^* = h - [h]$ ,  $\mathbf{V}_g$  is the geostrophic wind, and  $r$  is a Rayleigh friction coefficient. See Fig. 8.9. We use the quasi-

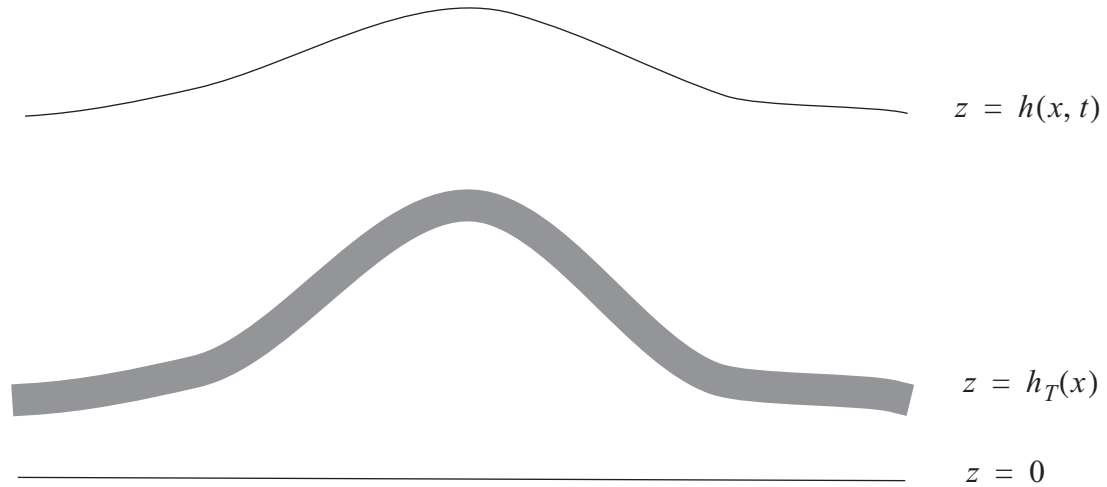


**Figure 8.9:** Schematic illustrating shallow water flowing over a “mountain.”

geostrophic approximation, with

$$\mathbf{V}_g = \frac{g}{f_0} \mathbf{k} \times \nabla h \quad \text{and} \quad \zeta = \frac{g}{f_0} \nabla^2 h. \quad (8.47)$$

We linearize about the zonally averaged state, which is assumed to be geostrophically balanced. Using (8.46) and (8.48), we can show that the zonal wind of the basic state satisfies

$$[u] = -\frac{g}{f_0} \frac{\partial}{\partial y} [h]. \quad (8.48)$$

We assume that  $[u]$  is independent of  $y$  as well as  $x$  and  $t$ . The potential vorticity gradient of

the zonally averaged flow is given by

$$[h] \frac{\partial}{\partial y} [q] = \beta + \frac{f_0^2 [u]}{g[h]}. \quad (8.49)$$

In linearizing about the basic state given by (8.48) and (8.49), we assume not only that the perturbation vorticity and height are small, but also that  $h_T$  is small compared to  $[h]$ , so that we can neglect any products of  $h_T$  with a perturbation quantity. The linearized version of (8.45) is then

$$\left( \frac{\partial}{\partial t} + [u] \frac{\partial}{\partial x} \right) q^* + v^* \frac{\partial}{\partial y} [q] = - \frac{r \zeta^*}{[h]}. \quad (8.50)$$

where all perturbation quantities can be expressed in terms of  $h^*$ , as follows:

$$v^* = \frac{g \partial h^*}{f_0 \partial x}, \quad (8.51)$$

$$\zeta^* = \frac{g}{f_0} \nabla^2 h^*, \quad (8.52)$$

$$\begin{aligned} [h] q^* &= \zeta^* - f_0 \frac{(h^* - h_T)}{[h]} \\ &= \frac{g}{f_0} \nabla^2 h^* - f_0 \frac{(h^* - h_T)}{[h]}. \end{aligned} \quad (8.53)$$

By substitution from (8.49) and (8.51)-(8.53), we can rewrite the perturbation potential vorticity equation, (8.50), as

$$\left( \frac{\partial}{\partial t} + [u] \frac{\partial}{\partial x} \right) \left\{ \frac{g}{f_0} \nabla^2 h^* - f_0 \frac{(h^* - h_T)}{[h]} \right\} + \frac{g \partial h^*}{f_0 \partial x} \left\{ \beta + \frac{f_0^2 [u]}{g[h]} \right\} = - r \frac{g}{f_0} \nabla^2 h^*, \quad (8.54)$$

or, after rearranging,

$$\frac{\partial}{\partial t} \left( \frac{g}{f_0} \nabla^2 h^* - \frac{f_0}{[h]} h^* \right) + \frac{g}{f_0} [u] \frac{\partial}{\partial x} (\nabla^2 h^*) + \beta \frac{g \partial h^*}{f_0 \partial x} + r \frac{g}{f_0} \nabla^2 h^* = - \frac{[u] f_0 \partial h_T}{[h] \partial x}. \quad (8.55)$$

Here some nice cancellation has occurred, and we have placed the “topographic forcing”

term, involving  $\frac{\partial h_T}{\partial x}$ , on the right-hand side, to set it apart. The waves described by (8.55) are “forced” by topography, which enters mathematically through the inhomogeneous term on the right-hand side, i.e.  $-[u]\frac{f_0}{[h]}\frac{\partial h_T}{\partial x}$ . In the presence of such forcing, a non-zero  $h^*$  is demanded by (8.55).

Assume that the perturbations have the form

$$h^* = \text{Re}\{\hat{h}\exp[i(kx + ly - \omega t)]\}, \quad (8.56)$$

where  $\hat{h}$  is a constant, and also that the topography satisfies

$$h_T = \text{Re}\{\hat{h}_T \exp[i(kx + ly)]\}. \quad (8.57)$$

With (8.56), a positive value of  $\omega$  indicates eastward propagation. Note that we could choose  $l = 0$ , which would give us the special case of no meridional variations. Substitution of (8.56) and (8.57) into (8.55) gives:

$$\{-\omega(K^2 + \lambda^{-2}) + k([u]K^2 - \beta) - irK^2\}\hat{h}e^{-i\omega t} = [u]\lambda^{-2}k\hat{h}_T. \quad (8.58)$$

Here  $K$  is the total wave number, which is defined by

$$K^2 \equiv k^2 + l^2, \quad (8.59)$$

and  $\lambda$  is the radius of deformation, which is defined by

$$\lambda^2 \equiv g[h]/f_0^2. \quad (8.60)$$

Note that  $\lambda$  is defined in terms of the basic state. We see directly from (8.58) that the amplitude of the waves, as measured by  $\hat{h}$ , is proportional to the amplitude of the forcing, as measured by  $\hat{h}_T$ . The proportionality factor is rather complicated, however.

First consider the special case in which a free wave exists in the absence of topographic forcing. Then (8.58) reduces to a dispersion formula, which can be written as

$$-\omega(K^2 + \lambda^{-2}) + k([u]K^2 - \beta) - irK^2 = 0, \quad (8.61)$$

or

$$\omega = \frac{k\{[u]K^2 - \beta\} - irK^2}{K^2 + \lambda^{-2}}. \quad (8.62)$$

Eq. (8.62) describes a damped, free Rossby wave in a balanced mean flow. The wave dies out after a finite time because there is no forcing to sustain it against the frictional damping. To see how the friction leads to damping, write

$$\omega = \omega_0 - i(\tau_f)^{-1}, \quad (8.63)$$

where

$$\omega_0 \equiv \frac{k\{[u]K^2 - \beta\}}{K^2 + \lambda^{-2}}, \quad (8.64)$$

and

$$(\tau_f)^{-1} \equiv \frac{rK^2}{K^2 + \lambda^{-2}}. \quad (8.65)$$

Then (8.56) can be rewritten as

$$h^* = e^{-t/\tau_f} \text{Re}\{\hat{h} \exp[i(kx + ly - \omega_0 t)]\}. \quad (8.66)$$

The wave-like solution, with period  $\omega_0$ , decays with  $e$ -folding time  $\tau_f$ .

A stationary wave is one for which  $\text{Re}\{\omega\} = 0$ . Under what conditions can a free Rossby wave be stationary? It is clear from (8.64) that a stationary free wave is possible only for  $[u] > 0$ . The reason is that the Rossby wave propagates toward the west relative to the mean flow, so the mean flow must be *from* the west to hold the wave steady relative to the Earth's surface. In such a case, the total wave number of the stationary wave is

$$K^2 = \beta/[u] \equiv K_S^2. \quad (8.67)$$

Here the subscript  $S$  or  $K_S$  stand for “stationary.”

With this preparation, we return now to the topographically forced case, and assume a stationary, neutral wave, i.e.,  $\omega = 0$ . For the case of *no friction* ( $r = 0$ ), we find from (8.58) that

$$\hat{h} = \frac{\hat{h}_T}{\lambda^2(K^2 - K_S^2)}. \quad (8.68)$$



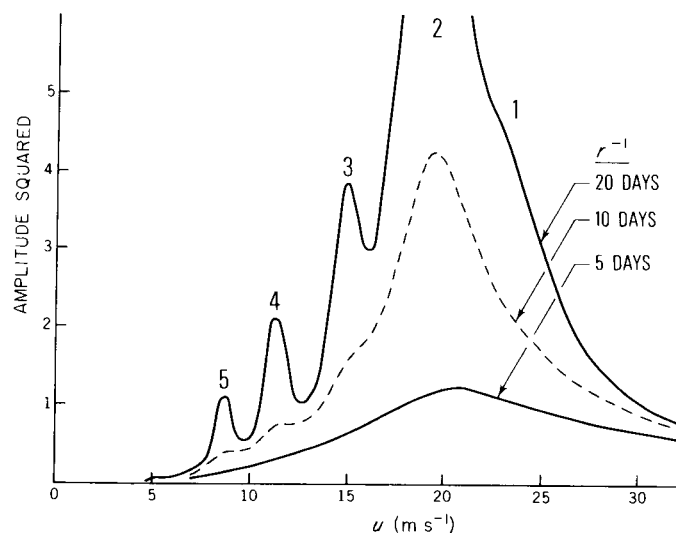
Note that in the absence of friction the forced wave has “infinite amplitude” for  $K^2 = K_S^2$ . This is the phenomenon of resonance, familiar from introductory physics. The infinity can be avoided by turning on the friction, i.e. allowing  $r$  to be positive. With friction, the amplitude of the stationary neutral wave is

$$\hat{h} = \frac{\hat{h}_T}{\lambda^2 \left( K^2 - K_S^2 - i \frac{r K^2}{k[u]} \right)}. \quad (8.69)$$

Eq. (8.69) shows that, mathematically, friction makes the amplitude complex. Clearly the denominator of (8.69) cannot become zero, so long as  $r > 0$ . For  $K^2 = K_S^2$ , (8.69) simplifies to

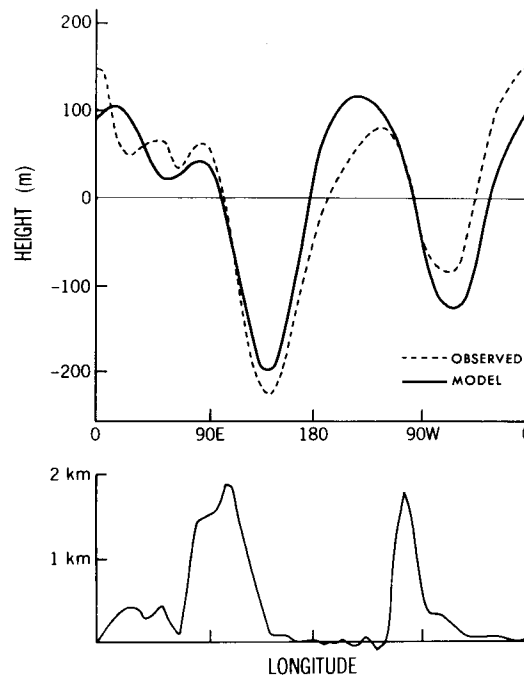
$$\hat{h} = \hat{h}_T \left( \frac{ik\beta}{\lambda^2 r} \right). \quad (8.70)$$

Fig. 8.10 shows how the squared amplitude of the steady-state wave response varies as the zonal wind speed changes, for different values of  $r$ . As shown in Fig. 8.10, the Charney-



**Figure 8.10:** The mean-square height response,  $[(\hat{h}^*)^2]$ , in the Charney-Eliassen model, as a function of  $[u]$ , for different values of the Rayleigh friction coefficient. The units are  $10^4 \text{ m}^2$ . The integers written above the curve indicate the values of  $[u]$  for which particular zonal wave numbers resonate. From Held (1983).

Eliassen model, despite its extreme simplicity, can explain reasonably well the observed zonal structure of the 500 mb height field at  $45^\circ \text{ N}$  in January. This strongly suggests that the observed midlatitude stationary eddies in winter are forced primarily by topography. A similar



**Figure 8.11:** Upper panel: The height response as a function of longitude in the Charney-Eliassen model for  $\tau^{-1} = 5$  days and  $[u] = 17 \text{ m s}^{-1}$  (solid line) and the observed climatological 500 mb eddy heights at  $45^\circ \text{ N}$  in January (dashed line). The lower panel shows the topography used. From Held (1983).

conclusion was reached by Manabe and Terpstra (1974) through numerical experiments with a general circulation model.

Fig. 8.12 shows the observed time-latitude sections of the zonal and meridional contributions to the stationary wave kinetic energy, i.e.  $[u^{*2}]$  and  $[v^{*2}]$ , respectively. In winter, the zonal component is strongest in middle latitudes, and we can think of this as corresponding to the orographically forced waves analyzed above, although of course there is also a thermally forced component. In summer, there is a subtropical maximum of stationary eddy kinetic energy associated with the monsoons, which will be discussed later.

### 8.5 Tropical waves

Matsuno (1966) studied the linearized shallow water equations (see the Appendix on the shallow water equations) applied to an equatorial  $\beta$ -plane. When he began this work, his motivation was to investigate to what extent near-equatorial motions are geostrophic. In the end, however, he discovered two new classes of tropical waves, which soon after were recognized in the observations. These same waves are actually among the solutions found by Laplace, but this was not recognized until later. The model studied by Matsuno turns out to be relevant to a wide variety of phenomena, including monsoons, the Madden-Julian oscillation, the Quasi-Biennial Oscillation, and El Niño. This is amazing, in view of the model's extreme simplicity.

The shallow-water equations on an equatorial  $\beta$ -plane, linearized about a state of rest,

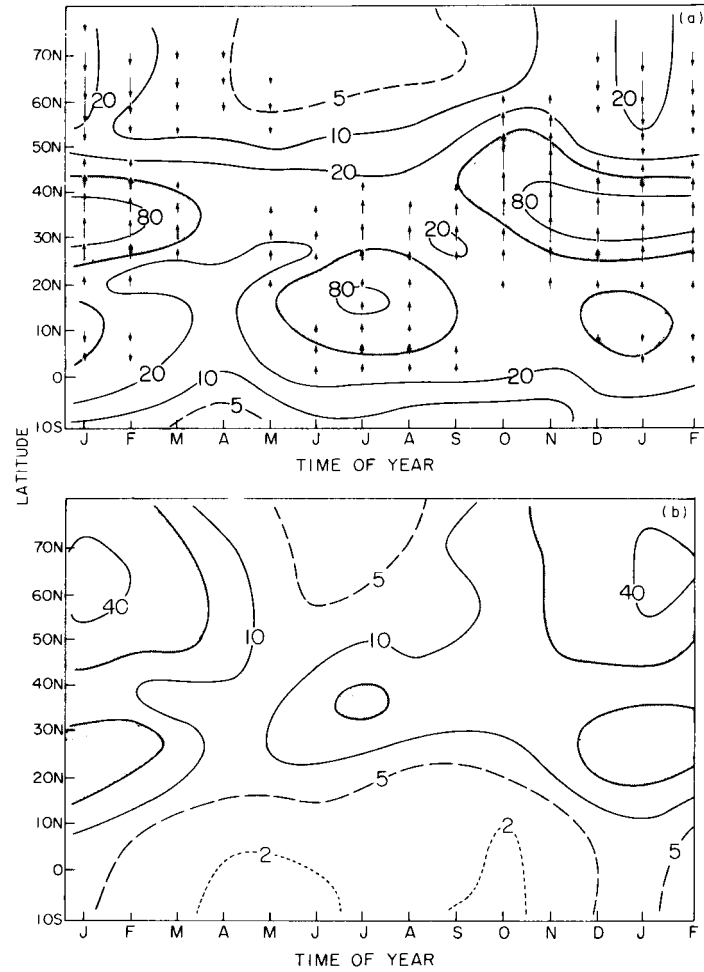


Figure 8.12: Time-latitude sections of Northern Hemisphere climatological mean stationary wave kinetic energy at the 200 mb level, based on data of Oort and Rasmusson (1971). a) Zonal wind component; b) meridional wind component, in units of  $\text{m}^2 \text{s}^{-2}$ . Arrows in a) denote the direction and relative magnitude of the meridional flux of zonal momentum by the stationary waves. From Wallace (1983).

are:

$$\begin{aligned}
 \frac{\partial u}{\partial t} - fv + g \frac{\partial h}{\partial x} &= 0, \\
 \frac{\partial v}{\partial t} + fu + g \frac{\partial h}{\partial y} &= 0, \\
 \frac{\partial h}{\partial t} + H \left( \frac{\partial u}{\partial x} + \frac{\partial v}{\partial y} \right) &= 0.
 \end{aligned} \tag{8.71}$$

Here  $f \equiv \beta y$ , where  $y$  is distance in the meridional direction, measured from  $y = 0$  at the



**Figure 8.13:** A photograph of Prof. T. Matsuno, taken as he gave a lecture at UCLA in January 1998.

Equator (i.e.,  $y = a\phi$ ), and  $\beta \equiv \frac{df}{dy}$  is approximated by a constant value. Of course,  $f = 0$  at the Equator, so that  $f = \beta y$ . Matsuno defined a time scale,  $T \equiv \sqrt{\frac{1}{c\beta}}$ , and a length scale,  $L \equiv \sqrt{\frac{c}{\beta}}$ . Here  $c \equiv \sqrt{gH}$  is the phase speed of a pure gravity wave. These definitions would have to be altered slightly if the Earth's rotation were reversed. Why? See Fig. 8.14 for a sketch defining the other quantities. Fig. 8.15 shows how  $T$  and  $L$  vary as functions of  $c$ . For  $c = 10 \text{ m s}^{-1}$ , we find that  $L \cong 1000 \text{ km}$  and  $T \cong 1 \text{ day}$ . Nondimensionalizing the governing equations by  $T$  and  $L$ , we obtain

$$\begin{aligned}\frac{\partial u}{\partial t} - yv + \frac{\partial \phi}{\partial x} &= 0, \\ \frac{\partial v}{\partial t} + yu + \frac{\partial \phi}{\partial y} &= 0, \\ \frac{\partial \phi}{\partial t} + \frac{\partial u}{\partial x} + \frac{\partial v}{\partial y} &= 0.\end{aligned}\tag{8.72}$$

Here  $\phi$  is the non-dimensional form of  $gh$ .

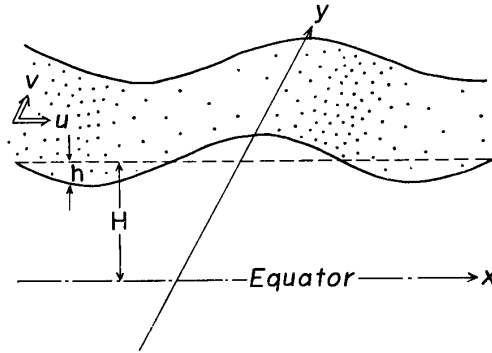


Figure 8.14: Model and coordinate system.  
From Matsuno (1966).

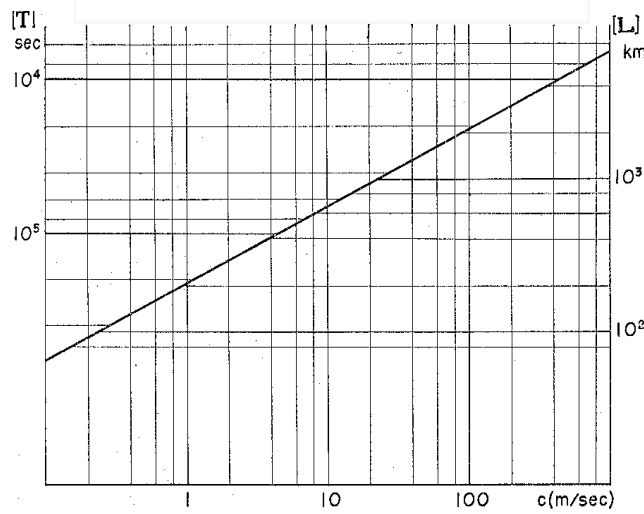
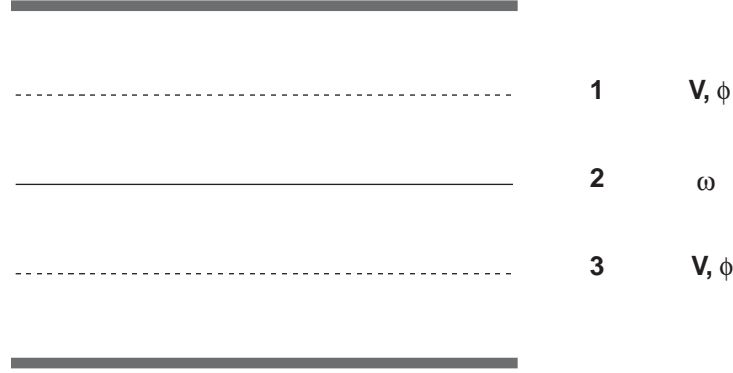


Figure 8.15: Units of time (left scale) and length (right scale) as functions of the phase velocity of a pure gravity wave. From Matsuno (1966).

As a side comment, we note that these equations can actually apply to a model with vertical structure (e.g. McCreary, 1981), and so are more readily applicable to the real atmosphere than one might guess. For example, consider a two-level model:

$$\begin{aligned}
 \frac{\partial \mathbf{V}_1}{\partial t} + f \mathbf{k} \times \mathbf{V}_1 + \nabla \phi_1 &= 0, \\
 \frac{\partial \mathbf{V}_3}{\partial t} + f \mathbf{k} \times \mathbf{V}_3 + \nabla \phi_3 &= 0, \\
 \frac{\partial}{\partial t}(\phi_3 - \phi_1) + S \Delta p \omega_2 &= 0.
 \end{aligned}
 \tag{8.73}$$

As shown in Fig. 8.16, subscript 1 denotes the upper level and subscript 3 denotes the lower



**Figure 8.16:** Schematic used to explain the two-level model represented by Eqs. (8.73).

level. The vertical velocity is defined in between, at level 2. Here  $\Delta p \equiv p_3 - p_1$  is the pressure thickness between the two layers, and  $S \equiv -\frac{\alpha}{\theta} \frac{\partial \theta}{\partial p}$  is the static stability of the basic state. Let

$$\mathbf{V}_d \equiv \mathbf{V}_3 - \mathbf{V}_1, \quad (8.74)$$

$$\phi_d \equiv \phi_3 - \phi_1, \quad (8.75)$$

be the vertical shear (actually, difference) of the horizontal wind between the two layers, and the thickness between the two layers, respectively. Then (8.73) implies that

$$\frac{\partial \mathbf{V}_d}{\partial t} + f \mathbf{k} \times \mathbf{V}_d + \nabla \phi_d = 0, \quad (8.76)$$

and

$$\frac{\partial \phi_d}{\partial t} + \frac{S \Delta p^2}{2} \nabla \cdot \mathbf{V}_d = 0, \quad (8.77)$$

which are identical to the shallow water equations, and we can identify

$$c_i \equiv \Delta p \sqrt{\frac{S}{2}} \quad (8.78)$$

as the phase-speed of the internal gravity waves.

We return now to our discussion of (8.72). Assume solutions of the form  $e^{i(kx + \omega t)}$ , with  $k \geq 0$ , so that  $\omega > 0$  implies westward propagation. We can derive a single equation

that governs the meridional structure of  $v$ :

$$\frac{d^2 v}{dy^2} + \left( \omega^2 - k^2 + \frac{k}{\omega} - y^2 \right) v = 0. \quad (8.79)$$

Here

$$v \rightarrow v(y), \quad (8.80)$$

where the “original  $v$ ” is  $\hat{v} e^{i(kx + \omega t)}$ . As boundary conditions, we use

$$v \rightarrow 0 \text{ as } y \rightarrow \pm\infty. \quad (8.81)$$

Nontrivial solutions satisfying these boundary conditions exist when

$$\omega^2 - k^2 + \frac{k}{\omega} = 2n + 1 \text{ for } n = 0, 1, 2, \dots \quad (8.82)$$

Note that the expression on the right-hand side of (8.82) generates all positive odd integers, so that Eq. (8.82) is equivalent to the statement that  $\omega^2 - k^2 + \frac{k}{\omega}$  is an odd positive integer. The solutions of (8.79) are given by

$$v(y) = C e^{-\frac{1}{2}y^2} H_n(y), \quad (8.83)$$

where  $H_n(y)$  is the  $n$ th Hermite polynomial, which is given by

$$H_n(y) \equiv (-1)^n e^{y^2} \frac{d^n}{dy^n} (e^{-y^2}) \quad (8.84)$$

(see the Appendix on Hermite polynomials). Because of the factor  $e^{-\frac{1}{2}y^2}$  in (8.83), these modes decay rapidly as we move away from the Equator. The e-folding distance is about 1000 km.

The dispersion equation, (8.82), is cubic in  $\omega$ , and so there are three  $\omega$ ’s for each  $(k, n)$ . Two of these correspond to inertia-gravity waves. For large  $k$ , they can be approximated by

$$\omega_{1,2} \cong \pm \sqrt{k^2 + 2n + 1}. \quad (8.85)$$

These expressions can be compared with (8.37). The third root corresponds to a Rossby wave. For large  $k$ , it can be approximated by

$$\omega_3 \equiv \frac{k}{\sqrt{k^2 + 2n + 1}} . \quad (8.86)$$

For the special case  $n = 0$ , the dispersion equation (8.82) can be factored:

$$(\omega - k)(\omega^2 + k\omega - 1) = 0 . \quad (8.87)$$

Matsuno shows that for  $n = 0$  the three roots can be interpreted as follows:

$$\textbf{Eastward gravity wave: } \omega_1 = -\frac{k}{2} - \sqrt{\left(\frac{k}{2}\right)^2 + 1} , \quad (8.88)$$

$$\textbf{Westward gravity wave: } \omega_2 = \begin{cases} \sqrt{\left(\frac{k}{2}\right)^2 + 1} - \frac{k}{2} & \text{for } k \leq \frac{1}{\sqrt{2}} \\ k & \text{for } k \geq \frac{1}{\sqrt{2}} \end{cases} , \quad (8.89)$$

$$\textbf{Rossby wave: } \omega_3 = \begin{cases} k & \text{for } k \leq \frac{1}{\sqrt{2}} \\ \sqrt{\left(\frac{k}{2}\right)^2 + 1} - \frac{k}{2} & \text{for } k \geq \frac{1}{\sqrt{2}} . \end{cases} \quad (8.90)$$

Notice that for  $n = 0$  the westward gravity wave and the Rossby wave are not really distinct. They coincide for  $k = 1/\sqrt{2}$ . Matsuno pointed out that the root  $\omega = k$  has to be thrown out in (8.89) and (8.90). The reason is that order to derive (8.79) it is necessary to assume that

$$\omega = \frac{\omega y v + k \frac{dv}{dy}}{i(\omega - k)(\omega + k)} . \quad (8.91)$$

In view of (8.91),  $\omega = -k$  is not permitted unless the numerator is identically zero for all  $y$ . Matsuno concluded, therefore, that for  $n = 0$  we have only two waves: an eastward moving gravity wave, and a “mixed Rossby-gravity wave,” which is also known as the “Yanai wave.” The Yanai wave behaves like a gravity wave for  $k < 1/\sqrt{2}$ , and like a Rossby wave for  $k > 1/\sqrt{2}$ . The dispersion relation for the Yanai wave is



$$\omega = \sqrt{\left(\frac{k}{2}\right)^2 + 1} - \frac{k}{2}. \quad (8.92)$$

Because  $H_0(y) = 1$ , (8.83) reduces to

$$v(y) = Ce^{-\frac{1}{2}y^2} \quad (8.93)$$

for the Yanai wave. This shows that in Yanai waves the meridional velocity has the same sign on both sides of the Equator and is a maximum on the Equator.

Another special case is the Kelvin wave. To find this mode, begin by putting  $v \equiv 0$  everywhere in (8.72). Then (8.72) reduces to

$$\begin{aligned} i\omega u + ik\phi &= 0, \\ yu + \frac{\partial \phi}{\partial y} &= 0, \\ i\omega \phi + iku &= 0. \end{aligned} \quad (8.94)$$

Nontrivial solutions exist only for

$$(\omega - k)(\omega + k) = 0, \quad (8.95)$$

and are given by

$$\begin{aligned} u = \phi &= Ce^{-\frac{1}{2}y^2}, \quad \omega = -k \\ -u = \phi &= Ce^{\frac{1}{2}y^2}, \quad \omega = k. \end{aligned} \quad (8.96)$$

The second solution does not satisfy our boundary condition as  $y \rightarrow \pm\infty$ . The first solution is the Kelvin wave. The Kelvin wave can be interpreted as corresponding to  $n = -1$ , in the sense that for  $n = -1$  (8.82) has  $\omega = -k$  as a root. We can accept  $\omega = -k$ , because we have not divided by  $\omega + k$  in the course of deriving (8.96).

The various wave-solutions of Matsuno's model are summarized in Fig. 8.17, which shows the roots of the dispersion equation. Recall that positive values of the frequency correspond to westward propagating waves, and negative values (lower part of the figure) to eastward propagating waves. The thick solid curves arcing upward from the origin represent Rossby waves, with positive values of  $n$ . The dashed curves in the upper part of the diagram correspond to westward propagating inertia-gravity waves, and the thin solid curves in the lower part of the diagram correspond to eastward propagating inertia gravity waves.

The westward propagating wave represented by the curve that is partly solid and partly dashed is the mixed Rossby-gravity wave, or Yanai wave. The dashed portion of this

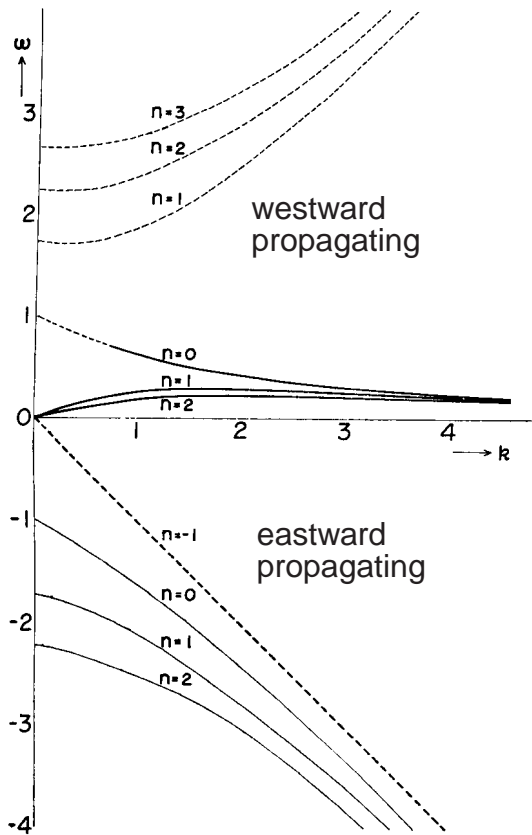


Figure 8.17: Frequencies as functions of wave number. Positive frequencies correspond to westward propagation. Thin solid line: eastward propagating inertia-gravity waves. Thin dashed line: westward propagating inertia-gravity waves. Thick solid line: Rossby (quasi-geostrophic) waves. Thick dashed line: The Kelvin wave. The westward moving wave with  $n=0$  is the mixed Rossby-gravity or Yanai wave. It is denoted by a dashed line for  $k < 1/\sqrt{2}$ , and by a solid line for  $k > 1/\sqrt{2}$ . From Matsuno (1966)

curve, plotted for  $k < 1/\sqrt{2}$ , represents those wave numbers for which the Yanai wave behaves like a westward propagating gravity wave. The solid portion of the curve, for  $k > 1/\sqrt{2}$ , represents those wave numbers for which the Yanai wave behaves like a Rossby wave.

The thick dashed line proceeding downwards towards the right from the origin represents the Kelvin wave.

For  $n = 0$ , the eastward moving inertia-gravity wave and westward moving Yanai wave have the structures shown in the upper and middle panels of Fig. 8.18. For a pure gravity wave we expect the winds to be perpendicular to the isobars. When rotation is dominant, the winds are parallel to the isobars. The waves shown look like pure gravity waves near the Equator. For  $n = 0$  and  $k = 1$ , the Yanai wave takes on the characteristics of a Rossby wave, as shown in the lower panel.

Solutions for  $n = 1$  are shown on the left side of Fig. 8.19. The corresponding results for  $n = 2$  are shown on the right side of the figure. Recall that the subscript  $n$  denotes the solution whose meridional structure is described by the  $n$ th Hermite polynomial. As can be seen in the figure, higher values of  $n$  correspond to more nodes in the meridional direction.

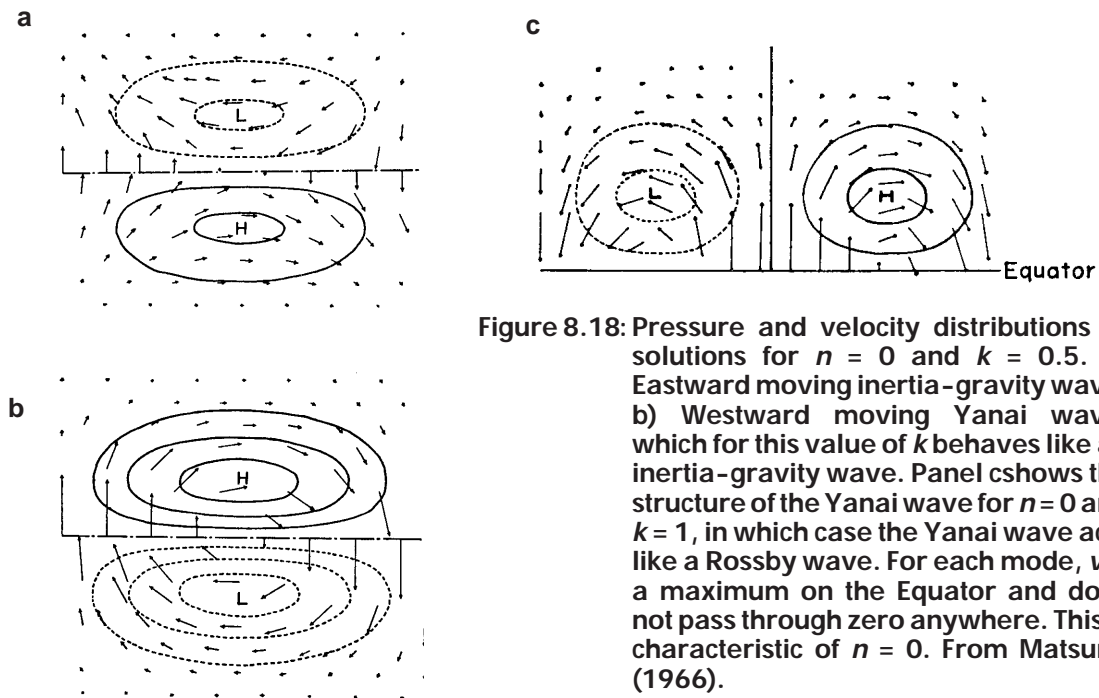


Figure 8.18: Pressure and velocity distributions of solutions for  $n = 0$  and  $k = 0.5$ . a) Eastward moving inertia-gravity wave. b) Westward moving Yanai wave, which for this value of  $k$  behaves like an inertia-gravity wave. Panel c shows the structure of the Yanai wave for  $n = 0$  and  $k = 1$ , in which case the Yanai wave acts like a Rossby wave. For each mode,  $v$  is a maximum on the Equator and does not pass through zero anywhere. This is characteristic of  $n = 0$ . From Matsuno (1966).

The structure of the Kelvin wave is shown in Fig. 8.20. Note that the velocity vectors are purely zonal, and that the tendency of the zonal wind is in phase with the pressure, as in a gravity wave.

There have been many observational studies of tropical waves. Maruyama and Yanai (1966) observed the mixed-Rossby-gravity wave shortly after Matsuno had predicted its existence<sup>2</sup>, and Wallace and Kousky (1968) found the Kelvin wave shortly thereafter. Wheeler and Kiladis (1999) examined the space-time variability of the tropical outgoing long wave radiation. The data have been separated into modes that are symmetric across the Equator (right panel), such as the Kelvin wave, and modes that are anti-symmetric across the Equator (left panel), such as the mixed-Rossby-gravity wave. Through the use of additional filtering procedures motivated by Matsuno's results, Wheeler and Kiladis were able to show the longitudinal propagation of various types of equatorially trapped disturbances (Fig. 8.22 and Fig. 8.24).

## 8.6 The response of the tropical atmosphere to stationary heat sources and sinks

Fig. 8.23 shows the stationary circulation driven by a mass source and sink on the equator. Think of this figure in terms of the low-level flow. The mass sink can be interpreted as a region of rising motion, where the air is converging at low levels, as in the western equatorial Pacific. The mass source can be interpreted as a region of sinking motion, where the air is diverging at low levels, as in the eastern equatorial Pacific. (Unfortunately the mass sink is plotted on the east side and the mass source is plotted on the west side, but this does not really matter because the solution is periodic in the zonal direction anyway.) The model predicts strong westerlies converging (from the west, of course) at low levels into the region of

<sup>2</sup>. Amazingly, Matsuno and Yanai were office mates at about this time.

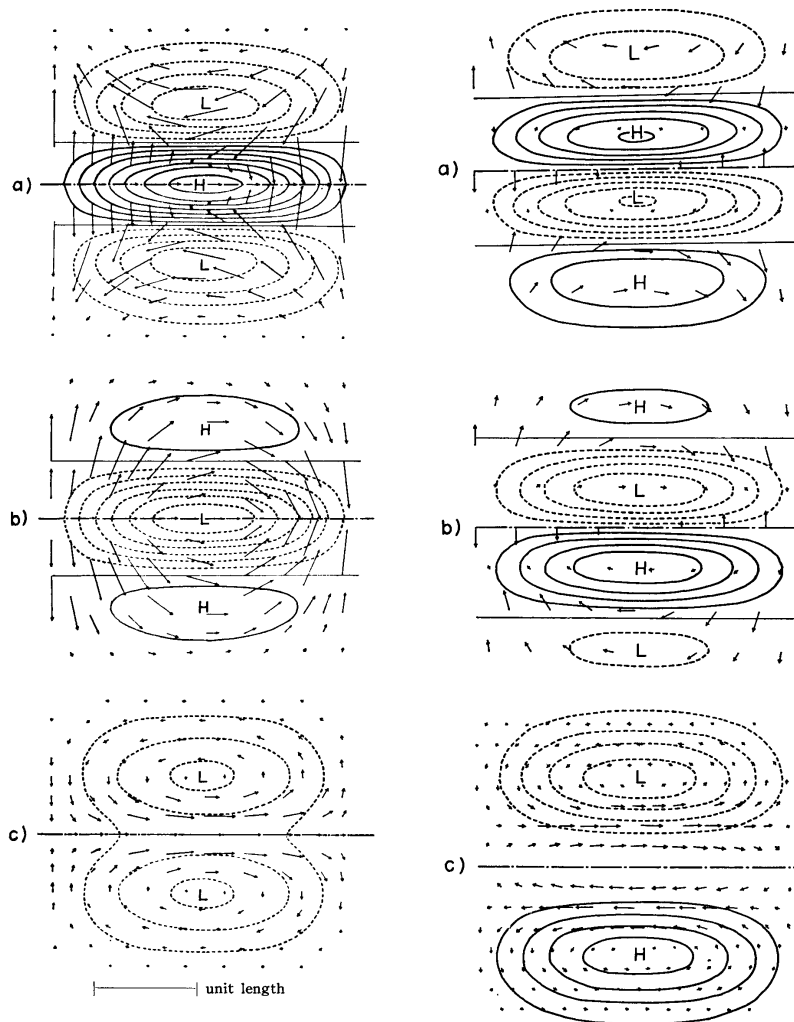


**Figure 8.19:** Left side: Pressure and velocity distributions of solutions for  $n = 1$ . a) Eastward propagating inertia-gravity wave. For each mode,  $u = 0$  on the Equator, as we expect for  $n = 1$ . b) Westward propagating inertia-gravity wave. c) Rossby wave. Right side: Corresponding results for  $n = 2$ . For each mode  $u$  is symmetrical across the Equator, as we expect for  $n = 2$ . From Matsuno (1966).

rising motion, and low-level easterlies converging on the east side of the region of low-level convergence. The easterlies can be interpreted as the trades, and as the lower branch of the Walker circulation. The westerlies can be interpreted as a “monsoon-like” westerly inflow to a region of heating. Further discussion will be given later.

Webster (1972) and Gill (1980) developed simple analytic models of the response of a resting tropical atmosphere to heat sources and sinks. Since much of the convective heating in the tropics is confined over three relatively small land regions (Africa, South America, and the Indonesian region), Gill examined the atmospheric response to a relatively small-scale heating source that is centered on the equator. If the atmosphere is abruptly heated at some

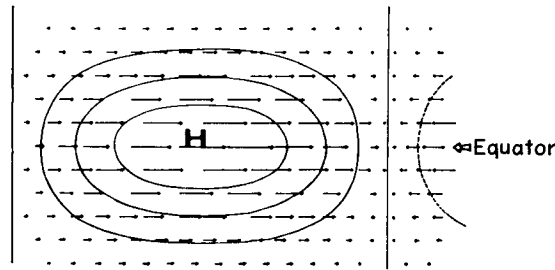


Figure 8.20: Pressure and velocity distributions for  $n = -1$  and  $k = 0.5$ . This is the Kelvin wave. From Matsuno (1966).

initial time, Kelvin waves propagate rapidly eastward and generate easterly trade winds to the east of the heating. Thus the easterly trade winds in the Pacific could result from Kelvin waves produced by convective heating over Indonesia. Similarly, Rossby waves propagate westward and generate westerlies to the west of the heating. Because the fastest Rossby wave travels at only one-third the speed of the Kelvin wave, the effects of the Rossby waves would be expected to reach only one-third as far those as those of the Kelvin wave. Gill interpreted the westerlies over the Indian ocean as a response to Rossby waves generated by convective heating over Indonesia.

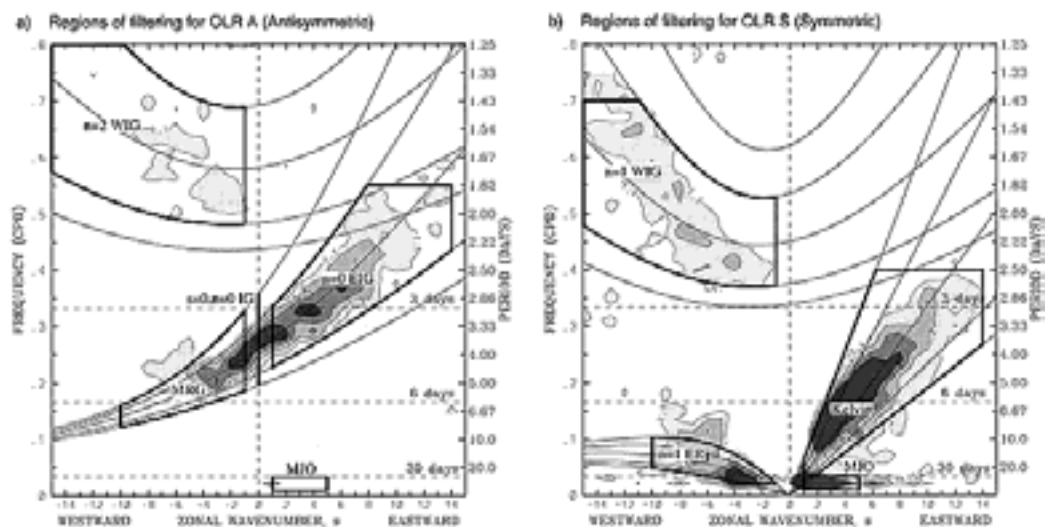


Figure 8.21: The variability of the OLR as a function of frequency and zonal wave number for modes that are symmetric across the Equator (right panel) and anti-symmetric (left panel). Eastward propagation is associated with positive wave numbers, and vice versa. From Wheeler and Kiladis (1999).

Gill (1980) studied what amounts to a steady-state version of Matsuno's model, and introduced forcing in the form of mass sources and sinks, along with very simple damping. Corresponding to (8.72), we have

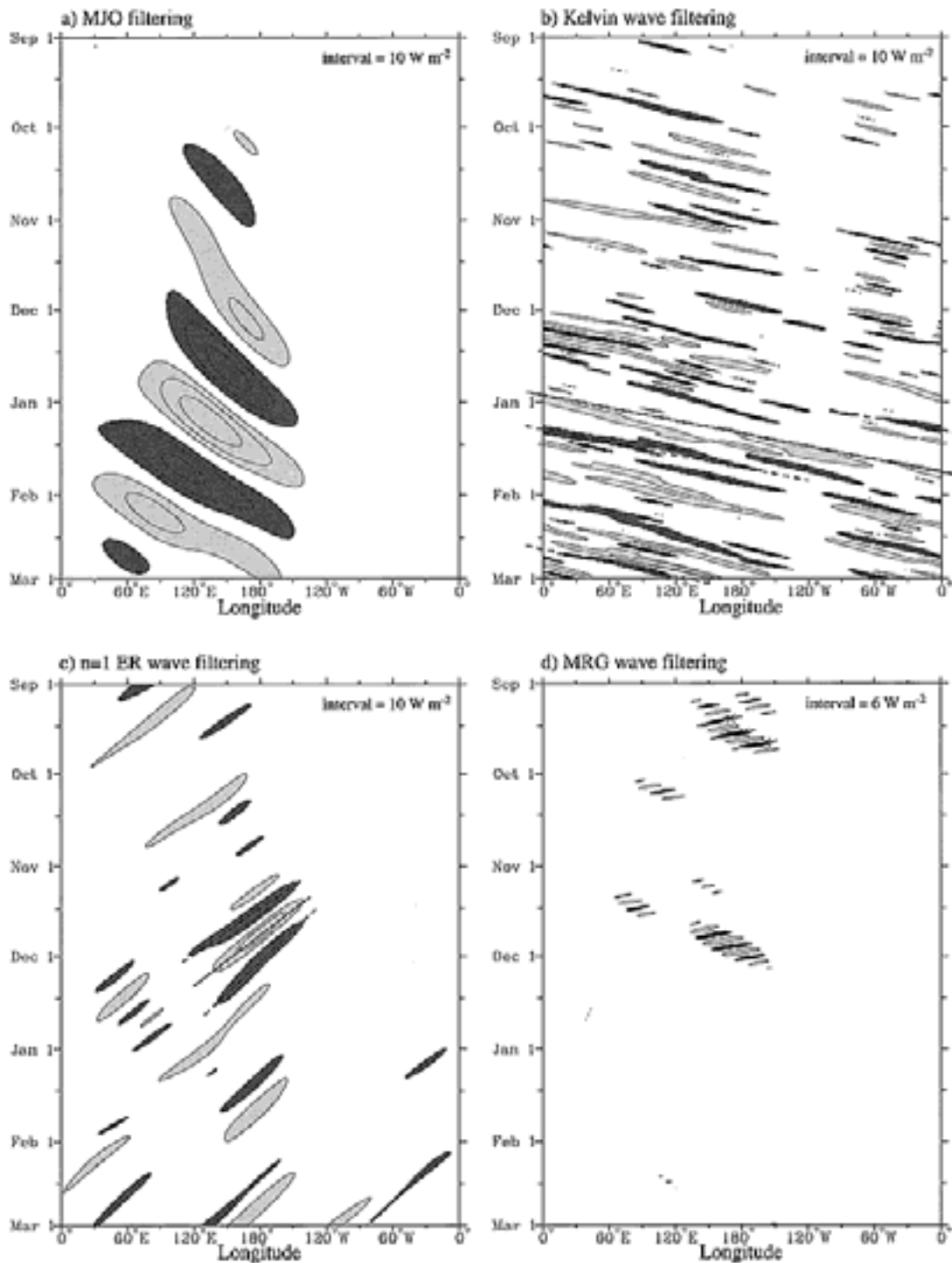


Figure 8.22: Longitudinal propagation of the Madden-Julian Oscillation (MJO; discussed later), Kelvin waves, equatorial Rossby (ER) waves, and mixed-Rossby-gravity (MRG) waves, as seen in the OLR. The zero contour has been omitted. From Wheeler and Kiladis (1999).

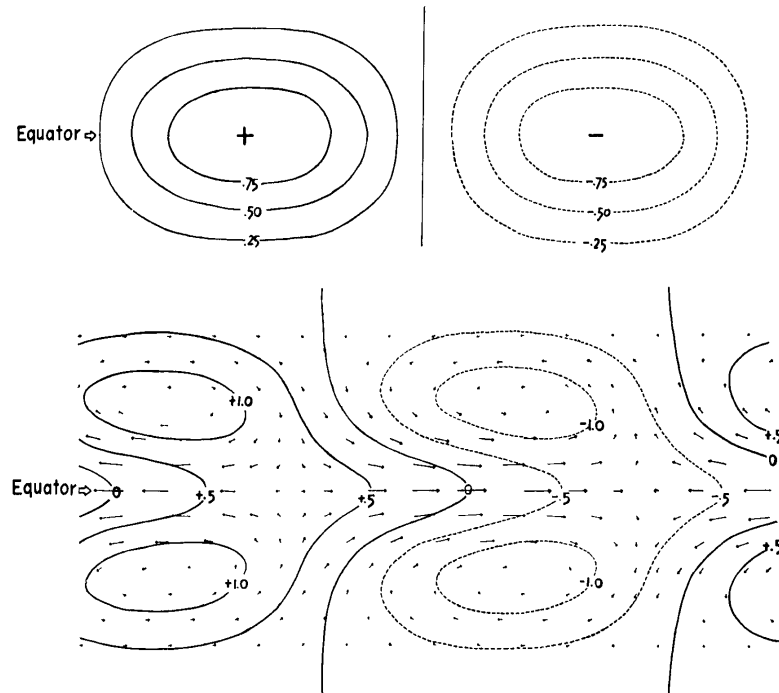


Figure 8.23: Stationary circulation pattern (lower panel) forced by the mass source and sink shown in the upper panel. From Matsuno (1966).

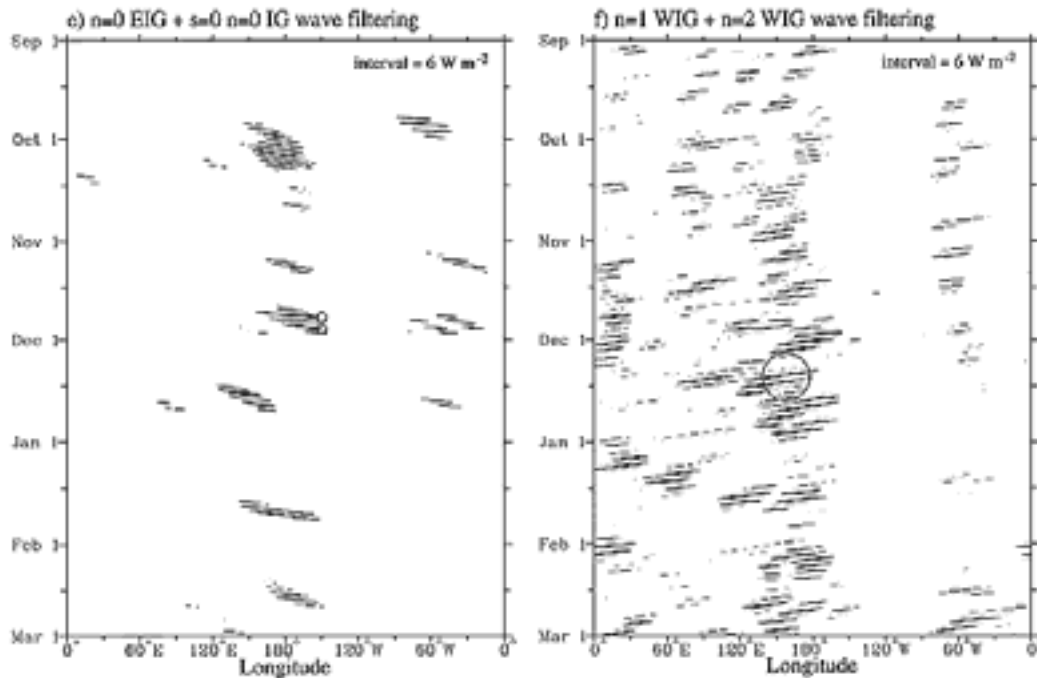


Figure 8.24: Longitudinal propagation of eastward- and westward-propagating inertia gravity waves, as seen in the OLR. The zero contour has been omitted. From Wheeler and Kiladis (1999).



$$\begin{aligned}
\varepsilon u - yv + \frac{\partial \phi}{\partial x} &= 0, \\
\varepsilon v + yu + \frac{\partial \phi}{\partial y} &= 0, \\
\varepsilon \phi + \frac{\partial u}{\partial x} + \frac{\partial v}{\partial y} &= -Q;
\end{aligned} \tag{8.97}$$

and, as a purely diagnostic relation,

$$w = \varepsilon \phi + Q. \tag{8.98}$$

The winds  $u$  and  $v$  represent the lower-tropospheric variables. Here  $\varepsilon^{-1}$  is a dissipation time scale, and  $Q$  is a “heating rate” that must be specified. The variables  $\phi$ ,  $w$ , and  $Q$  are defined in the middle troposphere. Gill included dissipation in the form of Rayleigh friction and Newtonian cooling, and for simplicity assumed that the time scales, given by  $\varepsilon^{-1}$ , are equal. Rayleigh friction is a simple parameterization of friction in which the velocity is divided by a frictional time scale.

Gill focused primarily on cases for which the heating is symmetric or anti-symmetric about the equator. The solution for symmetric heating resembles a Walker circulation, with lower-tropospheric inflow into the heating region and upper-tropospheric outflow. The Walker Circulation is discussed in detail later in this Chapter. The surface easterlies cover a larger area than the surface westerlies because the phase speed of the eastward-propagating Kelvin wave is three times faster than that of the westward-moving Rossby wave. By forming a vorticity equation for the case of no damping, and then substituting from the continuity equation, Gill found that

$$v = yQ. \tag{8.99}$$

This is closely related to what is sometimes called “Sverdrup balance,” in which the “meridional advection of the Coriolis parameter,” i.e. the so-called  $\beta$  term of the vorticity equation, is balanced by the divergence term, which is represented on the right-hand side of (8.99). For a incompressible atmosphere with a rigid lid at  $z = D$  and a constant lapse rate, the gravest mode (the mode with the largest vertical scale) has horizontal velocity components that vary as  $\cos(\pi z/D)$ , i.e., they pass through zero in the middle troposphere. This is similar to the observed vertical structure of the Hadley-Walker circulation.

For  $Q > 0$ , (8.99) implies poleward motion in the lower layer and equatorward motion in the upper layer. This suggests that in regions of heating, e.g. the western Pacific, the Walker circulation produces a north-south circulation that opposes the Hadley circulation. Geisler (1981) found the same result. For  $Q < 0$ , the low-level motion is Equatorward; this is what we see in the subtropical highs, e.g., in the eastern Pacific.

The solution for anti-symmetric heating consists of a mixed Rossby-gravity wave and a Rossby wave. There is no Kelvin-wave response because the Kelvin wave is intrinsically symmetric across the Equator. Long mixed Rossby-gravity waves do not propagate, and so



the response of this wave type is largely confined to the region of heating. Due to the westward propagation of Rossby waves, no response is generated to the east of the forcing region. To the west, the region of westerly flow into the heating region is limited because the Rossby modes travel slowly, and so are dissipated before they can propagate far to the west.

Gill interpreted the symmetric case as a simulation of the Walker circulation, and the asymmetric case as a simulation of the Hadley circulation.

For heating centered on the Equator, as in Fig. 8.25, Gill found strong westerlies on the west side, and strong easterlies on the east side, combining to give strong zonal convergence on the heating. The westerlies can be interpreted as the time-averaged response to westward-propagating Rossby waves excited by the heating, and the easterlies can be interpreted as the time-averaged response to eastward-propagating Kelvin waves excited by the heating. This implies a Walker circulation, as indicated in Fig. 8.25, and a surface pressure field with a minimum pressure slightly to the west of the heating.

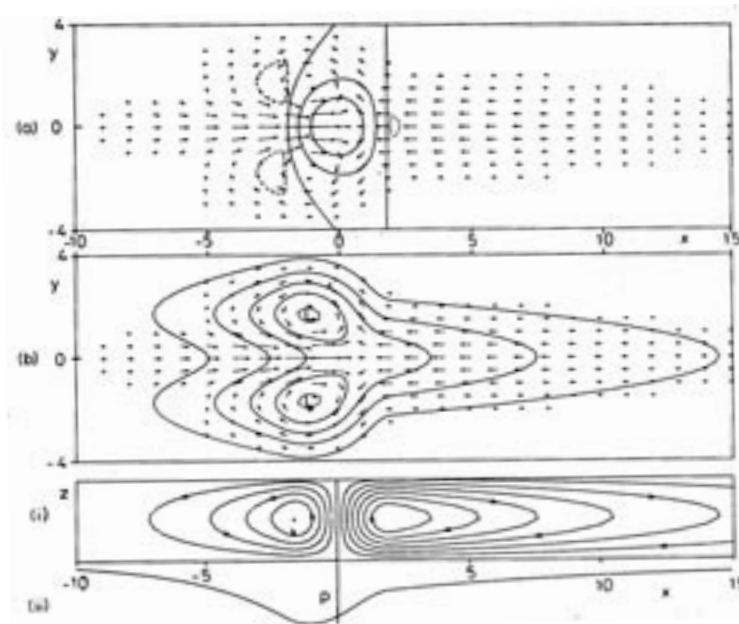


**Figure 8.25: Solution of Gill's model for the case of heating symmetric about the Equator.** The upper panel shows the heating field and the low-level wind field. The center panel shows the perturbation pressure field, which features low pressure along the Equator generally, with twin cyclones slightly off the Equator. The bottom panel shows the implied vertical motion and the zonal variation of the pressure along the Equator. From Gill (1980).

When the heating is antisymmetric across the Equator, as in Fig. 8.26, the model produces something like a Hadley circulation, with a low-level cyclonic circulation on the side with positive heating, and a low-level anticyclone on the other side.

When the symmetric and antisymmetric heatings are combined, as in Fig. 8.27, the model produces a circulation that looks remarkably similar to that of the Asian summer monsoon, as discussed in the next subsection.

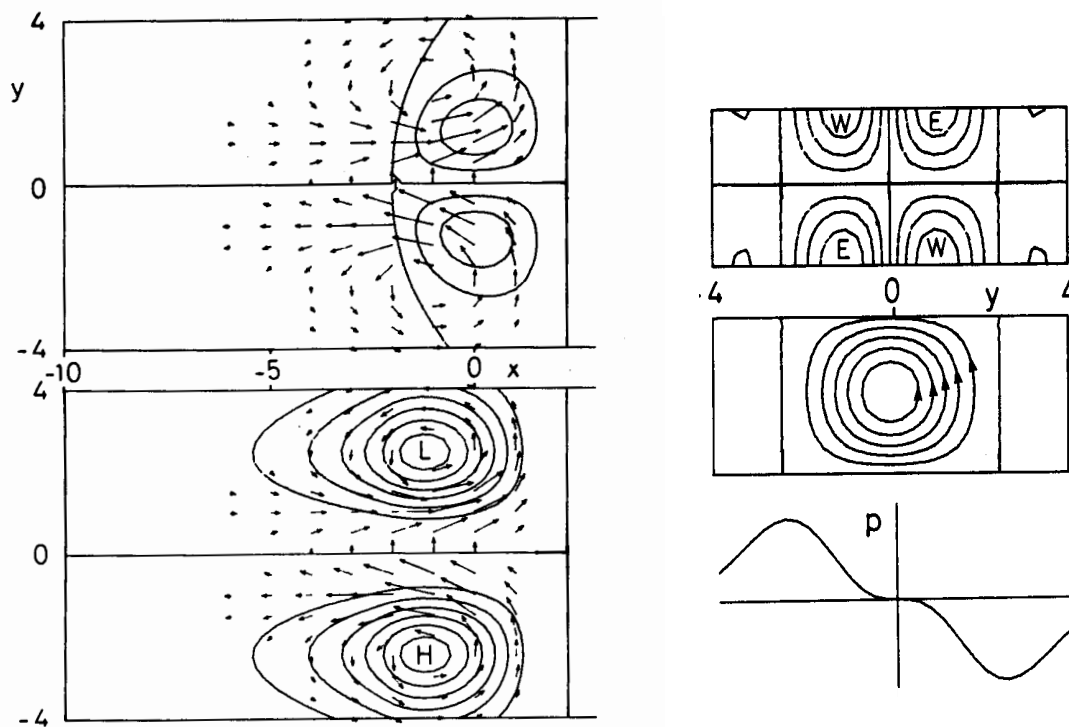
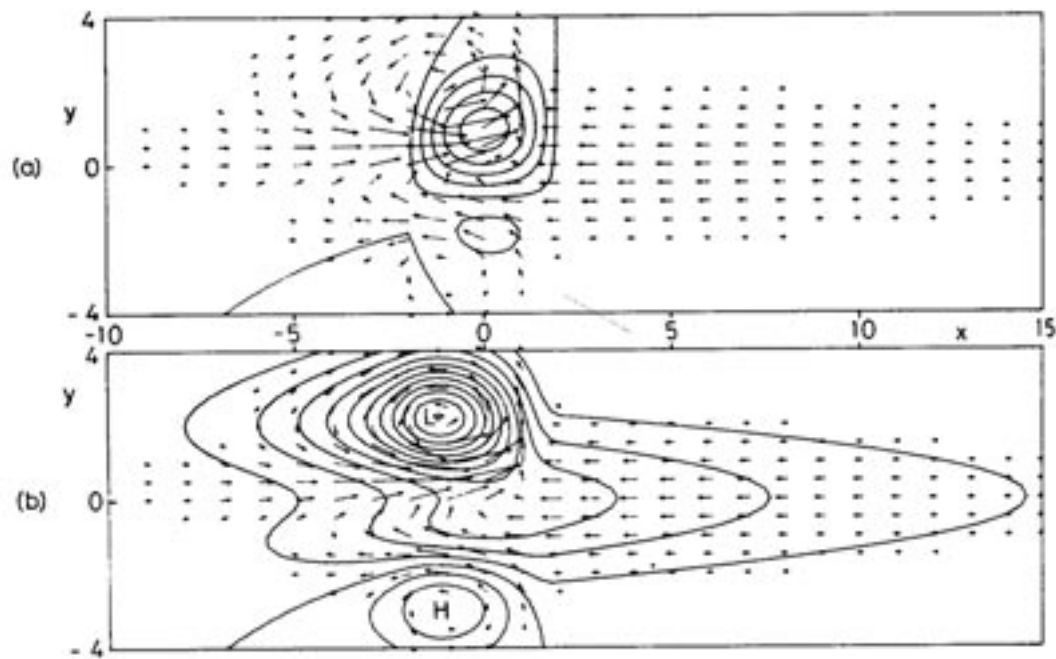


Figure 8.26: The response to antisymmetric heating. On the left side, the top panel shows contours of the mid-level vertical velocity superimposed on the horizontal wind vectors for the lower layer. The lower panel shows contours of the perturbation surface pressure, again with the lower-layer horizontal wind field superimposed. The right-hand panels show the zonally integrated solution corresponding to the results in the left-hand panels. The upper panel shows the latitude-height distributions of the zonal velocity and the stream function of the mean meridional circulation, as well as the meridional profile of the surface pressure. From Gill (1980).

Although Gill plausibly demonstrated that heating of limited extent generates tropical waves that produce broad wind and pressure fields resembling the observations, his results must be viewed with caution due to several limitations. First, results were generated for a specified rather than predicted heating of the tropical troposphere, and so ocean-atmosphere interactions and feedbacks involving moist convection were excluded. Second, the model includes neither a moisture budget nor cloud radiative effects. Last and most important, the model was linearized about a resting atmosphere. Although linearization is useful, Gill's results must be interpreted as the response of the tropical atmosphere to a perturbation of a basic state, not as a prediction of the basic-state climate. Gill demonstrated the sensitivity of the tropical troposphere to the spatial distribution of heating, but his study does not really address the basic-state climate.

### 8.7 Monsoons

Monsoons occur in many parts of the world. They can be viewed as thermally forced



**Figure 8.27: The response of Gill's model to a combination of symmetric and antisymmetric heating. From Gill (1980).**

stationary planetary waves associated with land-sea contrast. The most spectacular monsoon on Earth is the one associated with Asia, our largest continent.

The Asian monsoon can be defined in a number of ways. By definition, a monsoon is a dramatic seasonal reversal of the low-level prevailing winds (Lighthill and Pearce, 1981). In the dramatic case of the Asian monsoon, the winds near the surface reverse from the northeast in winter to the southwest in summer, as seen in Fig. 8.28. The  $15 \text{ m s}^{-1}$  low-level southwest wind that crosses the Equator and flows from the coast of east Africa to the shores of India is known as the Somali jet. It is one of the strongest low-level jets in the world. There are other seasonal changes of wind in the world, but none have the geographical scope or the socioeconomic impact of the Asian monsoon.

The basic trigger for the monsoon is a contrast between the temperature of the Asian continent and that of the surrounding ocean. The thermal anomaly in the middle troposphere is enhanced by the spectacular topography of the Tibetan Plateau (Fig. 8.29), which extends upward to about the 500 mb level. Much of the “surface” heating associated with the summer monsoon actually occurs in the middle troposphere, because it is located on the Tibetan Plateau. The Tibetan Plateau towers above the surrounding land surface, with average elevations over the central Plateau of over 3000 m. The observed JJA mean 500 mb temperature for the monsoon region is shown in Fig. 8.30. An island of warm air is centered over the Tibetan plateau.

After the non-permanent snow on the Plateau has melted in late spring and early summer, the surface and the air above it are heated to a temperature higher than that of the surrounding atmosphere. Rising motion balances this heating, and this forces convergence in the lower and middle troposphere, and compensating divergence aloft. As the seasonal heating builds, a trough forms over southern India in late May, and subsequently moves north and

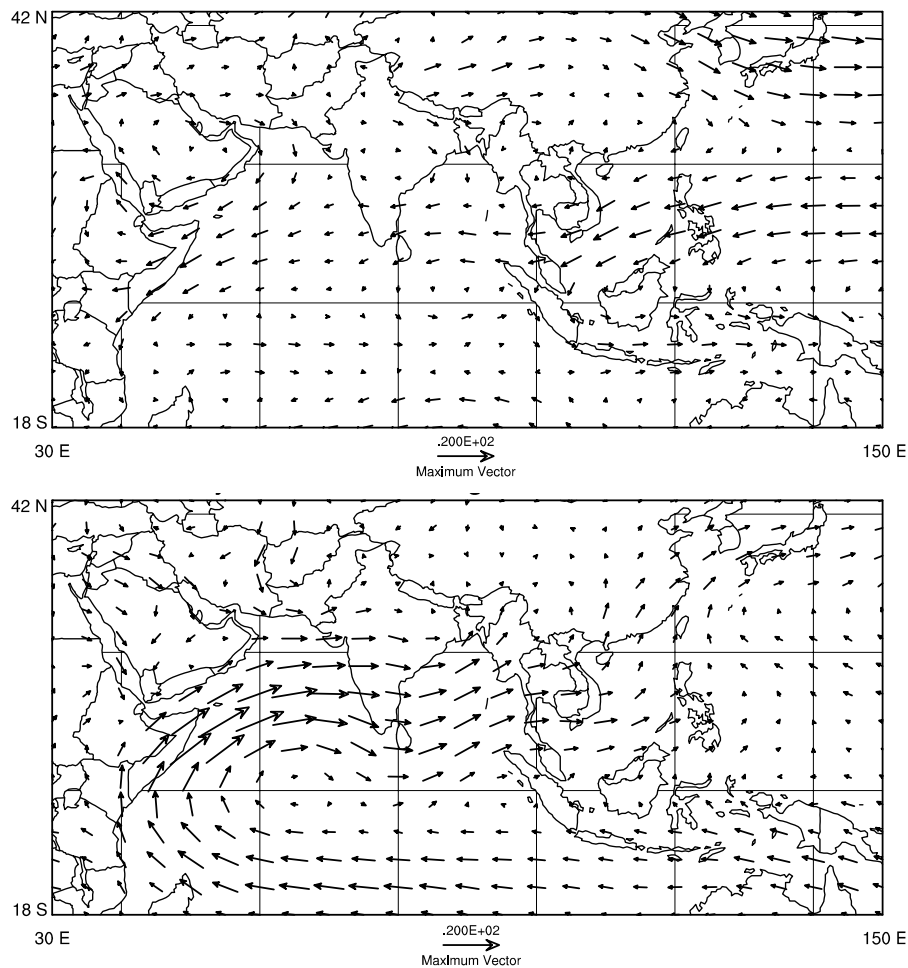


**Figure 8.28:** Observed 850 mb wind vectors for a) January, and b) July.

west. In some cases, the progression of the monsoon trough is expedited by the passage of a tropical or extratropical cyclone to the north (Mooley and Shukla, 1987). Cloudiness and precipitation begin to increase at the southern tip of India in late May. Nearly the entire country has begun to receive monsoon precipitation by the end of June.

The onset of the summer monsoon brings cooler surface temperatures to India and other areas that receive monsoonal precipitation, due to the increase in clouds as well as the increase in soil moisture that accompanies the precipitation. The data shows, as one might expect, that the lowest surface air temperatures in the monsoon region occur at the highest elevations. There is a large area of low (less than 280 K) surface air temperature on the Tibetan Plateau, and a large area of high (greater than 305 K) surface air temperatures on the Arabian Peninsula.

From an agricultural standpoint, the beginning of the precipitation associated with the Asian summer monsoon is probably one of the most anticipated events in the world. The onset of the monsoon is generally defined as the beginning of consistent rainfall of the monsoon season. Fig. 8.31 shows a plot of the dates of onset of the Asian monsoon from

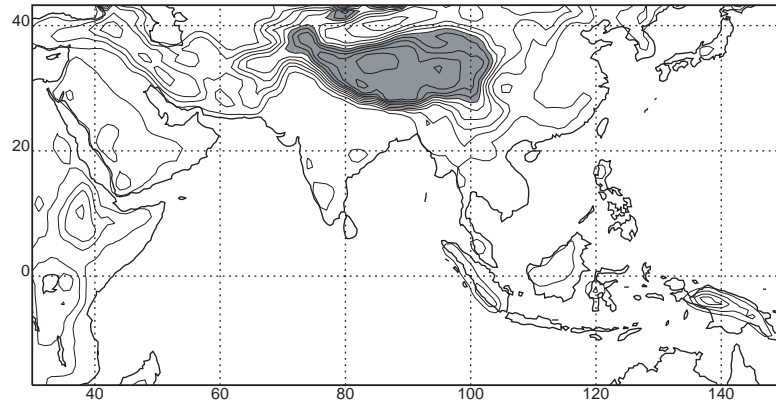


Figure 8.29: Average elevation of the monsoon region. Data was averaged to  $1^\circ \times 1^\circ$ , and then 9-point smoothed. Terrain over 3000 m high is shaded.

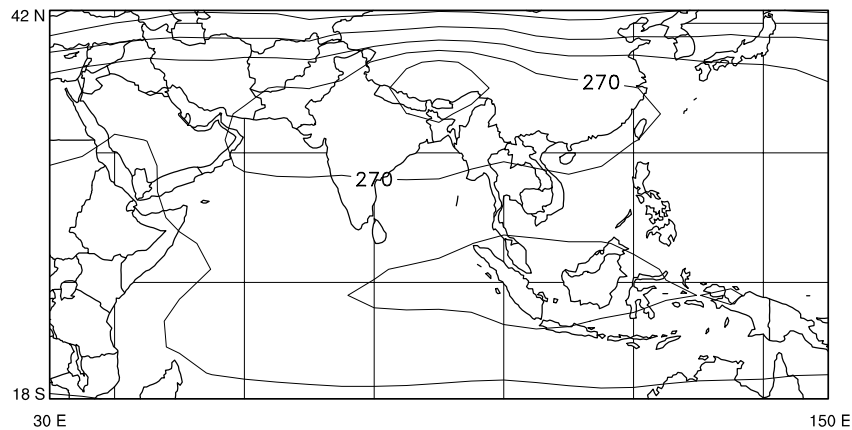


Figure 8.30: Observed JJA climatological 500 mb temperatures. Contour interval is 2 K.

Krishnamurti et al. (1990). The Ganges valley receives copious amounts of rain from monsoon depressions that form in the Bay of Bengal and propagate northward and westward. An example is shown in Fig. 8.32 a. Many areas within the monsoon region also receive significant amounts of precipitation from tropical cyclones. Fig. 8.32 b shows the daily precipitation totals at an average of several stations on the southwest coast of India, and gives a sense as to the observed intraseasonal variability of monsoon precipitation. Much of the precipitation of the Asian monsoon is forced by southwest winds flowing over the western shores of India and Southeast Asia, as well as the foothills of the Tibetan Plateau (Johnson and Houze, 1987).

Fig. 8.33 shows JJA means of the precipitation across the monsoon region, according to the climatological data set of Legates and Wilmott (1990). There are two major precipitation maxima. One is west of the southwest coast of India, and the other is west of southern Myanmar. Both of these areas receive strong onshore flow, showing that the ocean is the source of the moisture. Minima occur near Sri Lanka and the east coast of Vietnam. These areas appear to be in orographic rain shadows. The northern and western parts of the monsoon region are quite dry, receiving less than  $2 \text{ mm day}^{-1}$  of rain. The observed 850 mb wind

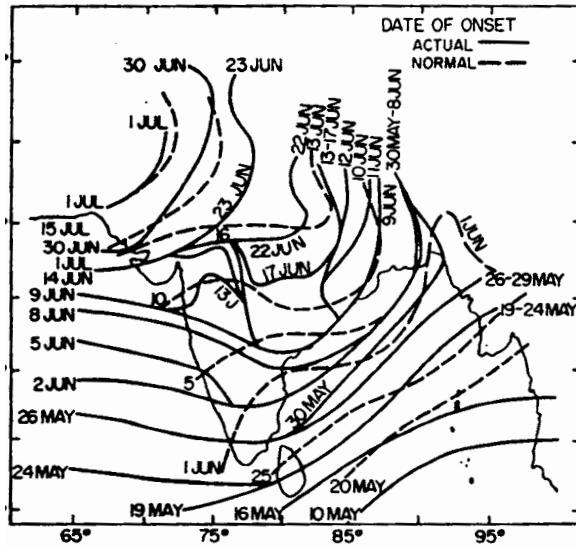


Figure 8.31: Dates of onset of the Asian monsoon near India in 1988 (actual) and mean (normal). From Krishnamurti *et al.* (1990).

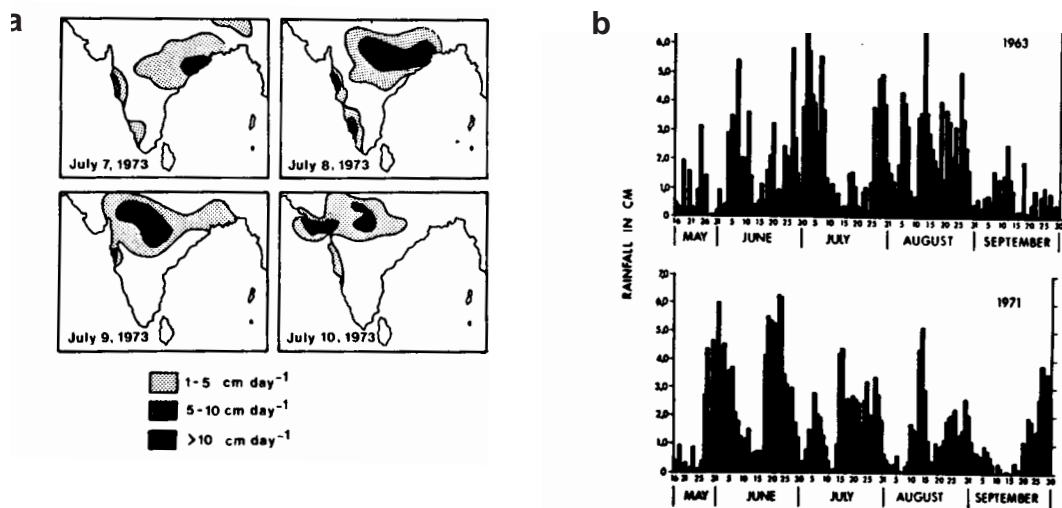
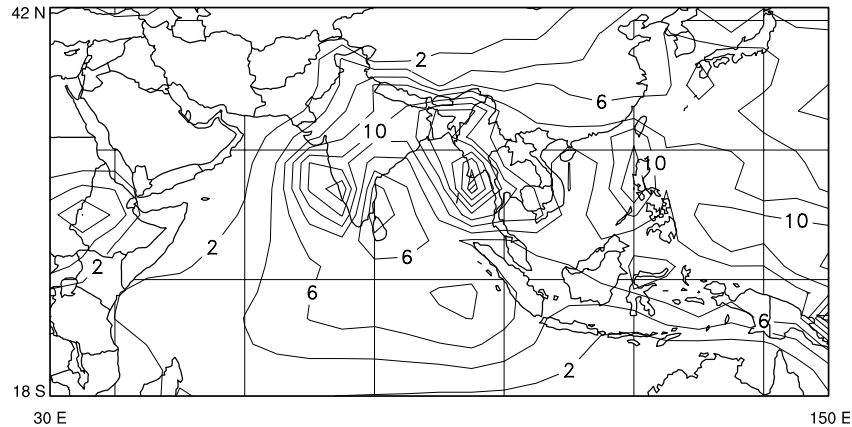


Figure 8.32: a) Observed daily rainfall along the southwest coast of India for the summer monsoon seasons of 1963 and 1971. From Webster (1987). b) Progress of a monsoon depression across India. Many such depressions occur throughout the summer monsoon. From Webster (1981).

analysis shows that these areas do not receive much moisture from the Indian Ocean during JJA. Only a small portion of the monsoon region receives more than  $20 \text{ mm day}^{-1}$  of precipitation.

The precipitation in much of the monsoon region varies on many time scales. The individual disturbances that cause the precipitation associated with the Asian monsoon last only a few days at any single location. However, there are also prominent variations known as “breaks,” which occur at periods of approximately 10-20 days and 40-50 days (Webster,





**Figure 8.33: The observed JJA climatological precipitation (Legates and Willmott, 1990). The contour interval is  $2 \text{ mm day}^{-1}$ .**

1987). The 10-20 day variation is related to the periodic northward propagation of the Intertropical Convergence Zone (ITCZ), which begins near the Equator, and progresses to the foothills of the Tibetan Plateau in roughly 15 days, as seen in Fig. 8.34. The ITCZ usually reforms in the south after it has progressed to the foothills of the Tibetan Plateau, but occasionally it stays near the Plateau for an “extended break” period of 40-50 days. These extended break periods have been linked by some (Webster, 1987) to the 40-50 day oscillation discovered by Madden and Julian (1972), which is discussed in detail later.

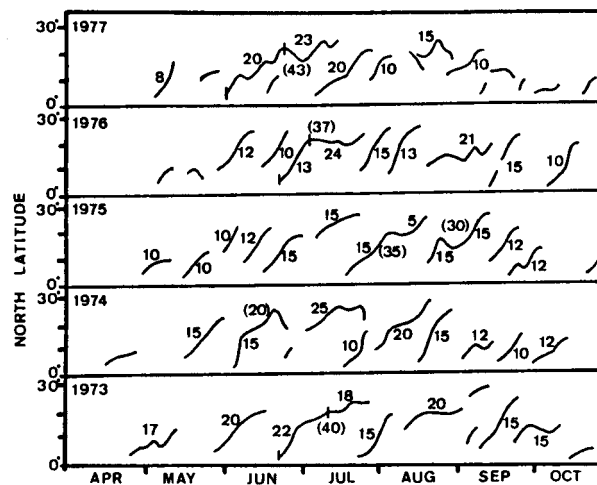


**Figure 8.34: Mean latitudinal position of the monsoon trough in the Indian Ocean for the summers of 1973-1977, as obtained from the maximum cloudiness zone and the 700 mb trough. Numbers refer to longevity of a particular cloudiness zone, with extended break periods indicated by parentheses. From Webster (1987), Webster (1983), and Sikka and Gadgil (1980).**

One of the most prominent signatures of the Asian monsoon is the monsoon trough, which extends from Bangladesh to the Arabian Peninsula. The sea level pressure field is dominated by the monsoon trough, and an area of high pressure over the Tibetan Plateau.

The heating of the middle troposphere by the Tibetan plateau induces convergence in the middle and lower troposphere (Yanai, *et al.*, 1992), largely through the Somali jet. To balance the convergence at the lower levels of the atmosphere, there must be large-scale rising motion, and divergence aloft. The observed JJA mean 500 mb vertical velocity for the monsoon region is shown in Fig. 8.35. The strongest areas of rising motion are over southwestern India and the Bay of Bengal. These areas both receive copious amounts of precipitation in JJA. Two of the strongest areas of sinking motion are over the eastern Mediterranean Sea and northern China. Both areas are quite dry in JJA, receiving less than 2 mm day<sup>-1</sup> of rain. The area mean vertical velocity is upward, at -10 mb day<sup>-1</sup>.

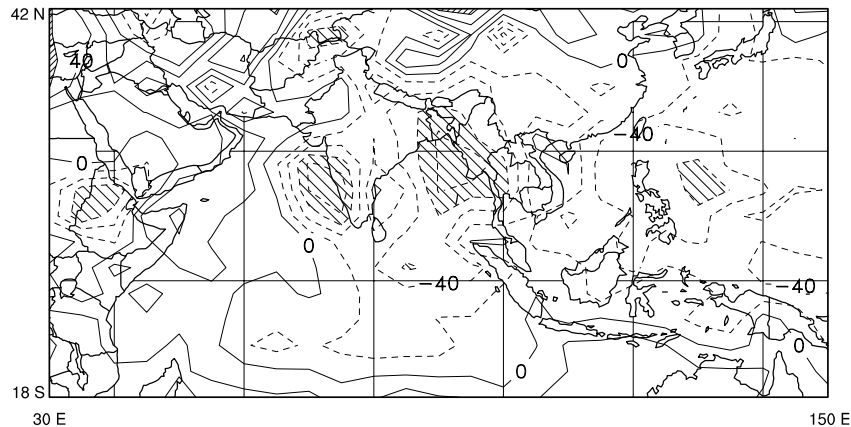


**Figure 8.35:** Observed JJA climatological 500 mb vertical velocity. Contour interval is 20 mb day<sup>-1</sup>. Areas with vertical velocities more negative than -60 mb day<sup>-1</sup> have light shading.

The upper-level divergence is associated with a broad, strong anticyclonic circulation over the Plateau at 200 mb, as shown in Fig. 8.36. The strong, upper-level easterlies (15 - 20

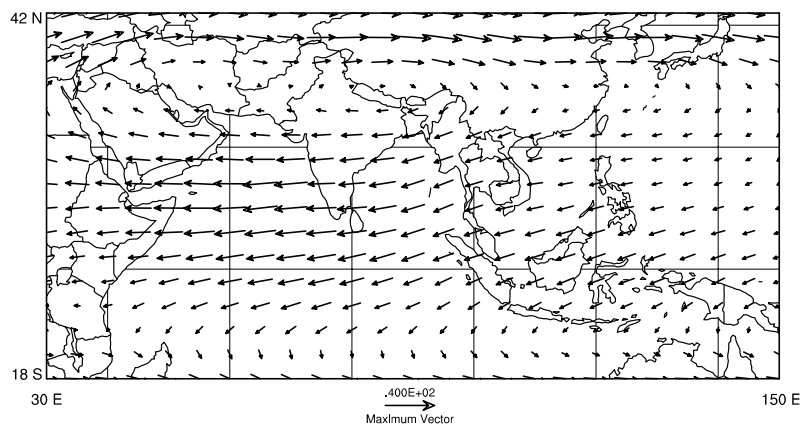


**Figure 8.36:** JJA climatological 200 mb winds. The scale vector is 50 m s<sup>-1</sup>.

m s<sup>-1</sup>) are consistent with the thermal wind relationship, because the lower and middle tropospheric temperatures actually increase towards the north in the Northern Hemisphere (Yanai *et al.*, 1992; Murakami, 1987; Yanai and Li, 1993). There is a slight northerly component to the 200 mb winds at the Equator, especially on the eastern side of the region.



The winds shift abruptly from easterlies to westerlies at the northern and southern fringes of the monsoon region, with westerlies of up to  $30 \text{ m s}^{-1}$  at about  $35^\circ \text{N}$ . Fig. 8.37 shows a latitude-pressure cross-section of the observed zonal wind at  $77.5^\circ \text{E}$ .

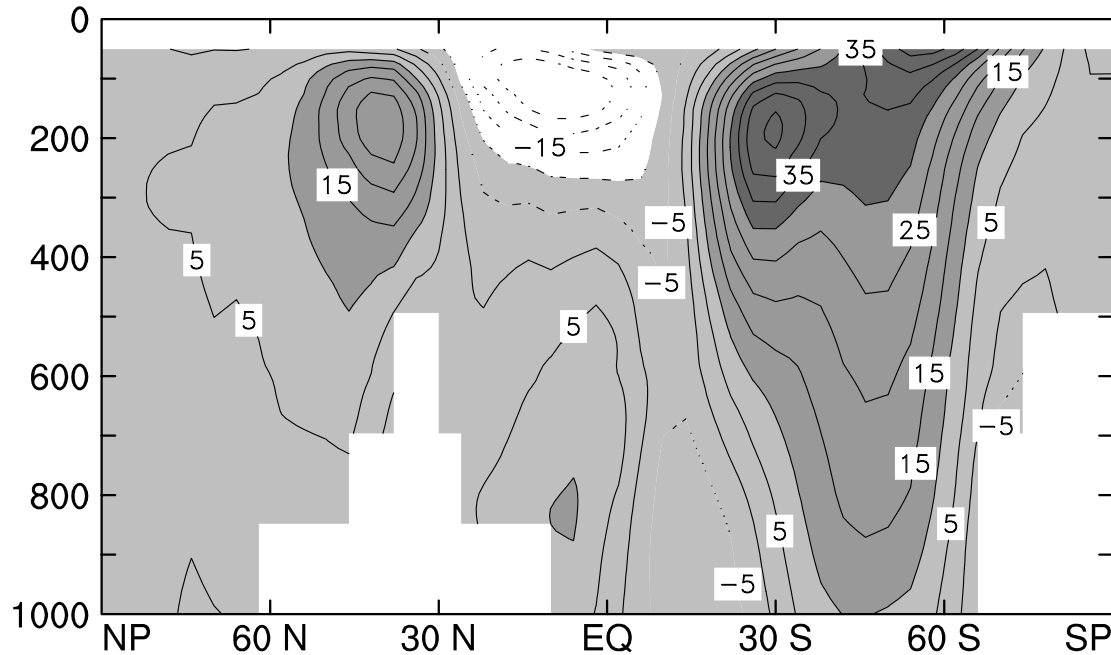
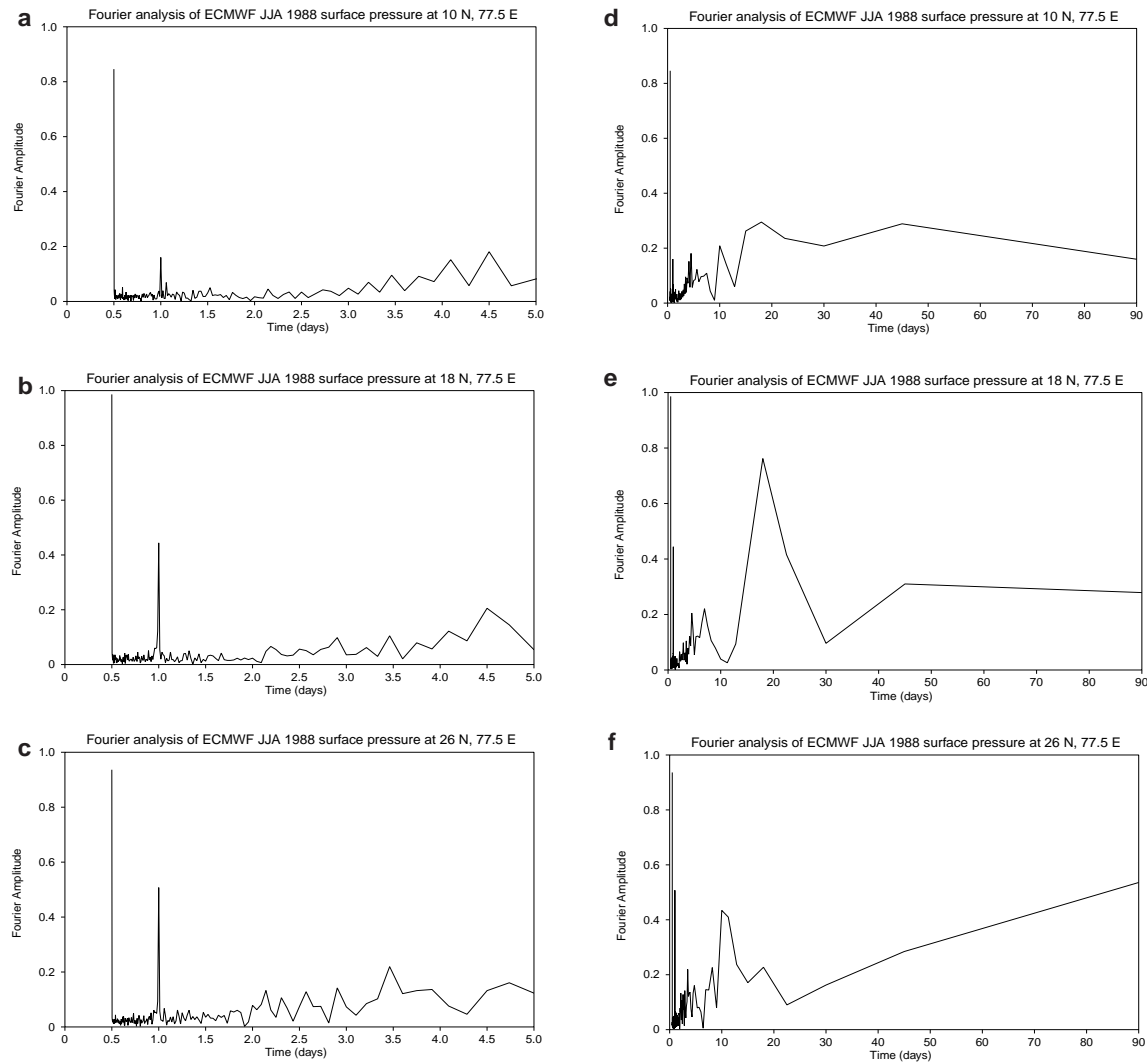


Figure 8.37: Latitude-pressure plot of the JJA climatological zonal winds at  $77.5^\circ \text{E}$ . The contour interval is  $5 \text{ m s}^{-1}$ .

From the above discussion, it is clear that we can interpret the monsoon as a zonally localized Hadley circulation (Webster 1987), with a meridional low-level branch that moves towards a warm, convectively active ascending branch, and an upper-level return flow that feeds a relatively cool descending branch. In fact, in the northern summer the Hadley circulation is more or less contained within the longitudes of the monsoon region. The monsoon is thus a direct circulation, which converts potential energy to kinetic energy.

The left-hand column of Fig. 8.38 shows the hourly record of surface pressure and its Fourier spectrum at  $10^\circ \text{N}$ ,  $77.5^\circ \text{E}$ , near the southern tip of India, at  $26^\circ \text{N}$ ,  $77.5^\circ \text{E}$ , and at  $26^\circ \text{N}$ ,  $77.5^\circ \text{E}$  in northern India. All three locations show a large peak at 12 hours, which corresponds to the semidiurnal tide. There is also a noticeable diurnal tide. The right-hand column of Fig. 8.38 shows similar observations for the same three locations, but for longer periods. Beyond 24 hours, all three locations show oscillations with time scales of a few days, which is the time scale of synoptic weather systems. There is also a spectral peak at 10–20 days, which may be associated with the period of time it takes for the monsoon trough to move from the southern tip of India to the Himalayan foothills and back again (Webster, 1987). The 10–20 day peak for  $26^\circ \text{N}$  is at about 18 days, while the peak at  $10^\circ \text{N}$  is only 13 days. The difference between the two periods may be due to the monsoon trough not making it as far north as  $26^\circ \text{N}$  during some of its north-south oscillations, which would cause the surface pressure dip to be less frequent there. There is also an oscillation with a period of 90 days that might be associated with the onset and departure of the monsoon itself.



**Figure 8.38:** Observed Fourier power spectra of surface pressure. a) at  $10^{\circ}\text{N}$ ,  $77.5^{\circ}\text{E}$ , near the southern tip of India, for oscillations with a period of 0–5 days; b) at  $18^{\circ}\text{N}$ ,  $77.5^{\circ}\text{E}$ , for oscillations with a period of 0–5 days; c) at  $26^{\circ}\text{N}$ ,  $77.5^{\circ}\text{E}$ , for oscillations with a period of 0–5 days; d) at  $10^{\circ}\text{N}$ ,  $77.5^{\circ}\text{E}$ , for oscillations with a period of 0–90 days; e) at  $18^{\circ}\text{N}$ ,  $77.5^{\circ}\text{E}$ , for oscillations with a period of 0–90 days; and f) at  $26^{\circ}\text{N}$ ,  $77.5^{\circ}\text{E}$ , for oscillations with a period of 0–90 days.

Precipitation in the monsoon region has also been observed to vary systematically on time scales of 2–5 days, 10–20 days, and 40–50 days (Webster, 1987). Due to the convective nature of much of the precipitation that takes place in the Asian monsoon, there are also significant variations on time scales of only a few hours. For periods on the order of 10–20 days, the spectral analyses of precipitation are similar to those of surface pressure. This is understandable, because the heaviest precipitation is generally associated with the monsoon trough. There do not appear to be any semidiurnal or diurnal variations in precipitation, although there is a large amount of high-frequency spectral energy, as might be expected with

convective rainfall. There are some indications of spectral peaks of precipitation at 25-35 days. These might be associated with the Madden-Julian oscillation.

There have been many efforts to understand the interannual variability that occurs with the Asian monsoon. The 1987 summer monsoon was remarkably dry over most of India (Krishnamurti *et al.*, 1989) whereas the 1988 summer monsoon was quite wet in the same region (Krishnamurti *et al.*, 1990). Charney and Shukla (1981) argued on the basis of modeling studies that the largest variations in monsoon rainfall and sea level pressure are due to changes in the boundary conditions. They speculated that if these boundary conditions could be specified without error, then seasonal predictions of quantities such as monthly-mean monsoon precipitation would be possible. Dry Asian summer monsoons have been statistically correlated to anomalously warm SSTs in the eastern Pacific (El Niño), and wet monsoons have been correlated to anomalously cold SSTs in the eastern Pacific (La Niña) by some researchers (Shukla and Paolino, 1983; Rasmusson and Carpenter, 1983), but there is some dissension on this point (Webster and Yang, 1992). The interannual variability of monsoons has also been linked to variations in snow cover (Yanai and Li, 1994; Barnett *et al.*, 1989) and the thermal contrast between the equatorial Pacific and the Tibetan Plateau (Fu and Fletcher, 1985).

### 8.8 The Walker Circulation

The Walker Circulation (named by Bjerknes, 1966) is an east-west overturning of the atmosphere above the tropical Pacific Ocean, with rising motion on the west side, over the so-called “Warm Pool,” and sinking motion on the east side. The Walker Circulation can be viewed as a thermally excited stationary eddy. Although the Walker Circulation is driven by the east-to-west sea surface temperature gradient, it also helps to maintain that gradient through mechanisms to be discussed later. For this reason, the Walker Circulation is best understood as a coupled ocean-atmosphere phenomenon. It undergoes strong interannual variability. Fig. 8.39 is a schematic illustration of the walker circulation and its relation to the

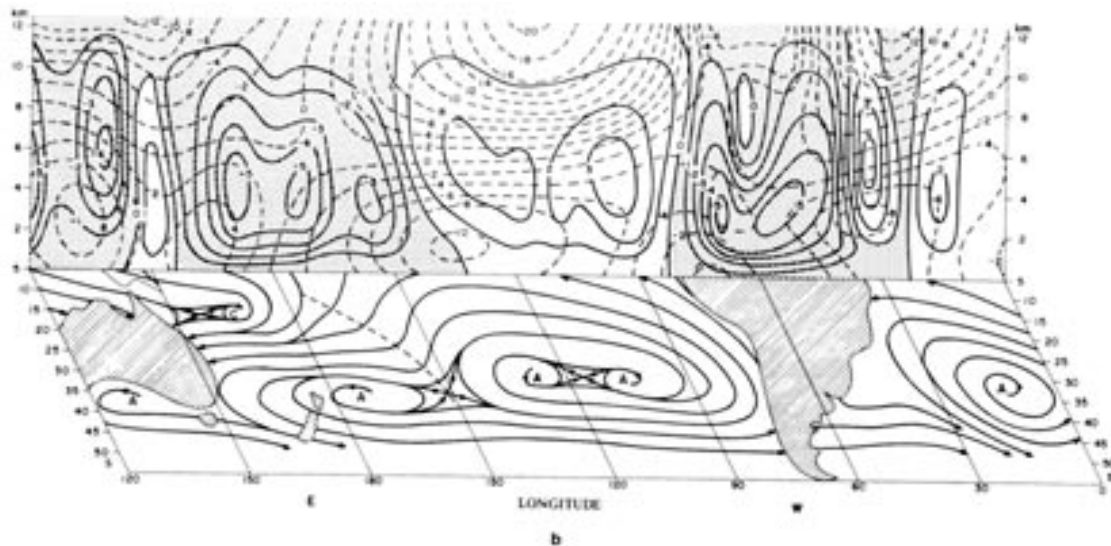
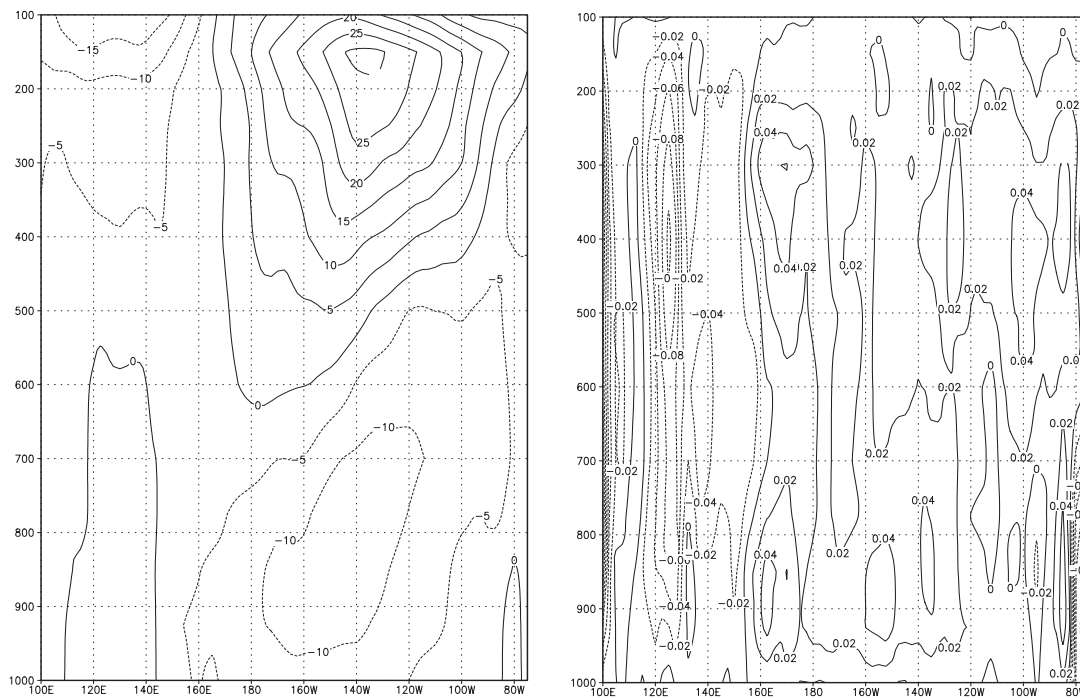


Figure 8.39: The Walker and Hadley Circulations. From Philander (1990).

surface wind field in the southern Hemisphere. The equatorward flow just west of South

America can be viewed as the inflow to the ITCZ (which is generally north of the Equator in this region), and so it is in a sense a portion of the lower branch of the Hadley circulation. Fig. 8.40 shows the observed longitude-height cross sections of the zonal wind and vertical velocity, for January.



**Figure 8.40:** The longitude-height cross-sections of the zonal wind (left, in  $\text{m s}^{-1}$ ) and vertical velocity (right, in  $\text{Pa s}^{-1}$ ) along the Equator, for January, as analyzed by ECMWF.

The Hadley Circulation is defined in terms of zonal averages, and so a particle participating in the Hadley Circulation through motions in the latitude-height plane cannot “escape” by moving to a different longitude. In contrast, the Walker Circulation is restricted to a narrow band of tropical latitudes, so that a particle participating in the Walker Circulation *can* escape by moving off to a different latitude; in fact, such meridional escapes are to be expected in view of the strong meridional motions associated with the Hadley Circulation. For this reason, we should not think of the Walker Circulation as a closed “race track;” it is better to view the Hadley and Walker Circulations as closely linked. For instance, a parcel may travel westward across the tropical Pacific in the lower branch of the Walker Circulation, ascend to the tropopause over the Warm Pool, and then move both poleward and eastward away from the Warm Pool, possibly descending in the subtropical eastern Pacific. It can then join the trades, and repeat its westward and Equatorward journey through the boundary layer.

Bjerknes (1969) theorized that the cool, dry air of the trade winds is heated and moistened as it moves westward until it finally undergoes large-scale moist-adiabatic ascent over the Warm Pool. If there were no mass exchange with adjacent latitudes, a simple circulation would develop in which the flow is easterly at low levels and westerly at upper levels. When meridional mass exchange is considered, this simple picture has to be altered, because absolute angular momentum is exported to adjacent latitudes. Under steady-state conditions, the flux divergence of angular momentum at the equator must be balanced by an

easterly surface wind stress. Thus surface easterlies on the equator are stronger than those imposed by the Walker circulation. The net result is that a thermally driven Walker cell is imposed on a background of easterly flow, the intensity of which depends on the strength of the angular momentum flux divergence.

Fig. 8.41 shows that the 1000-mb winds above the tropical Pacific (between  $10^\circ$  N and  $10^\circ$  S) have an easterly component in both solstitial seasons. For both seasons, easterly flow near the equator occurs west of about  $90^\circ$  W. In January, the easterly component is particularly strong above the central equatorial Pacific, and convergence is evident along the ITCZ near  $8^\circ$  N. In July, a notable characteristic is the strong cross-equatorial flow in the eastern Pacific. The zone of convergence at 1000 mb during the NH summer has moved north of  $10^\circ$  N over the eastern Pacific. At the latitude of the ITCZ, the easterly fetch originates to the east of Central America during both seasons. If we consider the Walker circulation to occur at near-equatorial latitudes, then easterly flow at 1000 mb cannot originate over the continents because the mountains of Peru act as a vertical barrier on the eastern boundary of the ocean. However, we note that a strong southerly component is evident during both seasons.

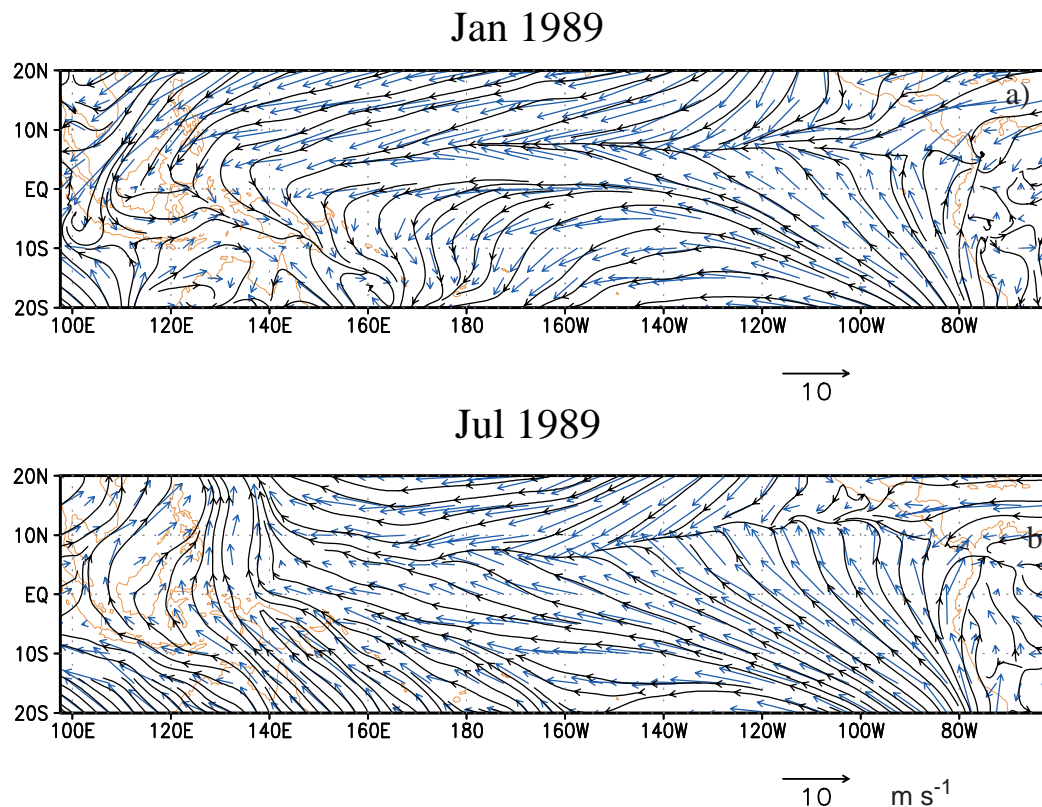


**Figure 8.41: Streamlines and horizontal wind vectors for the tropical Pacific at 1000 mb for a) January 1989 and b) July 1989. The units are  $\text{m s}^{-1}$ .**

Lindzen and Nigam (1987) used a simple model to show that SST gradients are capable of forcing low-level winds and convergence in the tropics. They assumed that near the surface the Coriolis acceleration is balanced by the sum of the horizontal pressure-gradient force and wind stress; this is called an Ekman balance. Linearizing about a state of rest, they



found a pressure field that qualitatively resembles the observations, although the wind speeds were unrealistically strong. Neelin et al. (1998) show that the model used by Lindzen and Nigam (1987) is very similar to that of Gill (1980).

Newell et al. (1996; hereafter N96) compared water-vapor data from the Upper Atmosphere Research Satellite (UARS) with upper-air wind data from the ECMWF reanalysis dataset to deduce horizontal and vertical motions in the tropical atmosphere. Their results indicate regions of strong ascending motion over the western Pacific Warm Pool and the South Pacific Convergence Zone. The main regions of sinking motion, which are located off South America and extend westward to the dateline just south of the equator, exhibit little seasonal movement. For comparison, Fig. 8.43 shows the vertical velocity fields at 300-mb

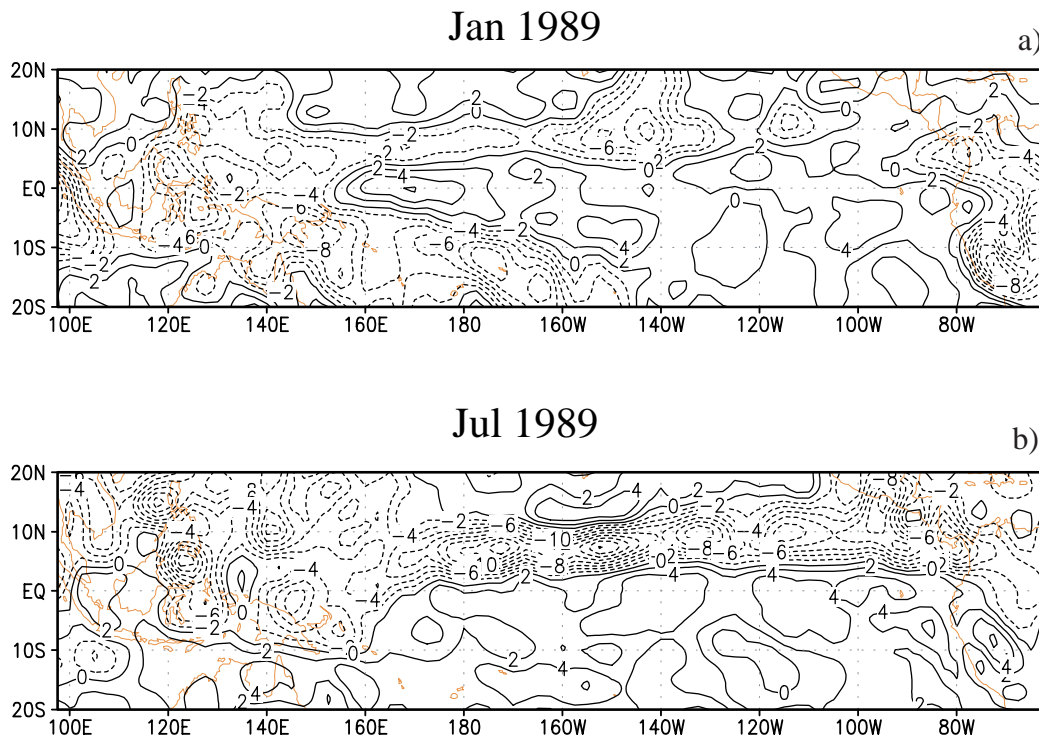


**Figure 8.42:** Contour plot of mean vertical velocity at 300mb (units,  $10^{-2} \text{ Pa s}^{-1}$ ) from the ECMWF reanalysis dataset for a) January 1989 and b) July 1989. Contour interval is  $2 \times 10^{-2} \text{ Pa s}^{-1}$ ; negative contours are dashed. Data were obtained from NCAR.

from the ECMWF reanalysis dataset for the solstitial months. During January 1989, centers of ascending motion were located near  $145^\circ \text{ E}$  at latitudes  $5^\circ \text{ N}$  and  $5^\circ \text{ S}$ . The SPCZ is clearly evident in the January 1989 data, with a large region of ascending motion that extends southeastward from  $145^\circ \text{ E}$  to  $160^\circ \text{ W}$ . A region of strong sinking motion straddles the equator and extends eastward from  $160^\circ \text{ E}$ . During July 1989, the ascending region remains fixed at  $145^\circ \text{ E}$ , but the NH and SH centers of ascending motion have merged on the equator. During the NH summer, the ITCZ is well developed at  $5^\circ \text{ N}$ , and so the zone of sinking motion has slipped southward from its January position, particularly the zone over the central Pacific. The general pattern is one in which ascending motion dominates over the tropical western Pacific, while sinking motion occurs over the tropical central and eastern Pacific. Easterlies extend across the equatorial Pacific from South America to  $170^\circ \text{ W}$  and  $160^\circ \text{ E}$ .

West of  $160^\circ$  E, the low-level equatorial winds are very weak. However, easterlies span the equatorial Pacific at  $5^\circ$  S and  $5^\circ$  N.

Fig. 8.43 shows the upper branch of the Walker circulation. West of the dateline, the zonal winds over the equator are easterly. Upper-level westerly flow occurs to the east of the rising motion. During July 1989, the upper-level flow above the equatorial Pacific ocean is

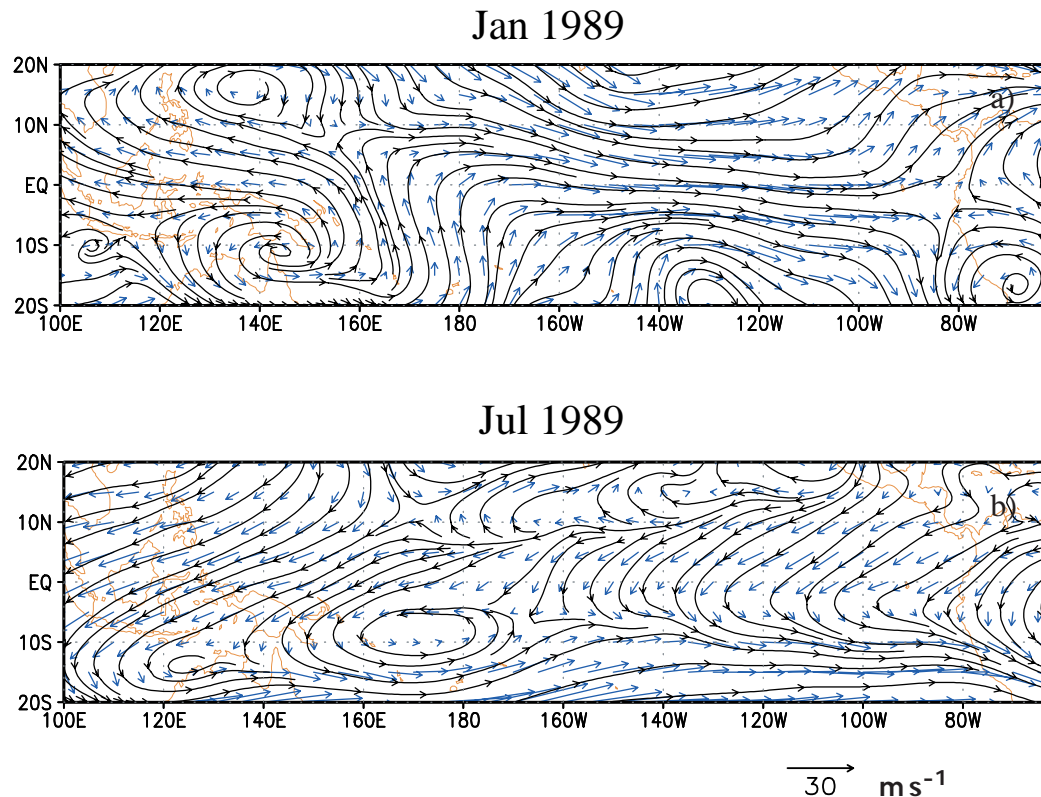


**Figure 8.43: Streamlines and horizontal wind vectors for the tropical Pacific at 200 mb for a) January 1989, and b) July 1989.**

entirely from the east. In the northern hemisphere (NH), weak westerly flow appears between  $170^\circ$  W and  $140^\circ$  W poleward of  $15^\circ$  N. In the southern hemisphere (SH), a westerly component of the wind exists south of  $5^\circ$  S to the east of the dateline. An interpretation is that the Walker circulation has migrated into the SH. A reexamination of Fig. 8.42b indicates that sinking motion is confined mainly to the SH, and occurs as far west as  $165^\circ$  W.

The Walker Circulation is an atmospheric phenomenon, but it is closely tied to east-west sea surface temperature gradients that are produced by atmospheric phenomena including aspects of the Walker Circulation itself. The Walker Circulation can thus be viewed as a phenomenon of the coupled atmosphere-ocean system. Fig. 8.44 shows that a sea-surface temperature (SST) maximum occurs over the tropical region centered on  $120^\circ$  E, and for this reason the region is known as the tropical Warm Pool. The “cold tongue” is a band of relatively cold waters along the equator that stretches from South America westward to near  $160^\circ$  E. Although a noticeable SST gradient exists along and across the cold tongue, the temperature variation is still much smaller than that which is generally observed in extratropical or polar regions of the globe. The tropical climate is characterized by sea surface

and horizontal air temperature gradients that are weak compared to the corresponding mid-latitude gradients. As explained by Charney (1963), for cloud-free regions of the tropics, pressure and temperature gradients must be small compared to those of midlatitudes.

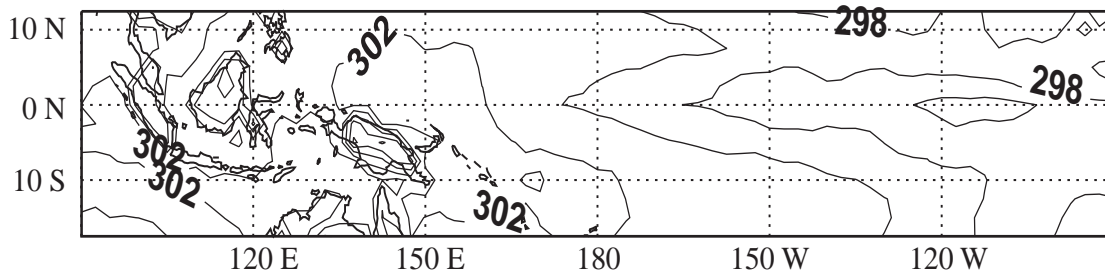


**Figure 8.44:** Tropical skin temperature for January 1989 from the ECMWF reanalysis dataset obtained from NCAR. Resolution for this dataset is  $2.5^\circ$  and the contour interval is 2 K.

The distribution of tropical convection is strongly related to both the local SST and the SST gradient. The tropical-Pacific Warm Pool is a region of intense deep convection. In Fig. 8.45, regions in which the outgoing longwave radiation (OLR) is less than  $225 \text{ W m}^{-2}$  can be identified as areas of frequent convection (Webster 1994). The OLR threshold corresponds to a monthly mean emission temperature of 250 K. Due to longwave trapping by optically thick anvil clouds, which are produced by deep convection, the OLR is reduced and threshold values of OLR can therefore be used as surrogates to infer the presence of convection. From the figure, we see that convection occurs throughout the Warm Pool, and in

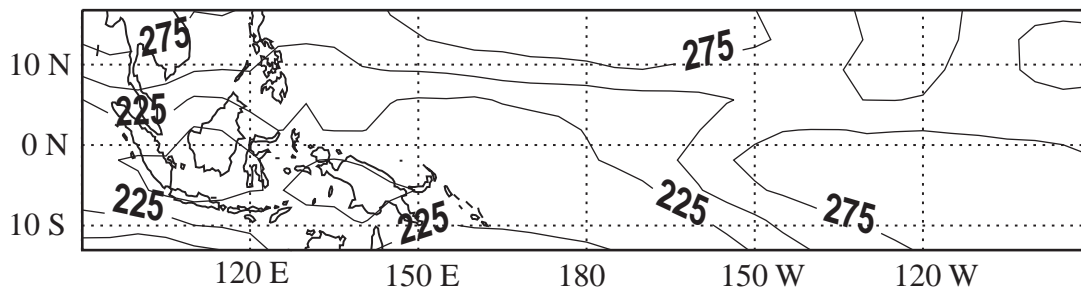


**Figure 8.45:** Tropical OLR for January averaged over 1985 to 1988. Daily means from the Earth Radiation Budget Experiment (ERBE) were averaged and interpolated onto a  $5^\circ \times 4^\circ$  (longitude–latitude) grid. The units are  $\text{W m}^{-2}$ .

the South Pacific convergence zone (SPCZ). On the other hand, the OLR is generally larger than  $275 \text{ W m}^{-2}$  across the equatorial cold tongue, indicating that convection is infrequent there.

The high, cold, and sometimes bright clouds of the Warm-Pool region limit the radiative cooling of the atmosphere over the Warm Pool, but they also limit the solar warming of the ocean. Ramanathan and Collins (1991) hypothesized that cirrus clouds act as a thermostat to regulate tropical SST. They used Earth Radiation Budget Experiment (ERBE) data to deduce the inter-relationships among shortwave and longwave cloud radiative forcings and radiative forcing of the clear atmosphere. They emphasized that the shortwave effects of clouds dominate over the longwave effects in regulating SST. According to their



hypothesis, as SST increases, the cloud albedo increases. According to their idea, the atmosphere warms as a result of longwave cloud radiative effects, stronger latent-heat release by convection, and a stronger SST gradient over the tropical Pacific. This warming leads to an amplification of the large-scale flux convergence of moisture. The process continues until the reflectivity clouds increases sufficiently to cool the surface. A criticism of their study is that changes in the strength of the ocean and atmosphere circulations were not included. Nevertheless it undoubtedly true that the blocking of shortwave radiation by deep cloud systems tends to limit the sea-surface temperature in the Warm Pool.

In the eastern tropical Pacific, stratus clouds in the boundary layer intercept sunlight and strongly reduce the heat flux into the ocean below (e.g. Hartmann et al. 1992). In this way, the atmosphere helps to maintain the cooler SSTs of the eastern Pacific. Stratus clouds form preferentially over cold water (Klein and Hartmann 1993), so a positive feedback is at work here (Ma et al. 1996). Latent heat exchange between the ocean and atmosphere is influenced by the surface relative humidity and the surface winds. For fixed relative humidity and SST, the evaporative cooling of the ocean increases as the surface wind stress increases. The winds also influence the SST distribution by generating cold-water upwelling in the eastern Pacific, and along the equator in the eastern and central Pacific. As discussed in Chapter 2, the equatorial cold tongue is due to upwelling driven by the trade winds.

The driving force behind the Walker circulation is the zonally varying heating that is balanced by zonally varying adiabatic heating/cooling due to sinking/rising motions. Over the warm waters of the western Pacific, latent heat release due to intense convection and radiative warming of the atmospheric column are balanced by the adiabatic cooling associated with rising motion (Webster 1987). Over the eastern tropical Pacific, where the SST is relatively cold, convection is infrequent, and so a balance between radiative cooling and subsidence exists, as discussed in Chapter 2.

Pierrehumbert (1995; hereafter P95) presented a two-box model of the Hadley/Walker circulation that has strongly influenced recent studies of the tropical climate. Fig. 8.47 presents a schematic of his “furnace/radiator-fin” model. The model has separate energy budgets for its Cold-Pool and Warm-Pool regions. The SSTs of the Cold Pool and Warm Pool are assumed to be those that give energy balance for each box of the model atmosphere and for the Cold-Pool ocean. Surface energy balance for the Warm Pool was not explicitly included in the model. A vertically and horizontally uniform lapse rate was assumed, and the free-tropospheric temperature profile was assumed to be uniform across the tropics. The radiating temperature of the Cold-Pool free atmosphere was assumed to be the air temperature at  $z = z_T/2$ , where  $z_T$  is the assumed height of the tropopause. The solution was obtained by first computing the net energy flux at the top of the Warm-Pool atmosphere for a given SST and relative humidity profile. The net radiative flux at the Warm-Pool TOA was assumed to be balanced by a horizontal energy transport to the Cold Pool. The Cold-Pool SST and radiating temperature were then computed under the constraint that the net diabatic cooling must balance the energy imported laterally from the Warm Pool.

The mass flux of the Hadley-Walker circulation was assumed to be that required to give a balance between adiabatic warming by dry subsidence and the net radiative cooling of the Cold-Pool region. It can be shown that the horizontal heat transport by the Warm-Pool atmosphere is proportional to the diabatic cooling of the Cold-Pool atmosphere and to the ratio of Cold-Pool area and Warm-Pool area. This area ratio is a prescribed parameter of the model. P95 showed that for very small values of the Cold-Pool emissivity, the Warm-Pool SST increases without limit, because the Cold Pool cannot radiate enough energy to balance the Warm Pool. Because the Warm Pool controls the temperature profile, its equilibrium SST must decrease as the Cold-Pool radiating temperature decreases. As the Cold-Pool emissivity

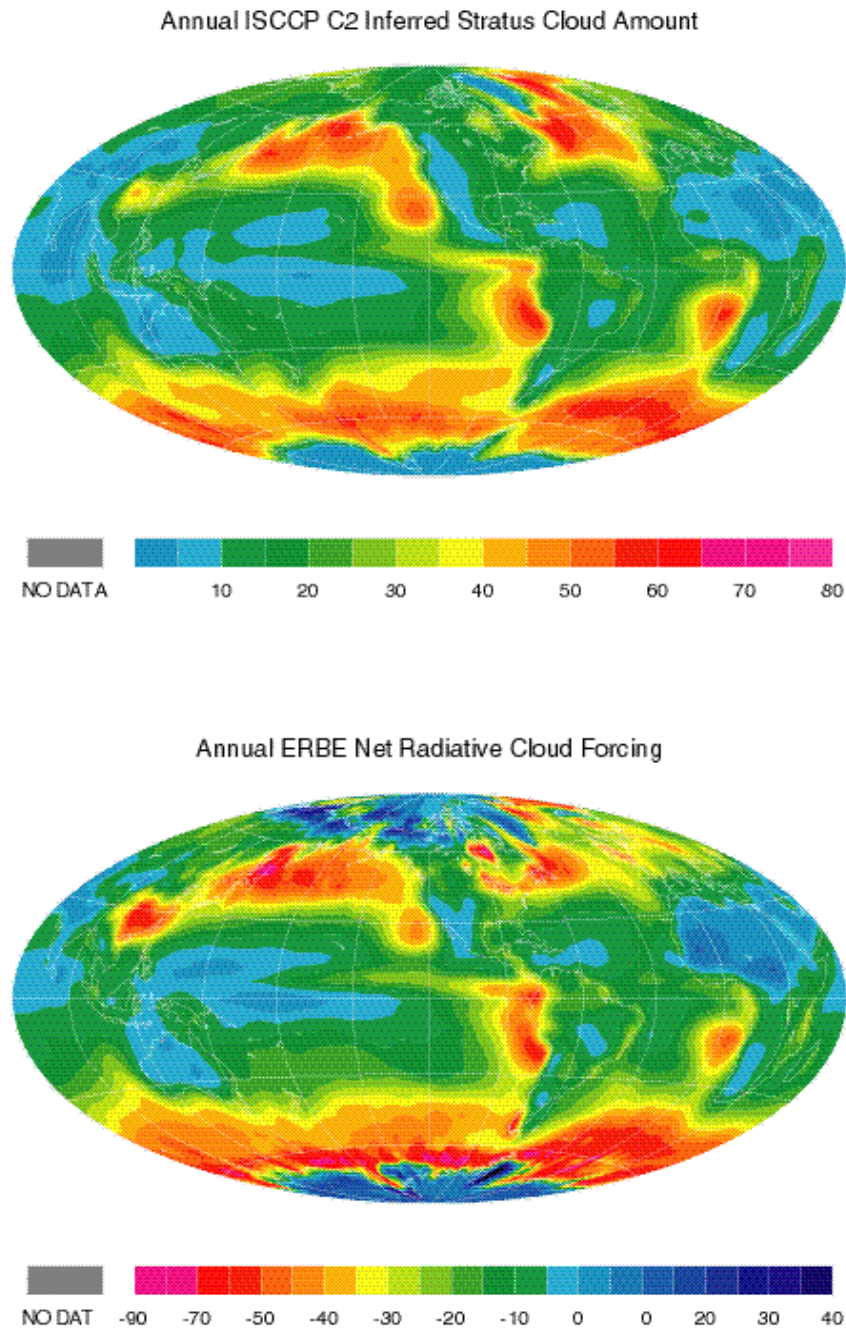
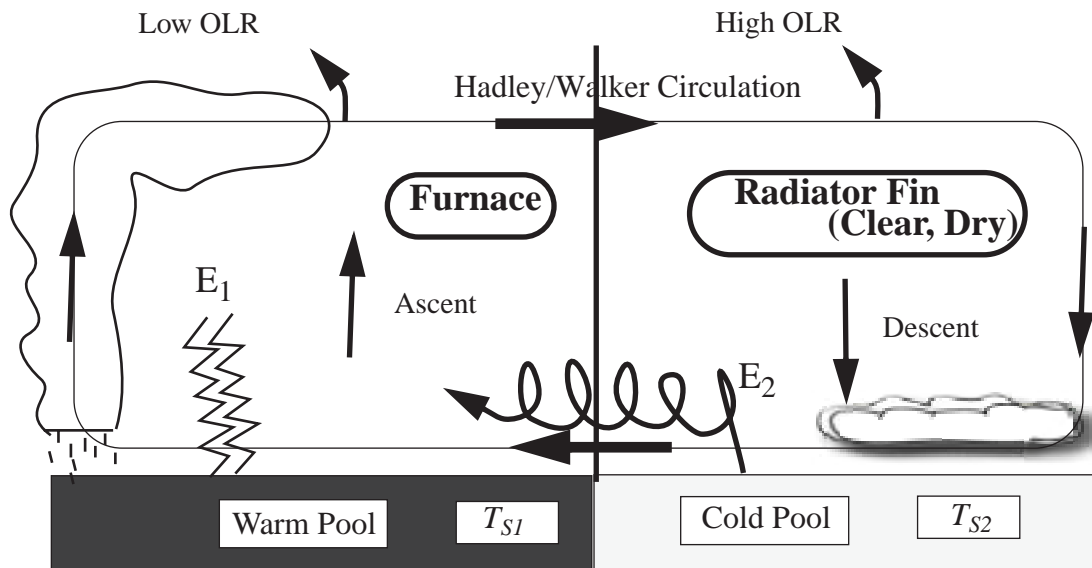


Figure 8.46: Observed annual-mean low-cloud amount (upper panel) and the net effects of clouds on the Earth's radiation budget (lower panel). Negative values in the lower panel indicate a cooling, i.e. shortwave reflection dominates longwave trapping.



**Figure 8.47:** Reproduction of Pierrehumbert's schematic representation of the 'furnace/radiator-fin' model of the tropical circulation. The symbols  $E$  and  $T_S$  represent the evaporation rate and SST, respectively. The subscripts 1 and 2 denote the Warm Pool or furnace and the Cold Pool or radiator fin.

increases, the Warm-Pool cools off. The simulated Cold-Pool and Warm-Pool SSTs resemble the present-day climate for a range of conditions. The diagnosed mass flux is realistic. A weakness of the model is that it fails to account for cloud-radiative effects.

Miller (1997) extended Pierrehumbert's model by studying the radiative effects of low clouds in the Cold-Pool region. Extending the basic concepts of P95, Miller constructed a three-box model, which includes energy- and moisture-balance equations for the boundary layer and free troposphere and a surface energy budget for each of three boxes: the updraft region, the Warm Pool, and the Cold Pool. Taking advantage of the small surface area covered by the updrafts, Miller simplified the model for the limit of vanishing updraft cross-sectional area. He demonstrated that in this limit, the boundary layer and tropopause of the Warm Pool region must be connected by a moist adiabat. Miller assumed that the lapse rate of the Warm Pool region is moist adiabatic. Following P95, atmospheric dynamics were implicitly included by assuming a uniform free-tropospheric temperature sounding across both the Warm and Cold Pool regions. Miller's main conclusion is that low clouds in the Cold Pool act as a thermostat for the SST throughout the tropics.

## 8.9 The Madden-Julian Oscillation

The tropical atmosphere undergoes a powerful oscillation with a period in the range 30 - 60 days (Fig. 8.48). The oscillation appears most clearly over the Indian and western Pacific Oceans, and involves many meteorological variables, including the zonal wind, surface pressure, temperature, and humidity (Madden and Julian, 1971, 1972). It is referred to as the Madden-Julian Oscillation (MJO), or sometimes the Tropical Intraseasonal Oscillation.

Observations have revealed corresponding oscillations of various measures of

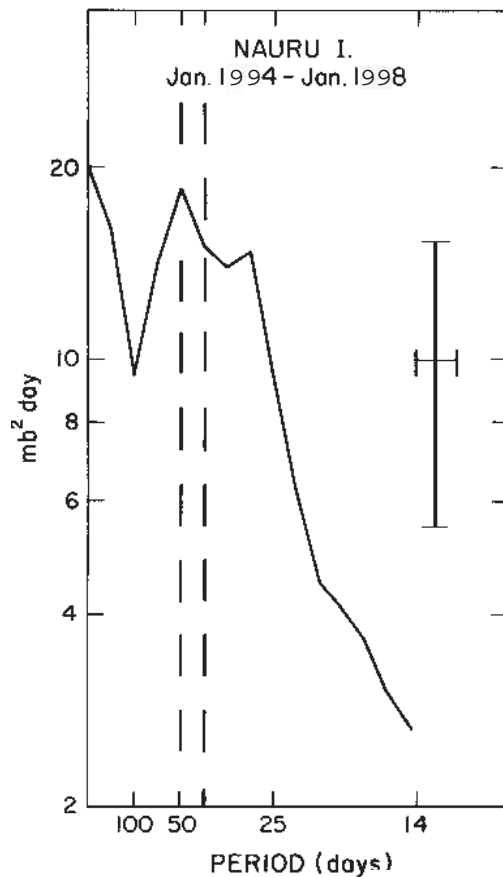


Figure 8.48: Variance spectrum for station pressures at Nauru Island,  $0.4^{\circ}$  S,  $161.0^{\circ}$  E. Ordinate (variance/frequency) is logarithmic and abscissa (frequency) is linear. The 40–50-day period range is indicated by the dashed vertical lines. Prior 95% confidence limits and the bandwidth of the analysis ( $0.008 \text{ day}^{-1}$ ) are indicated by the cross. From Madden and Julian (1994). Taken from Madden and Julian (1972 a).

cumulus activity (Murakami et al., 1986), including precipitation (Hartmann and Gross, 1988) and outgoing longwave radiation (e.g., Weickmann and Khalsa, 1990). A schematic depiction of the MJO is provided in Fig. 8.49. The observed phase propagation is shown in Fig. 8.50. The MJO does not produce oscillations of convection over the Amazon basin or the Congo basin, even though an MJO signal is sometimes observed in the winds at those longitudes.

Embedded within the MJO are fluctuations on smaller space and time scales (Nakazawa, 1988; Fig. 8.51).

The MJO has been the subject of intense research because of its intraseasonal time scale, which suggests that intraseasonal weather anomalies may be predictable; and also because of their apparent relationships with the Indian summer monsoon (Yasunari, 1979; Krishnamurti and Subrahmanyam, 1982), the likelihood of tropical Pacific storms (Gray, 1979), and the initiation of El Niño events (Lau and Chan, 1985). Since tropical convection can force Rossby waves that propagate into the extratropics, the MJO can also influence the weather in middle latitudes (e.g., Rueda, 1991).

The MJO is a first baroclinic mode, equatorially-trapped, convectively-coupled disturbance that propagates at a phase speed of about  $5 \text{ m s}^{-1}$  as it travels from the Indian Ocean eastward to the dateline, at which point its convective coupling diminishes and it

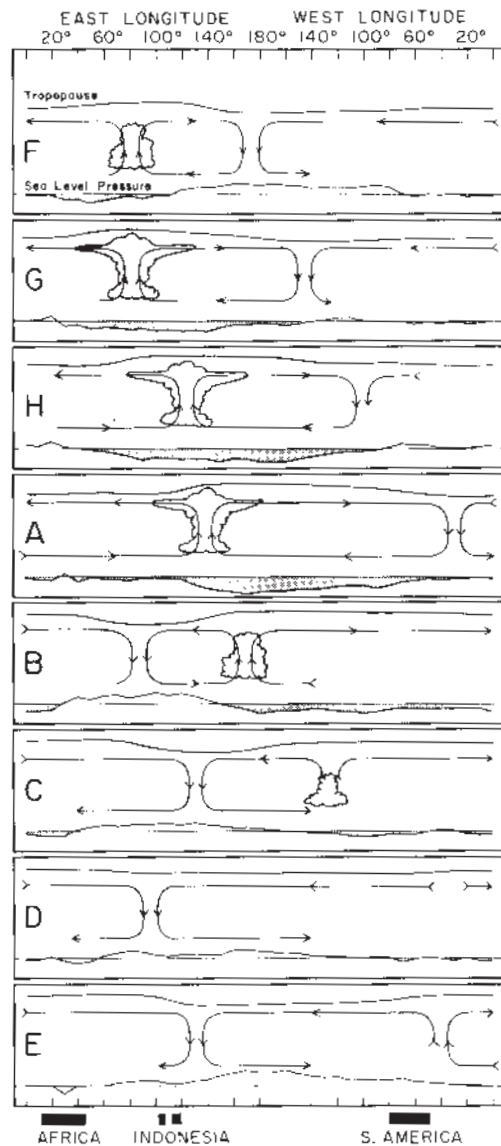


**Figure 8.49:** Schematic depiction of the time and space (zonal plan) variations of the disturbance associated with the 40-50-day oscillation. Dates are indicated symbolically by the letters at the left of each chart and correspond to dates associated with the oscillation in Canton's station pressure. The letter A refers to the time of low pressure at Canton and E is the time of high pressure there. The other letters represent intermediate times. The mean pressure disturbance is plotted at the bottom of each chart with negative anomalies shaded. The circulation cells are based on the mean zonal wind disturbance. Regions of enhanced large-scale convection are indicated schematically by the cumulus and cumulonimbus clouds. The relative tropopause height is indicated at the top of each chart. From Madden and Julian (1994). Taken from Madden and Julian (1972 a).

propagates at about  $12 \text{ m s}^{-1}$ . Global circumnavigation of the disturbance can sometimes be seen in upper-tropospheric velocity potential, but is harder to detect in other fields closer to the surface. In the oceanic regions of the eastern hemisphere, the disturbance is closely coupled to convective processes and is characterized by strong surface fluxes. During its convectively inactive phase, the MJO is characterized by weak surface easterlies and high downward radiative fluxes. In the convectively active phase, strong surface westerlies and high surface latent heat fluxes are observed.

An understanding of the MJO has been elusive. Most theories fall into one of the following three categories:

- 1) wave-CISK theories (e.g., Hayashi, 1970; Lindzen, 1974; Hayashi and Sumi, 1986; Lau and Peng, 1987; Salby et al., 1994),



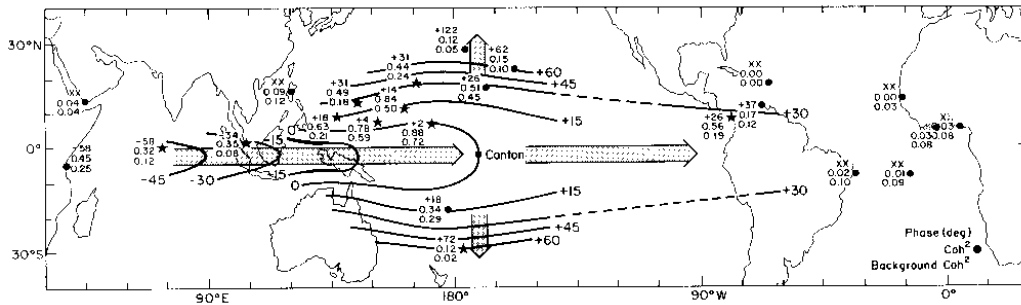


**Figure 8.50:** Mean phase angles (in degrees), coherence squares, and background coherence squares for approximately the 36-to-50-day period range of cross spectra. between surface pressures at all stations and those at Canton. The plotting model is given in the lower right-hand corner. Positive phase angle means Canton time series leads. Stars indicate stations where coherence squares exceed a smooth background at the 95% level. Mean coherence squares at Shemya ( $52.8^{\circ}$  N,  $174.1^{\circ}$  E) and Campbell Island ( $52.6^{\circ}$  S,  $169.2^{\circ}$  E; not shown) are 0.08 and 0.02, respectively. Both are below their average background coherence squares. Values at Dar es Salaam ( $0.8^{\circ}$  S,  $39.3^{\circ}$  E) are from a cross spectrum with Nauru. The arrows indicate propagation direction. From Madden and Julian (1994), adapted from Madden and Julian (1972).

- 2) surface evaporation feedback theories (Emanuel, 1987; Neelin and Yu, 1994; Yu and Neelin 1994), called WISHE (wind-induced surface heat exchange) theories, and
- 3) local forcing or discharge-recharge theories (Blade and Hartmann, 1993; Hu and Randall, 1994; Salby and Garcia, 1997; Flatau et al., 1997).

Each of these categories of theories has strengths and weaknesses.

The basic premise of wave-CISK theories is that the waves and the cumulus heating sustain each other and propagate eastward together via their mutual interactions and feedbacks. In order to maintain a continuous progression of waves at any given longitude, the waves have to complete a global circuit without dissipating. A major problem with these theories is that they have difficulty explaining the observed phase speeds and vertical structures of the waves. The wave-CISK theory (Hayashi, 1970; Lindzen, 1974) predicts a vertical wavelength of 8 - 9 km for waves with a Doppler-shifted phase speed of  $10\text{--}15\text{ m s}^{-1}$  (consistent with a global circuit in 40-50 days). This vertical wavelength is less than half that of the observed 30 - 60 day waves in the tropics (15 - 30 km, see Madden and Julian, 1972). In other words, a direct application of the classic wave-CISK theory predicts a phase speed twice as fast as observed, for waves of the observed depth.

Chang (1977) produced a new, “viscous” mode by introducing a damping term that raised the order of the dispersion equation by one. Although the viscous mode’s eastward phase speed is slow compared to the that of the classic wave-CISK modes, it has significant amplitude only near the heat source. Chang did not explain the mechanism that produces the oscillating heat source. Along similar lines, Lau and Peng (1987) proposed a theory in which negative heating is not permitted. Although their results show modes that realistically

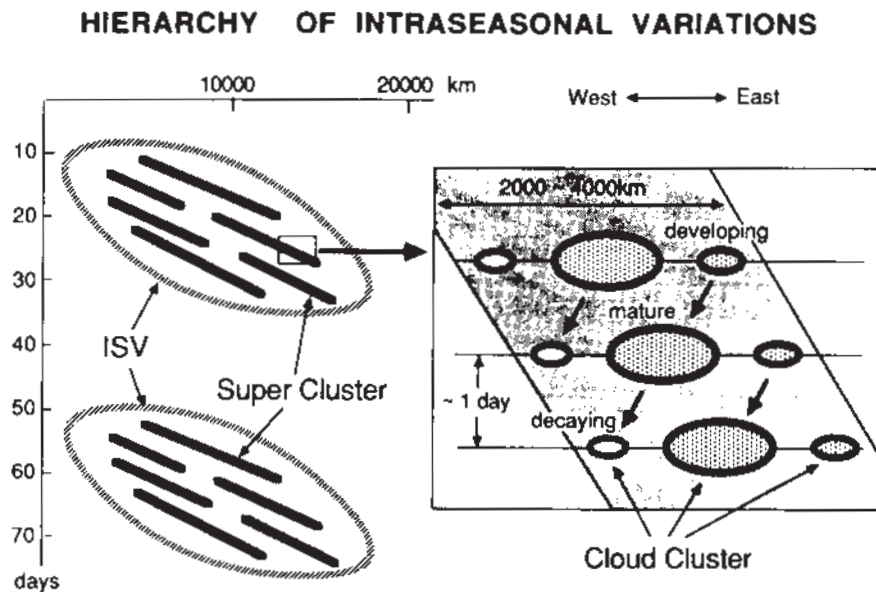


**Figure 8.51:** Schematic describing the details of the large-scale eastward-propagating cloud complexes [slanting ellipses marked ISV (intraseasonal variability) on the left-hand side]. Slanting heavy lines represent super cloud clusters (SCC) within the larger complexes or ISV. The right-hand side illustrates the fine structure of the SCC with smaller westward-moving cloud clusters that develop, grow to maturity, and decay in a few days. From Nakazawa (1988).

combine deep vertical scales with slow phase speeds, these are a consequence of their *specified* heating profile that has a maximum near the 700 mb level (see their Table 2). Chang and Lim (1988) argued that such a low-level heating maximum is necessary in order to generate slowly propagating modes. Wang (1988) suggested that interactions between internal and external modes can generate slow, eastward-propagating waves. Wang and Chen (1989) showed that the frictionally forced boundary-layer convergence of mass and moisture can induce such interactions. When frictional moisture convergence is strong enough, the growth of low-frequency planetary waves is favored. It remains to be seen whether this mechanism can explain how a low-frequency oscillation is excited.

Pursuing a rather different idea, Neelin et al. (1987) and Emanuel (1987) hypothesized a feedback based on “wind-induced surface heat exchange” (WISHE) to explain the Madden-Julian oscillation. According to their theory, the heat source is maintained by both the waves through their interaction with the low-level flow. The maintenance and eastward propagation of convection in this theory depends on the existence of a mean easterly flow in the Indian and western Pacific Oceans. Such winds are not observed, however (e.g., Oort, 1983). In addition, observations show that the strongest evaporation in an MJO disturbance occurs on the west side of the convection, rather than the east side. WISHE does appear in some numerical model results, however. It is possible that WISHE accounts for the initial (i.e., small-amplitude) growth of the MJO, even though it does not appear to describe fully developed events.

The discharge-recharge idea has received some support in recent years. Hartmann and Gross (1988) analyzed a 22-year time series of tropical precipitation, and showed that the 30 -

60 day oscillation of precipitation occurs only at stations within or near the areas of intense convection in the Indian and western Pacific Oceans, e.g., the SPCZ. They found that the oscillations of precipitation lead those of the zonal wind by 5 - 6 days. This phase difference suggests that the observed propagating low-frequency waves in the zonal winds are forced by the convection, but not the reverse.

Hsu et al. (1990) reported a stationary, fluctuating, low-frequency latent heat source in the tropical western Pacific. Waves appear to emanate from the region of the oscillating heat source, and to propagate both eastward and poleward. The heating itself is relatively localized and does not appear to be symbiotically coupled with the propagating waves. Interestingly, Hsu et al. (1990) found that the eastward-propagating 30 - 60 day waves typically complete only about a half cycle before they dissipate. This appears to rule out the possibility that episodes of enhanced convection are triggered by the arrival, from the west, of eastward-propagating waves that were forced by their predecessors.

Holton (1972) showed that a specified oscillating tropospheric heat source excites waves in both the troposphere and the stratosphere; naturally, these waves have the same period as the heating. Their vertical scale is on the order of 20-30 km. For Kelvin waves, the zonal wavelength is linearly proportional to the vertical scale of the waves; deep modes have zonal wave number one. Studies by Yamagata and Hayashi (1984), Hayashi and Miyahara (1987), Salby and Garcia (1987), and Garcia and Salby (1987), among others, provide examples of the application of this forcing - response concept to the Madden-Julian oscillation. Salby and Garcia showed that the response of the tropospheric winds to a stationary 30-day heating oscillation in the tropical western Pacific Ocean closely resembles that of the observed Madden-Julian oscillation. They found that the period of the oscillation increases with the period of the heating. They further demonstrated that eastward-propagating waves excited in the lower troposphere in the Western Pacific are likely to succumb to dissipation before reaching the Americas. As shown by Salby and Garcia (1987) and Garcia and Salby (1987), a low-frequency tropical heat source excites waves that propagate slowly and have structures similar to the observed Madden-Julian waves. In summary, several studies have shown that slow eastward- and poleward-propagating waves with vertical scales comparable to that of the Madden-Julian oscillation can be explained quite naturally as responses to localized, low-frequency tropical heating.

Recharge of atmospheric moisture on MJO time scales has been reported in the literature. Lin and Johnson (1996) analyzed TOGA COARE data that revealed an intensely dry mid-troposphere after the passage of the MJO. This drying was accompanied by subsidence and scattered, shallow cumulus convection. With time, the base of the very dry layer rises, so that the atmosphere is moistened from below, restoring conditions to those favorable a new episode of deep convection. Whether this remoistening occurs through large-scale convergence or local effects is not clear. Maloney and Hartmann (1998), Hendon and Glick (1997), and Lau and Sui (1997) present evidence supporting large-scale convergence. In their analyses of various observational data sets, Woolnough et al. (1999) and Kembell-Cook and Weare (2000) conclude that the remoistening of the atmosphere is accomplished through local thermodynamic control. DeMott and Rutledge (1998) document the gradual increase in convective cloud top height during convectively inactive periods of TOGA COARE, and attribute this gradual increase to the erosion of the base of the dry layer, thereby paving the way for greater instability and progressively deeper convection. Similar behavior in cloud top heights has been reproduced by Inness et al. (2001) in GCM studies of the MJO. In this study, increasing the vertical resolution of the model resulted in a more realistically broad distribution of cloud-top heights than the lower-resolution version of the model. The more realistic cloud-top height distribution led to enhanced detrainment of cloud mass at lower levels of the atmosphere and a more robust MJO signal.



Some authors have suggested that fluctuations of the SST are important for the MJO. Flatau et al. (1997) and Walliser et al. (1999) reported that simulated 30-60-day tropical variability increased when their atmospheric general circulation models (GCMs) were coupled to slab ocean models. They concluded that the increased variability at MJO time scales was linked to the response time of sea surface temperatures (SSTs) to cooling associated with the convective phase of the MJO. Wang and Xie (1998) simulated the coupled tropical system within a linear model framework and concluded that the ocean mixed layer sustains the MJO by destabilizing the moist Kelvin wave, providing a longwave selection mechanism, and slowing down the phase propagation to the expected 40-50-day period, although a physical mechanism by which this occurs was not clearly stated. Shinoda et al. (1998), through an analysis of observational data, also proposed that the ocean mixed layer controls (slows) the period of oscillation by reducing surface latent and sensible heat fluxes at MJO time scales below those that would be expected in the absence of MJO time scale variability in the upper layers of the ocean. In summary, discharge-recharge theories are attractive in that they offer a possible explanation for the observed seasonality of the MJO, and invoke coupling to the ocean as a mechanism to explain the period of the oscillation.

It has also been suggested that the MJO can be triggered by low-frequency variability in middle latitudes. In concluding that some sort of atmospheric discharge-recharge process controls the MJO, Blade and Hartmann (1993) mention east Asian pressure surges as one possible “trigger” for setting off the MJO after the atmosphere has recharged from the previous MJO episode. Meehl et al. (1996) present composites of 6-30-day OLR variability over the Indian and Pacific Ocean regions and examine the accompanying upper-level wave trains and surface pressure perturbations on this time scale. They conclude that pressure-surge activity on this time scale interacts with convective activity on MJO time scales, albeit through a rather complex, dynamical interaction. A similarly complex picture of pressure surge activity and MJO interaction is discussed in Compo et al. (1999), but nevertheless provides a link between quasi-stochastic high-frequency pressure surge activity and MJO-related convection. The existence of such a link seems plausible given the seasonal variations in MJO activity.

## 8.10 Summary

In this chapter, we explored the nature of the wave motions that fill the atmosphere, from both theoretical and observational perspectives. The basic theory of planetary waves, governing even the tropical waves that were rediscovered by Matsuno in 1966, was worked out by Laplace.

The waves of largest scale are by far the most energetic, and produce the lion’s share of the fluxes of heat, moisture, and momentum that affect the zonally averaged flow.

Monsoons and the Walker Circulation can be regarded as thermally forced eddies.

Transient and stationary eddies are both important components of the general circulation of the atmosphere. Their effects on the mean flow are the subject of the next Chapter.

## Problems

1. Show that for an isothermal atmosphere the static stability,  $S_p$ , increases strongly upward.

2. Show that for a resting isentropic basic state with no heating and no gravitational forcing, perturbations satisfy

$$\frac{\partial z'}{\partial t} + H_0 \nabla_p^2 \chi = 0, \quad (8.100)$$

for all  $p$ , where  $H_0 = RT_0/g$  and subscript zero denotes a surface value. Notice that (8.100) looks very much like the continuity equation for shallow water.

3. Show that for an isothermal atmosphere the vertical wavelength of a vertically propagating free wave decreases as its equivalent depth,  $h_n$ , decreases. Show also that if the equivalent depth exceeds a particular value, vertical propagation does not occur. Assume  $h_n > 0$ .
4. Show that the FOSC with the nondivergent approximation ( $\chi = 0$ ) must satisfy

$$\nabla_p \bullet (f \nabla_p \Psi) = g \nabla_p^2 z'. \quad (8.101)$$

This implies that the oscillation is not in exact geostrophic balance.

5. Planetary waves are often observed to “bend westward” on their equatorward sides (see Fig. 8.52). Give an explanation for this based on Rossby wave dynamics.
6. Show that when there is a basic zonal current from the west, with a constant angular velocity  $\dot{\lambda}$ , the apparent “phase speed” relative to the Earth’s surface of the free oscillation of the second class is given by

$$-\frac{\sigma}{s} = \dot{\lambda} - \frac{2(\Omega + \dot{\lambda})}{n(n+1)}. \quad (8.102)$$

7. Laplace’s tidal equation has a special solution when the period of oscillation is 1/2 day and the longitudinal wave number is zero.

i) Show that the solution is given by

$$\Theta_n = A \sin(\sqrt{\epsilon_n} \mu) + B \cos(\sqrt{\epsilon_n} \mu)$$

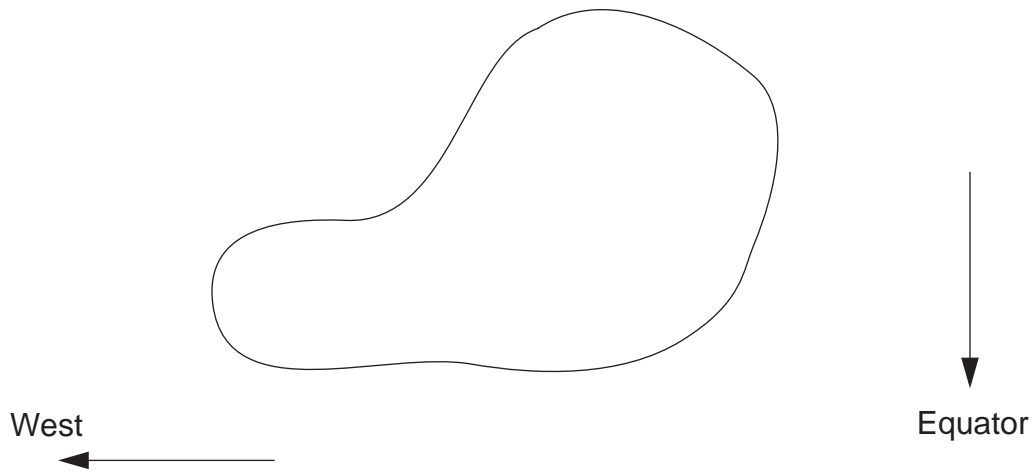


Figure 8.52: Schematic illustration of the structure of a Rossby wave.

where

$$\epsilon_n = \frac{4\Omega^2 a^2}{gh_n}$$

j) Show that

$$\epsilon_n = \left(\frac{1}{2}n\pi\right)^2, n = 1, 2, \dots$$

$$A/B = \tan\left(\frac{n\pi}{2}\right)$$

k) are required to satisfy the boundary condition that  $V_n$  remains finite at the poles. This solution was found by Solberg (1936).

8. Prove that an isothermal atmosphere has only one equivalent depth for free oscillations, given by

$$\hat{h} = \gamma H, \quad (8.103)$$

where  $\gamma \equiv c_p/c_v$ , and  $H = RT/g$ .

9. Show that the gravitational tidal potential  $\Phi$  at a point  $P$ , due to the moon, is approximately given by

$$\Phi \cong -\frac{3\gamma_g M a^2}{2 D^3} \left( \frac{1}{3} - \cos^2 \theta \right), \quad (8.104)$$

where  $\gamma_g$  is the universal constant of gravitation,  $M$  is the mass of the moon, and  $D$  and  $\theta$  are as shown in Fig. 8.53.

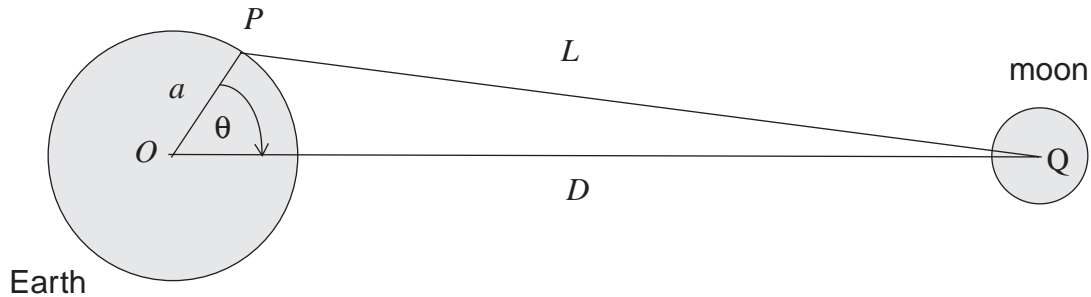


Figure 8.53: Earth-moon geometry.

10. a) Work out an algebraic expression for the temperature profile, as a function of pressure, in an atmosphere that has a constant (vertically uniform) static stability.
- b) Choose a “typical” positive constant for value for the static stability, and explain how you arrive at this choice. It should be “typical” for either the troposphere or the stratosphere, and you should state which. Plot the temperature as a function of pressure using this value, for pressures ranging from 1000 mb to 1 mb, assuming a surface temperature of 288 K. Repeat, assuming a temperature at 1 mb of 270 K. Comment on the two plots -- are they at all realistic?
- c) Find all of the equivalent depths for free oscillations in an atmosphere with constant static stability.

11. For the model of Charney and Eliassen, derive an expression for the “mountain torque” associated with stationary, frictionally damped, resonant waves (i.e.  $K^2 = K_S^2$ ).
12. Derive (8.79) from (8.72). Verify by substitution that (8.83) is a solution of (8.79).

